5-2013

INTEGRATING BIOMECHANICS AND CELL PHYSIOLOGY TO UNDERSTANDING IVD NUTRITION AND CELL HOMEOSTASIS

Yongren Wu
Clemson University, bioewu@gmail.com

Recommended Citation

Wu, Yongren, "INTEGRATING BIOMECHANICS AND CELL PHYSIOLOGY TO UNDERSTANDING IVD NUTRITION AND CELL HOMEOSTASIS" (2013). *All Dissertations*. 1123.
https://tigerprints.clemson.edu/all_dissertations/1123

INTEGRATING BIOMECHANICS AND CELL PHYSIOLOGY TO UNDERSTANDING IVD NUTRITION AND CELL HOMEOSTASIS

A Dissertation
Presented to
the Graduate School
of Clemson University

In Partial Fulfillment
of the Requirements for the Degree
Doctor of Philosophy
Bioengineering

---

by
Yongren Wu
May 2013

Accepted by:
Dr. Hai Yao, Committee Chair
Dr. Martine LaBerge
Dr. Jiro Nagatomi
Dr. Barton L. Sachs

ABSTRACT

Back pain associated with degeneration of the intervertebral disc (IVD) is a major public health problem in Western industrialized societies. Degeneration of the IVD changes the osmotic and nutrient environment in the extracellular matrix (ECM) which affects cell behaviors, including: cell proliferation, cell energy metabolism, and matrix synthesis. In addition, a thin layer of hyaline cartilaginous end-plate (CEP) at the superior/inferior disc-vertebral interface was found to play an important role in nutrient supply as well as load distribution in the IVD. Therefore, our general hypothesis is that the CEP regulates the ECM osmotic and nutrient environment which further affects IVD cell energy metabolism and homeostasis.

First, based on the triphasic theory, we developed a multiphasic model that considered the IVD tissue as a mixture with four phases: solid phase with fixed charges, interstitial water phase, ion phase with two monovalent species (e.g., Na^+ and Cl^-), and an uncharged nutrient solute phase. Our numerical results showed calcification of the CEP significantly reduced the nutrient levels in the human IVD. In cell based therapies for IVD regeneration, excessive amounts of injected cells may cause further deterioration of the nutrient environment in the degenerated disc. To address the lack of experimental data on CEP tissue, the regional biomechanical and biochemical characterization of the bovine CEP was conducted. We found that the lateral endplate was much stiffer than the central endplate and might share a greater portion of loading. Our results also indicated that the CEP could block rapid solute convection and allowed pressurization of the interstitial fluid in response to loading. The energy metabolism properties of human IVD cells in different extracellular nutrient environments were also outlined. We found that human IVD cells prefer a more prevalent glycolytic pathway for energy needs under harsh nutrient environmental conditions and may switch towards oxidative phosphorylation once the glucose and oxygen levels increase.

In order to further analyze the effect of the extracellular environment on cell homeostasis, IVD cells were defined as a fluid-filled membrane using mixture theory. The active ion transport process, which imparts momentum to solutes or solvent, was also incorporated in a supply term as it appears in the conservation of linear momentum. Meanwhile, the trans-membrane transport parameters (i.e hydraulic permeability and ion conductance) were experimentally determined from the measurements of passive cell volume response and trans-membrane ion transport using the differential interference contrast (DIC) and patch clamp techniques. This novel single cell model could help to further illuminate the mechanisms affecting IVD cell homeostasis. The objective of this project was to develop a multi-scale analytical model by incorporating experimentally determined IVD tissue and cell properties to predict the ECM environment and further analyzing its effect on cell energy metabolism and homeostasis. This work provided new insights into IVD degeneration mechanisms and cell based IVD regeneration therapies for low back pain.

ACKNOWLEDGEMENTS

My years studying for my PhD have been unbelievably rewarding both in academic career development and personal enjoyment. There are many people I would like to thank to for their guidance and help. First, I would like to express my sincere gratitude to my advisor, Dr. Hai Yao, for his constant guidance through each stage of this dissertation. Dr. Yao has always been an outstanding mentor and great friend in past years. He supported and facilitated me in pursuing a variety of scientific trainings, developing the independent and scientific way of thinking and approaching the problem, and learning to run a laboratory. Dr. Yao also constantly provided me motivation and confidence to grow as a scientific investigator and individual. The most important to me is knowing that his ultimate goal is always my success.

I would also like to express my sincere gratitude to my committee members; Dr. Martine LaBerge, Dr. Jiro Nagatomi, and Dr. Barton L. Sachs for their constant support and far-sighted advice. Their effort and contribution in this project significantly improved my work and broadened my understanding of scientific research. I would also like to thank Dr. Richard Swaja for his help, advice and encouragement. I would also like to thank all the students and postdocs in Clemson-MUSC Bioengineering program. They were always there when I needed them no matter for the research or personal life. I really appreciated their friendships and efforts in establishing such a nice and compatible community. I wish all of them more success in their future life. Finally, I would like to dedicate this dissertation to my parents, Bihua Zheng and Zhaosheng Wu, back in China for their selfless and extraordinary support during all the difficult times.

TABLE OF CONTENTS

LIST OF TABLES

LIST OF FIGURES

CHAPTER 1 GENERAL INTRODUCTION

1.1 Introduction

Back pain is a major public health problem in Western industrialized societies. It causes suffering and distress to patients and their families, and affects a large number of the population. Approximately 40.5 million people in the United States visiting hospitals and physician's offices had low back pain as the first diagnosis (NIH 2005). Low back pain primarily occurs in patients between 30 and 50 years of age, and affects men and women equally. It is the most common cause of work-related disability in people under 45 and is the most expensive disability, in terms of workers' compensation and medical expenses [1]. Its total cost, including direct medical costs, insurance, loss of production and disability benefits, is estimated at 85.9 billion in US, £12 billion per annum in the UK and 1.7% of the gross national product in the Netherlands [2, 3].

Back pain is strongly associated with degeneration of the intervertebral disc[4]. Although it is asymptomatic in many cases, disc degeneration [5] is also associated with sciatica and disc herniation or prolapse. Disc height changes the mechanics of the spinal column. Behavior of other spinal structures such as muscles and ligaments is likely to be negatively adversely affected. Moreover, compared with other musculoskeletal tissues, discs degenerate much earlier. In the age group of 11-16 years, the first unequivocal indication of degeneration in the lumbar discs was found [6]. About 20% of people in their teens have discs with mild signs of degeneration. Degeneration increases steeply with age, particularly in males, so that around 10% of 50-year-old discs and 60% of 70-year-old discs are severely degenerated [7]. Degeneration of the intervertebral disc will cause biochemical change of ECM components. Proteoglycan content drops dramatically with degeneration, causing associated changes in swelling propensity, osmotic pressure gradients, and electrochemical effects such as streaming potentials and streaming currents [8, 9]. Potent regulators of cellular biosynthesis and remodeling [10, 11] will therefore be affected. Another factor related with IVD degeneration is nutrient environment. A fall in nutrient supply leads to a lowering of oxygen tension, glucose concentration, change in pH (due to increased lactic acid concentrations) which could affect cell viability, proliferation rate, energy metabolism and the ability to synthesize and maintain the disc's extracellular matrix. It may ultimately result in disc degeneration.

The IVD is the largest avascular structure in the human body. The nutrients that disc cells require for maintaining disc health are supplied by blood vessels at the margins of the disc. There are two possible pathways for nutrient transport into IVD, one route is through the CEP and the other is through the periannular [12]. Transport of fluid and solutes (including ions) in tissue is mainly governed by transport properties such as hydraulic permeability and solute diffusivities [13, 14], which are all mechanical strain dependent. Although many studies have been done to determine the mechanical and transport properties of annulus fibrosus (AF) and nucleus pulposus (NP), data for CEP is still rare. Consequently, the CEP properties were investigated in this research.

The balance between the rate of nutrient transport through the matrix and the rate of consumption by disc cells determines the local nutrient concentration gradient within the IVD. The nutrient consumption is related to cell energy metabolism. Although there are a few studies on articular cartilage chondrocytes and IVD cells in animal models [15-

18], to our knowledge, there is no study examining human disc cell energy metabolism. Based on previous studies, porcine and bovine IVD cells obtain their energy primarily through glycolysis, even in the presence of oxygen. Nevertheless, IVD cells, as well as chondrocytes, require oxygen to function [16-18]. The pathways of oxygen utilization by chondrocytes and IVD cells remain obscure. The rates at which chondrocytes and IVD cells metabolize glucose and consume oxygen depend on the local concentration of nutrients. Our studies addressed this by measuring the energy metabolism properties of human IVD cells under various nutrient environments.

Since the in vivo biomechanical response, transport of solutes and cellular activities in human IVD are difficult to determine, numerical simulation using finite element model (FEM) became an essential tool to help understand the biomechanical and nutrient environment in the IVD. Earlier studies have been limited to analyzing the nutrient solutes diffusion inside the disc and which did not include biomechanical loading [19, 20]. Recently, some investigators have developed finite element models based on mixture theory to analyze the effects of static and dynamic loading on solute transport inside the disc [21-24]. However, to our knowledge, effects of cartilage endplate on nutrient transport (diffusion and convection) inside human IVD under physiological loading condition were not clear. Furthermore, injection of IVD cells/stem cells in the NP region was proposed for IVD regeneration in cell based therapy for low back pain treatment [25-27]. Deteriorated ECM nutrient environment in the degenerated disc could be further changed due to the increase of cellular nutrient metabolism, therefore accelerating the process of degeneration. Until now, effect of nutrient concentration gradient on this therapy was still not investigated. In this research, we further developed a multiphasic finite element model to analyze the effects CEP and NP cell injection on extracellular nutrient environment inside the human IVD.

Changes in both the extracellular osmotic and nutrient environment in tissue level may be transduced into cellular level therefore affect various cell behaviors. As a signal for cell proliferation and matrix synthesis [28], cell homeostasis (volume regulation process) was found to be very sensitive to the ECM environment [29-31]. In previous studies, both passive and active cell volume responses of articular chondrocytes were analyzed under various osmotic loading conditions [28, 32-36]. Recently, cell membrane properties (hydraulic permeability and diffusivity of neutral solutes) in bovine articular chondrocytes were calculated by curve fitting real time cell volume data using Boyle-van't Hoff and Kedem & Katchalsky equations [37]. Compared to articular chondrocytes, different cell volume responses were observed in porcine IVD cells which may indicate different cell volume regulation mechanisms [35, 38]. However until now, there is no further research about cell homeostasis mechanisms in IVD cells. In this research, in order to quantitatively analyze the transport of fluid and solutes in relation to the mechanism of cell volume regulation, cell membrane modulus (hydraulic permeability, ion conductivity, etc.) were measured.

Previously, Boyle-van't Hoff and Kedem & Katchalsky equations [39] were used to simulate passive trans-membrane water and ion transport under various osmotic conditions. However, mechanical effects such as the cell membrane tension force or physicochemical factors such as the solute partition effect could not be considered. A more general mixture theory approach [40] was developed to incorporate these factors. Fundamental governing relationships for mechano-electrochemical transduction effects such as streaming potential, streaming current, diffusion (membrane) potential, and electro-osmosis could be deduced using this mixture theory. Specifically, stress, strain, and fluid velocity fields through a membrane during a one-dimensional steady diffusion process was simulated using this theory. Exchange of Na^+ and Ca^{2+} through the membrane were also analyzed [14]. Recently, several types of cell models were used to simulate passive cell volume response of articular chondrocytes and IVD cells by defining the cell as fluid-filled membrane or hydrogel/perfect osmometer like cytoplasm plus fluid filled membrane using the mixture theory [41, 42]. However, until now, there is no single cell model for trans-membrane ion transport coupled with water transport and membrane tension under cell homeostasis. Based on multiphasic theory, we developed a single cell model which could model the interactions of solid, fluid, and solutes (ions and neutral solutes) constituents in the cell membrane.

1.2 Objective and Specific Aims

The ultimate goal of this project is to fill the gap by incorporating experimentally determined IVD tissue and cell properties into a multi-scale analytical model capable of predicting the ECM environment and further analyzing its effect on cell energy metabolism and homeostasis. Our general hypothesis is that the CEP regulates the ECM osmotic and nutrient environment which further regulate IVD cell energy metabolism and homeostasis. Since the IVD is the largest avascular structure in the human body. The nutrients that disc cells require for maintaining disc health are supplied by blood vessels at the margins of the disc. A thin layer of hyaline cartilaginous end-plate (CEP) at the superior/inferior disc-vertebral interface, plays an important role in nutrient transport as well as load distribution in the IVD [43]. Recent studies have shown that the levels of oxygen and glucose significantly affect cell proliferation, cell energy metabolism, and matrix synthesis of bovine and porcine IVD disc cells in vitro [15-18, 44, 45]. This suggests that the transport of nutrients through the CEP and extracellular matrix (ECM) plays a key role in maintaining the physiological concentration of nutrients as well as the IVD cell energy metabolism and homeostasis. Deviations from physiological levels imply the initiation of tissue remodeling and matrix degradation. Therefore, we studied mechanical and transport properties of CEP and predicted ECM environment of human IVD with a multiphasic finite element model by incorporating experimentally determined tissue and cell properties. The resulting changes in cell energy metabolism and homeostasis were then studied to better understand the biological consequence. In order to achieve these goals, we propose the following specific aims.

Aim 1: Develop a multiphasic mechano-electrochemical finite element model of the IVD. Based on our previous studies of constitutive modeling of hydrated soft tissues, the IVD tissue will be modeled as a charged, fluid-saturated, inhomogeneous poroelastic medium consisting of solid, fluid, ions, and nutrients. Specifically, we will: **1a)** further develop a 3D mechano-electrochemical finite element model of human IVD by incorporating the CEP and the source terms for cell energy metabolism; **1b)** study the effect of calcification of the CEP and cell injection in cell based therapies for low back pain in the human IVD ECM environment.

Aim 2: Characterize mechanical and transport properties of the CEP. Knowledge of mechanical and transport properties of the CEP and its relationship with tissue composition is crucial for elucidating the mechanical function of the CEP and studying its effect on fluid and nutrient transport inside the IVD. Therefore, we will: **2a)** determine compressive aggregate modulus of the CEP using confined creep compression test; **2b)** determine biochemical properties of CEP and correlate with its mechanical and transport properties.

Aim 3: Determine IVD cell nutrient metabolic rates in relation to local nutrient levels. The nutrient gradients within IVD are dependent on the balance between diffusion transport rates through the tissue and consumption/production rates of disc cells. We will determine oxygen consumption rates (OCR) and glucose consumption rates (GCR) of IVD cells in different regions under various nutrient levels.

Aim 4: Develop a multiphasic single cell model to simulate the trans-membrane water, ions and neutral solute transport under homeostasis. Based on previous studies, IVD cells could be modeled as a water-filled membrane using the triphasic theory. The cell membrane was considered as a multiphasic mixture which includes a solid phase (cytoskeleton), a fluid phase (interstitial fluid), and solute phases (ions and neutral solutes). We will: **4a**) further develop a single cell model by incorporating membrane tension and ions transport; **4b**) study the trans-membrane water, neutral solute and ion transport under homeostasis.

Aim 5: Characterize the trans-membrane water and ion transport properties of IVD cells. IVD cells maintain homeostasis under different ECM osmotic and nutrient environment by adjusting water and ion transport through its membrane. We will: **5a**) determine hydraulic permeability of IVD cells from cell volume experiments; **5b**) determine ion conductance of IVD cells using patch clamp technique.

1.3 Organization of Dissertation

The following manuscript is organized in chapters of related studies that combine to form the overall aims of this project. In Chapter 2 we presented a comprehensive overview of physiology (anatomy, biochemistry, and function) and pathophysiology (disc degeneration) of human IVD. The homeostasis of articular chondrocytes and IVD cells were also outlined. This chapter also described previous single cell modeling methods about cellular mechanical environment and trans-membrane water and ion transport. In Chapter 3, a multiphasic mechano-electrochemical finite element model of IVD was developed based on triphasic theory. Detailed formulation of the specialized triphasic theory for charged IVD tissue was presented. The IVD tissue was modeled as a mixture with four phases: solid phase with fixed charges, interstitial water phase, ion phase with two monovalent species (e.g., Na^+ and Cl^-), and an uncharged nutrient solute phase. In this chapter, fundamental governing equations for the mixture, such as electro-neutrality condition, continuity equations, linear momentum equations and constitutive equations were given. In Chapter 4, the weak form formulation of mixture model developed in Chapter 2 was used for finite element analysis of physical signals and nutrient solute transport inside human IVD. The numerical results of this study showed that calcification of the cartilage endplate could significantly reduce the nutrient levels in human IVD. It also showed that in cell based therapy for IVD regeneration, excessive numbers of injected cells may cause further deterioration of the nutrient environment in the degenerated disc. In Chapter 5, the biphasic mechanical properties of cartilage endplate were measured to characterize its mechanical and transport behaviors which were also correlated with its histological and biochemical properties. The results of this study showed that cartilage endplate could block rapid solute convection, which allowed pressurization of the interstitial fluid and played a significant role in nutrient supply in response to loading. The study indicated that the cartilage endplate was unique in regards to its structure and function. In Chapter 6, the oxygen consumption rates of human IVD cells were measured under different glucose environmental conditions. Meanwhile, glucose consumption rates and lactate production rate of human IVD cells were measured under different oxygen conditions. These studies showed that energy metabolism rates of human IVD cells were significantly dependent on nutrient environment. In Chapter 7, a multiphasic single cell model was developed to simulate the trans-membrane water and ion transport based on multiphasic theory. The IVD cells were modeled as a water-filled membrane with solid phase, water phase, ion phase and neutral solute phase. This is the first single cell model for cell homeostasis which is capable of simulating the interaction of mechanical tension force and ion transport. Furthermore, active ion transport during cell homeostasis was also incorporated in the model by adding a unique source term in the momentum equations based on classical non-equilibrium thermodynamics [46-48]. In Chapter 8, trans-membrane water and ion transport during cell homeostasis was characterized by passive cell volume response and patch clamp experiments. Hydraulic permeability and ion conductance for IVD cells were measured. Chapter 9 outlined the overall conclusions of this project and identified future directions of this work.

CHAPTER 2 BACKGROUND

2.1 Physiology and Pathophysiology of Human IVD

2.1.1 Anatomy of Human IVD

The IVD is the largest avascular cartilaginous structure in the human body. It lies between the vertebral bodies, linking them together (Figure 2.1). They are the main joints of the spinal column and occupy one-third of its height. Their major role is mechanical, as they constantly transmit loads arising from body weight and muscle activity through the spinal column. They provide flexibility, allowing bending, flexion and torsion. They are approximately 7–10mm thick and 4 cm in diameter (anterior–posterior plane) in the lumbar region of the spine [49, 50]. The intervertebral discs are complex structures that consist of a centrally-located NP surrounded peripherally by AF. At each end of the disc, where the IVD meets the vertebre, there is a thin hyaline cartilage layer called the endplate.

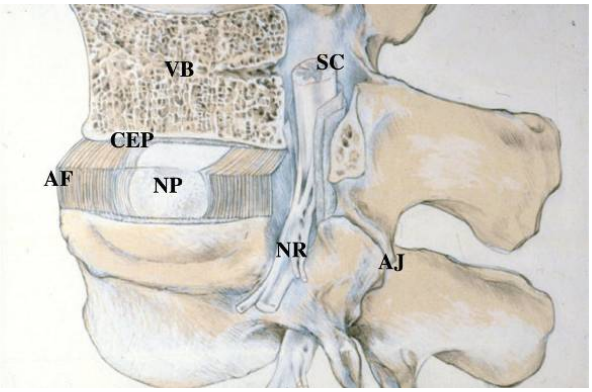

Figure 2.1 Anatomy of human IVD [51].

Nucleus Pulposus

The central nucleus pulposus matrix contains type II collagen and proteoglycan, mainly aggrecan [50]. Collagen fibers in the central nucleus pulposus are organized randomly [52] and elastin fibers (sometimes up to 150 mm in length) are arranged radially [53] (Figure 2.2). These fibers are embedded in a highly hydrated aggrecan gel. Cells in the NP are chondrocyte-like cells with a low density (approximately 5000/mm^3) [54]. The type II collagen fibers are not believed to give the same level of order to the structure or the same degree of mechanical stability to the matrix as in articular cartilage. The proteoglycans are hydrophilic, which could cause the NP to swell. The swelling pressure of the NP proteoglycans is constrained by the end-plates above and below as well as the annulus fibrosus around the periphery.

Annulus Fibrosus

The boundary between the NP and AF becomes distinct in young individuals (<10 years). AF is made up of a series of 15 to 25 concentric rings, or lamellae [49] (Figure 2.2). Collagen fibers lie parallel within each lamella. There are also elastin fibers lying between the lamellae. They help the disc to return to its original arrangement after bending by flexion or extension. They may also bind the lamellae together [53]. The annulus cells, particularly in the outer region are elongated, thin, fibroblast-like and are aligned parallel to the collagen fibers. However, the cells in the inner annulus are more oval. Both AF and NP cells can have several long, thin cytoplasmic projections, which may be more than 30 mm long [55, 56]. These features are not observed in articular chondrocytes. These may act as sensors and communicators of mechanical strain within the disc [55].

Cartilage Endplate

The third morphologically distinct region is the cartilage endplate. This structure consists of a layer of cartilage that covers the central parts of the inferior and superior cortical bone surfaces of the vertebral bodies. This serves as an interface between the disc and the vertebral body. The endplate ranges in thickness from 0.1 to 1.6 mm with a mean value of 0.62±0.29 mm [57, 58]. The collagen fibers within it run horizontal and parallel to the vertebral bodies, with the fibers continuing into the disc [57]. Numerous cells interspersed among the matrix tend to be aligned along the fibers. The collagen fibers from the disc appear to continue into the endplate, turning through approximately 120 degree from the lamellae of the outer annulus and 90 degree from the nucleus at the disc-endplate interface.

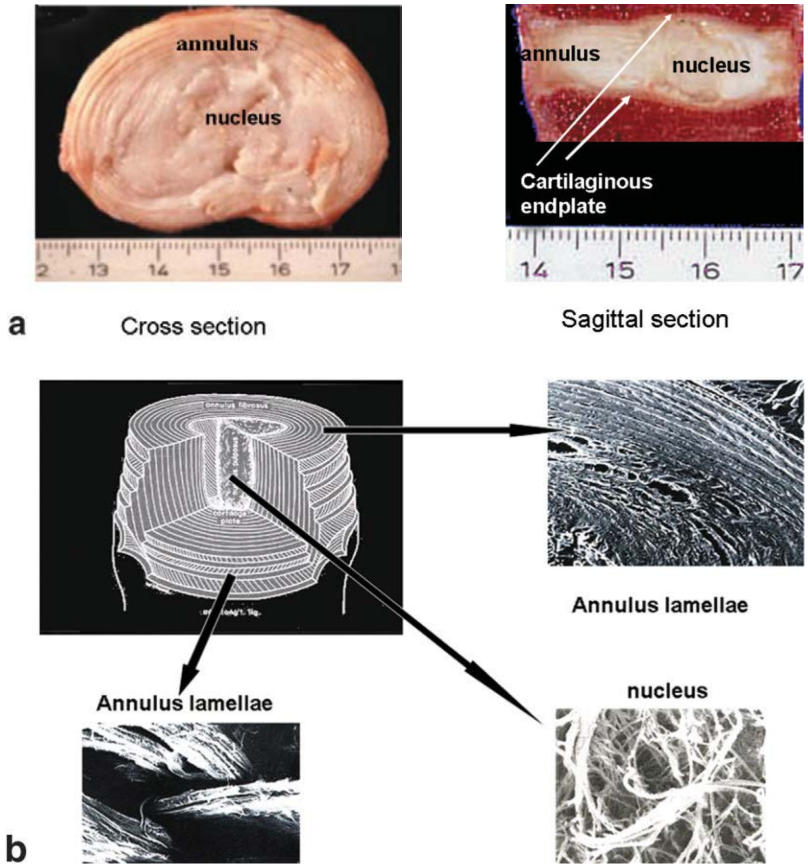

Figure 2.2 Morphology of human IVD [52]. a: Cross-section and sagittal sections through adult human discs. b: Schematic view of the collagen network of the disc.

2.1.2 Biochemical Composition of IVD and Function

Water

Quantitatively, the major component of the disc is water that contains ions which is governed by the matrix glycosaminoglycans (GAGs). The nutrients essential for cellular survival and the cellular metabolites are transported in the water phase. The interstitial water also contains bioactive molecules such as growth factors from the blood, soluble factors produced by cells, and degraded extracellular matrix fragments. The concentrations of all these molecules are all very low. The concentration of water varies with position in the disc and age [57]. In general, the nucleus pulposus in the central region of the disc is the most hydrated. The water content of the nucleus in an infant can reach 90%, and falls to around 80% in the non-degenerated disc of a young adult [59]. Comparatively, the water content of the annulus is lower than that of the nucleus. It falls to around 65% in the outer annulus in adult humans. Water content also varies with load. In the lumbar discs, mechanical forces cause a diurnal change in hydration. Loads on the disc are imposed by body weight but more importantly by muscle activity and ligament tensions. They undergo a diurnal cycle [60] with pressures generated inside the disc. Forces are lowest at night during rest and increase dramatically during the day time. Loads are also higher when sitting than when standing. Water is lost during the day due to increases in load on the disc and is regained at night when the load is removed. About 25% of the disc's water is lost and regained during this diurnal cycle in young highly-hydrated lumbar discs [61]. This diurnal water cycle results in changes in height of the disc and total body height of up to 2.5 cm [62]. Most highly hydrated disc can be turgid which will also affects the disc's mechanical properties [63].

Collagen

Collagen is the main macromolecular component of the disc [64]. Highly organized collagen fibrils form the framework of the disc. These anchor to the bone and provide tensile strength. The lamellae of the annulus are formed from collagen bundles which are firmly anchored to the adjacent vertebral bodies. These run at an oblique angle to the axis of the spine, while the angle is reversed in adjacent lamellae [52]. The collagen content of the disc is highest in the outer annulus which is as much as 70% by dry weight. It falls to around 20% to 30% of the dry weight in the nucleus of adult human lumbar discs [65]. Collagen content is very low in the nucleus of infant discs which is highly hydrated. The major molecular species of the fibrils are Type I (found in ligament, skin, and tendon) and Type II collagens (found in hyaline cartilages). Type I content is highest in the outer annulus, decreasing radially toward the nucleus region. Type II collagen follows the reverse radial gradient [65].

Aggrecan

Aggrecan is the major proteoglycan of the disc [62], and is responsible for maintaining tissue hydration through osmotic pressure due to its constituent chondroitin and keratan sulfate chains [62]. The proteoglycan in the nucleus is around 15% of the wet weight while it is approximately 5% of the wet weight in the annulus. Aggrecan is a very large molecule which consists of a protein core and around 100 GAG side-chains are attached to the core. Many aggrecan molecules attach to hyaluronan chains via a globular region (G1 domain) at one end of the protein core which form large aggregates (hence the name "aggrecan"). These aggregates are trapped in the disc by the surrounding collagen network. The GAGs maintain tissue hydration and determine the ionic composition of the interstitial fluid. They contain anionic groups (SO_3^- and COO^-), which impart a net negative charge to the matrix. The interstitial water contains an excess of cations and a deficit of anions in order to maintain electro-neutrality. The concentrations of negatively charged solutes, particularly anions such as Cl^- are therefore lower than in the plasma, while those of positively-charged species are higher. The major cation in the disc is Na^+ and its concentration is directly related to concentrations of fixed negative charge related to GAG concentration. Na^+ is highest in the nucleus and lowest in the outer annulus and is affected by load-induced changes in hydration and changes in GAG concentration. This high concentration of Na^+ imparts a high osmotic pressure to the tissue, which consequently tends to gain water. The ionic osmotic pressure is functionally important for the disc, as it governs the swelling pressure and the ability of the disc to maintain hydration and turgidity under loading condition [66]. Moreover, the ECM of all three structures (NP, AF and CEP) is highly regulated by continuous matrix breakdown and synthesis which are controlled by the cells in the matrix.

Other Macromolecules

The disc also contains a large number of other macromolecules in addition to collagens I, II and aggrecan. The concentrations are much lower, but they are important for maintaining disc matrix integrity and function [67]. Some of these appear to be important structurally and biomechanically, such as elastin and elastic microfibrils and collagen IX [64]. Others, such as the small proteoglycans decorin, fibromodulin, the cartilage oligomeric matrix protein (COMP), are involved with matrix assembly and organization. Proteins such as cartilage intermediate layer protein (CILP) may bind growth factors [68]. Some polymorphisms of these molecules even appear to predispose to premature disc degeneration [69].

Relation of IVD and Cartilage Tissue

The intervertebral disc is often likened to articular cartilage, and does resemble it in many ways, particularly in regard to biochemical components. However, there are significant differences between the two tissues. One of these is the composition and structure of aggrecan. IVD aggrecan is more highly composed with keratan sulphate than that found in the deep zone of articular cartilage. In addition, the aggrecan molecules are less aggregated (30%) and more heterogeneous in the disc compared with articular cartilage (80% aggregated) from the same individual [53]. Disc proteoglycans become increasingly difficult to extract from the matrix with increasing age [62]. The reason may be extensive cross-linking, which appears to occur more within the disc matrix than in other connective tissues.

2.1.3 IVD Cells Morphology and Phenotype

NP Cells

In the early embryo, the cells of the nucleus are notochordal cells, with cell clumps joined by gap junctions. Meanwhile, the matrix is highly hydrated and translucent while macromolecules in the matrix differ from those of mature human discs [70, 71]. By early adulthood in the human, the nucleus becomes populated by chondrocyte-like cells that may migrate from the adjacent endplate or inner annulus fibrosus regions [72]. In adulthood, the cell population varies with species. In some cases, such as those of the rabbit, rat, pig, and dogs, notochordal cells persist well into adult life, whereas in cattle, notochordal cells have virtually disappeared by birth. In humans, notochordal cells are present in infancy, but disappeared by 4 to 10 years of age [73]. They are replaced by chondrocyte-like cells, which may be closely packed, and contain smaller and more densely packed nuclei. Cells in the mature nucleus pulposus may extend small cytoplasmic processes [74, 75] similar to those reported for bovine nucleus pulposus cells [76]. These same cells stain intensely for vimentin intermediate filaments, F-actin and cytokeratins which are similar to chondrocytes (Figure 2.3).

AF Cells

Cells of the annulus fibrosus originate from the mesenchyme and exhibit many characteristics of fibroblasts and chondrocytes [77] such as synthesis of types I and II collagen and aggregating proteoglycans [78]. For the most part, these cells have an ellipsoidal morphology, with long axes that align with the oriented collagen fibers within lamellas, and aspect ratios of long to short axes (i.e., R1:R2) between 2 to 7 [55, 79] (Figure 2.3). Cells within the inner annulus fibrosus regions are more rounded, sparsely distributed, and may be surrounded by a pericellular matrix region rich in types III and VI collagen, which is termed as chondron [80]. Recent studies have revealed the existence of a population of “interlamellar” cells, with a more flattened, “disc-shaped” morphology [56] that may reflect their existence within a different biochemical and structural environment. Cells of the annulus fibrosus exhibit staining for F-actin (Figure 2.3). Annulus fibrosus cells also display thin cytoplasmic projections that stain for both actin microfilaments and vimentin intermediate filaments [55, 74]. In some regions of the annulus fibrosus, cell processes may elongate or branch out within single lamellas or may branch in multiple directions, as observed for the “stellate” cells of the interlamellar regions. These cell projections have been observed in human, bovine, rat, and porcine IVDs with varying frequency. However their mechanical role remains unknown.

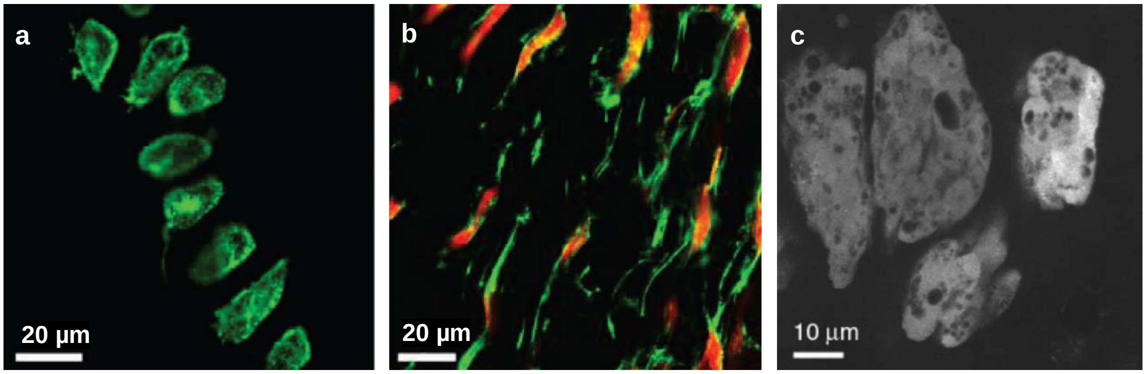

Figure 2.3 Morphology of IVD cells in different regions [81, 82]. a: Inner AF cells. b: Outer AF cells within an immature porcine IVD stained for F-actin using fluorescent phalloidin. Outer cells are dual-labeled with cytoplasmic stain. c: Nucleus pulposus cells within the rat lumbar IVD stained with calcein-AM to label cytosol.

2.1.4 Disc Degeneration

Changes in Tissue Composition and Structure

The most significant biochemical change to occur during disc degeneration is loss of proteoglycan which parallels the degeneration grade [83] (Figure 2.4). The aggrecan molecules become degraded, with smaller fragments being able to leach from the tissue more readily than larger portions. This results in loss of glycosaminoglycans which is responsible for the fall in the osmotic pressure of the disc matrix and a loss of hydration. However, even in degenerated discs, the disc cells can retain the ability to synthesize large aggrecan molecules, with intact hyaluronan-binding regions, which have the potential to form aggregates [84]. Less is known of how the small proteoglycan population changes with disc degeneration, although there is some evidence that the amount of decorin, and more particularly biglycan, is elevated in degenerated human discs as compared with normal ones [85].

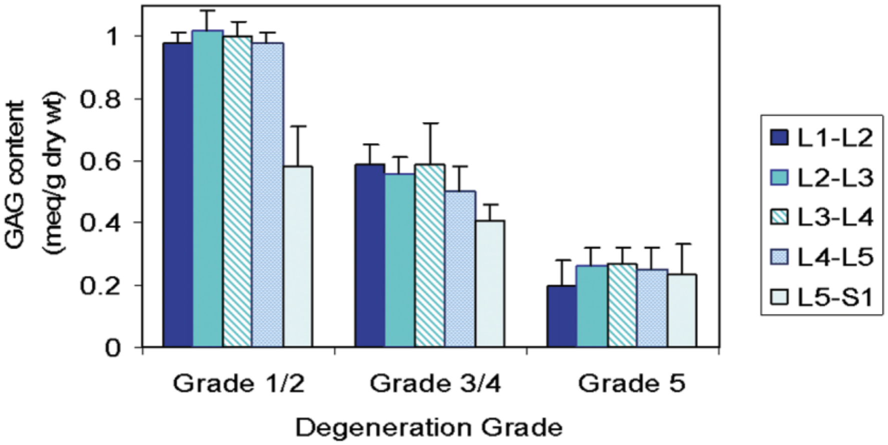

Figure 2.4 Fall in GAG concentration with increase in degeneration grade [83].

Although the collagen population of the disc also changes with degeneration of the matrix, the changes are not as obvious as those for proteoglycans. The absolute quantity of collagen changes slightly but the types and distribution of collagens can alter significantly. For example, there may be a shift in proportions of types of collagens found and their distribution within the matrix. In addition, the fibrillar collagens, such as type II collagen, become more denatured due to enzymic activity. As with proteoglycans, the triple helices of the collagens are more denatured and ruptured than those found in articular cartilage from the same individual. The amount of denatured type II collagen increases with degeneration [59]. However, collagen cross-link studies indicate that new collagen molecules may be synthesized at early stage of disc degeneration in an attempt to repair the damage [86].

Other components can change in disc degeneration and disease in either quantity or distribution. For example, fibronectin content increases with increasing degeneration and becomes more fragmented [87]. These elevated levels of fibronectin could reflect the response of the cell to an altered environment. The formation of fibronectin fragments can then feed into the degenerative cascade because they have been shown to down regulate aggrecan synthesis but to upregulate the production of some matrix metalloproteinases (MMPs) in vitro systems.

Changes in Disc Cells

Little is known about changes in cell morphology specific to IVD degeneration. Decreases in cell density and the incidence of necrotic cells have been commonly reported for aged nucleus pulposus [6], but may not be specifically linked to IVD degeneration. Clusters of proliferating cells are a commonly observed but not consistent feature of IVD degeneration [88]. A study by Johnson and Roberts (2003) suggests that the prevalence of cell cytoplasmic projections may be greater in the scoliotic IVD. Another important feature of IVD degeneration is an increased presence of other cell types including nerve fibers, Schwann cells, endothelial cells, and fibroblasts associated with increased vasculature [6]. Finally, the glycosaminoglycan content changes dramatically with degeneration, with associated changes in swelling propensity, osmotic pressure gradients, and electrochemical effects such as streaming potentials and streaming currents [10, 11]. Incorporation of osmotic pressure and electrokinetic effects will be critical in future work to evaluate the effects of changes in these factors on micromechanical stimuli, specifically cell volume change which may occur with degeneration in the IVD. It will also be important in evaluating the related effects on IVD mechanotransduction.

2.1.5 Nutrient Environment and Disc Degeneration

Nutrient Transport

The disc is large and avascular and the cells depend on blood vessels at their margins to supply nutrients and remove metabolic waste. The pathway from the blood supply to the nucleus cells is precarious because these cells are supplied virtually entirely by capillaries that originate in the vertebral bodies. The capillaries penetrate the subchondral plate and terminate just above the cartilaginous endplate [89]. Nutrients must then diffuse from the capillaries through the cartilaginous endplate and the dense extracellular matrix of the nucleus to the cells. The distance could be as far as 8 mm from the capillary bed (Figure 2.5). There are several factors that could significantly affect the blood supply to the vertebral body such as atherosclerosis, sickle cell anemia, Caisson disease, and Gaucher’s disease [90]. All of these factors appear to lead to a significant increase in disc degeneration. Long-term exercise or lack of it appears to have an effect on movement of nutrients into the disc, and thus on their concentration in the tissue [91]. The mechanism is not known but it has been suggested that exercise affects the architecture of the capillary bed at the disc–bone interface. Finally, even if the blood supply remains undisturbed, nutrients may not reach the disc cells if the cartilaginous endplate calcifies [92]. Intense calcification of the endplate is frequently observed in scoliotic discs.

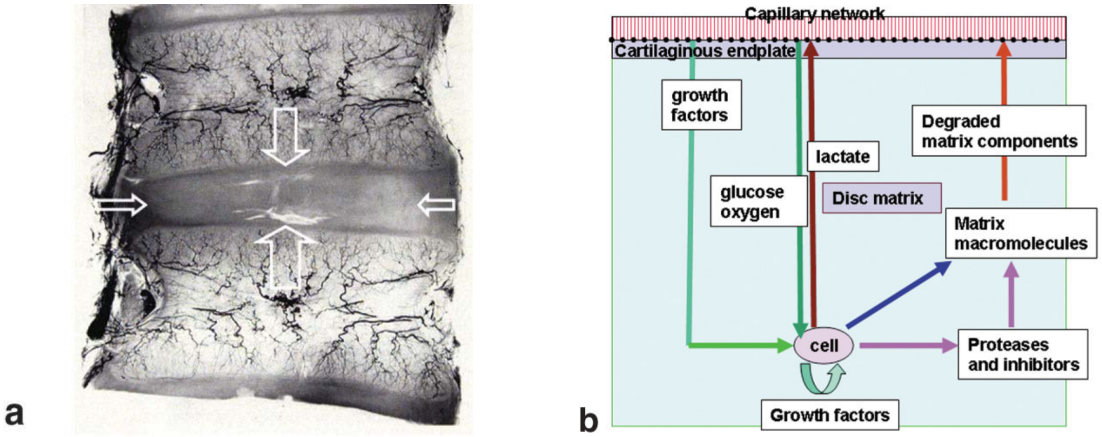

Figure 2.5 Pathways for nutrient supply to the disc cells [93]. a: The avascular nature of the disc compared with the vertebral body and ligaments. b: Schematic showing transport between the blood supply and the disc.

Cell Metabolism

One of the primary causes of disc degeneration is thought to be failure of the nutrient supply to the disc cells [12]. Like all cell types, the cells of the disc require nutrients such as glucose and oxygen to remain alive and active. For the disc cells to remain viable, the levels of extracellular nutrients and pH must remain above critical values. Because disc cells obtain adenosine triphosphate (ATP) primarily by glycolysis, glucose is a critical nutrient. Cells start to die within twenty-four hours if the glucose concentration falls below 0.2 mM, and at this concentration, the efficiency of glucose transport into the cell is likely reduced [94]. The rate of cell death increases when pH levels are acidic; cell viability is reduced even with adequate glucose at pH 6.0 [15] (Figure 2.6). Although necessary for maintaining matrix synthesis, oxygen is not required for maintaining disc cell viability. Disc cells can remain viable for many days with no oxygen present [15, 44]. It supports the findings that these cells produce ATP primarily through glycolysis (Figure 2.6). Thus, it appears that local nutrient and pH levels must be maintained within certain limits to allow optimal cell activity. However it is still not well defined. Moreover, if these nutrient levels fall below the critical value, disc cells will die. However whether death occurs by apoptosis or necrosis is unknown.

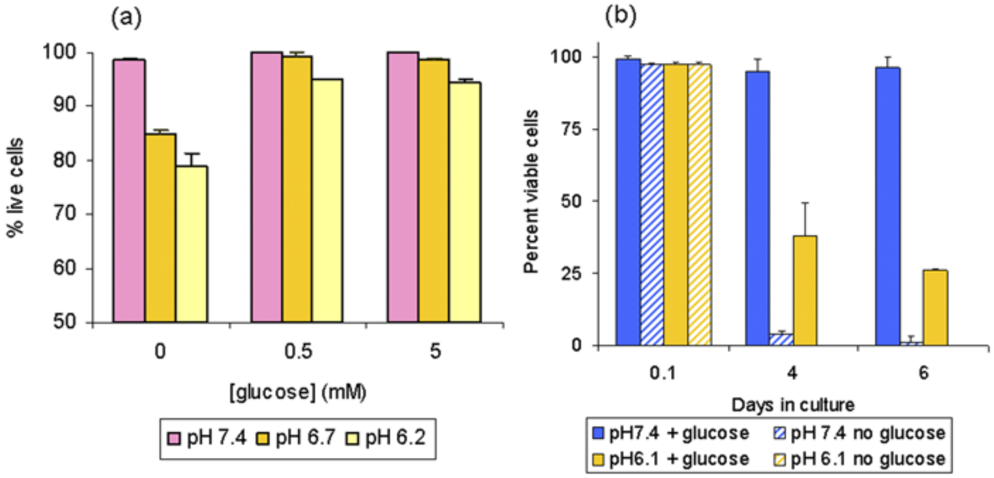

Figure 2.6 Effect of nutrient-metabolite concentrations on survival of disc cells [15]. a: Cells were cultured at 0% oxygen for 24 hours. b: Cells were cultured at 0% oxygen for 6 days.

Disc cell energy metabolism also is regulated by extracellular oxygen concentrations and extracellular pH. The rates at which disc cells metabolize glucose, consume oxygen and produce ATP depend on the local acidity and concentration of nutrients [95]. However, the effect of oxygen concentration on metabolism rates is still unclear. In some studies, low oxygen has been observed to diminish the rate of glycolysis which is known as negative Pasteur Effect. However, the opposite phenomenon has been found in other studies. Glycolysis rates rising during low oxygen is known as a positive Pasteur Effect [95, 96]. The reasons for these differences are still unclear. Moreover, all studies have found that an acidic pH level significantly reduces the rates of glycolysis and the rate of oxygen uptake, and hence the production of ATP [95, 97]. Other factors such as growth factors, changes in the stresses in the surrounding matrix, and the osmotic environment also have been observed to influence the energy production rates [98].

Matrix Synthesis

During in vitro studies, the activity of disc cells is very sensitive to extracellular oxygen and pH, with matrix synthesis rates significantly affected by nutrient environment. Synthesis rates appear to be highest at around 5% oxygen [96]. However, once oxygen tension falls below 5%, synthesis is inhibited significantly in an oxygen-tension-dependent manner. Sulfate incorporation rates at 1% oxygen are only one-fifth of the rates at 5% oxygen. In other cell types, gene expression was affected by low oxygen [99], but there is little information on disc cells. Extracellular pH also has a significant effect on the synthesis rates of matrix components; rates at pH 7.0 were 40% higher than at pH 7.4. However synthesis fell steeply once the environment became acidic [97]. By contrast, extracellular matrix degradation appears less sensitive to pH. Thus, acidic pH levels may increase the rate of matrix breakdown by inhibiting synthesis but not degradation. In conclusion, a fall in nutrient supply that leads to a lowering of oxygen tension or pH could therefore affect the ability of disc cells to synthesize and maintain the disc’s extracellular matrix and could ultimately lead to disc degeneration.

2.2 Homeostasis of Articular Chondrocytes and IVD Cells

Total number of cellular osmolytes will be changed due to the shift of metabolism toward either anabolism (synthesis) or catabolism (degradation). It will thus cause osmotic perturbation. It is found that hormones regulate metabolism in liver cells which cause cell volume changes [100]. Membrane transport activities will induce changes of intracellular osmolarity thus inducing cell volume changes. Therefore, cell volume regulation even happens in an "isotonic" milieu due to cell activity-associated osmotic perturbation. Regulatory volume increase (RVI) and regulatory volume decrease (RVD) are used by many animal cell types to cope with cell shrinkage and swelling due to osmotic shock. The mechanism of RVI is that NaCl or some organic solutes transport into the cytoplasm against the chemical potential gradient through the cell membrane. The mechanism of RVD is that KCl or some organic solutes transport out of cytoplasm. The ion transport readjusts the intracellular and extracellular osmotic environment thus leading to water flux through the cell membrane. The cell volume finally could reach equilibrium. When the osmolarity of extracellular solution is changed back to physiological level from the hypertonic and hypotonic conditions, the cell could have isotonic induced second RVD or RVI. These phenomena are termed as post-RVI RVD or post-RVD RVI (Figure 2.7). Most of the cell could have second RVD or RVI even some of them could not have primary RVD or RVI.

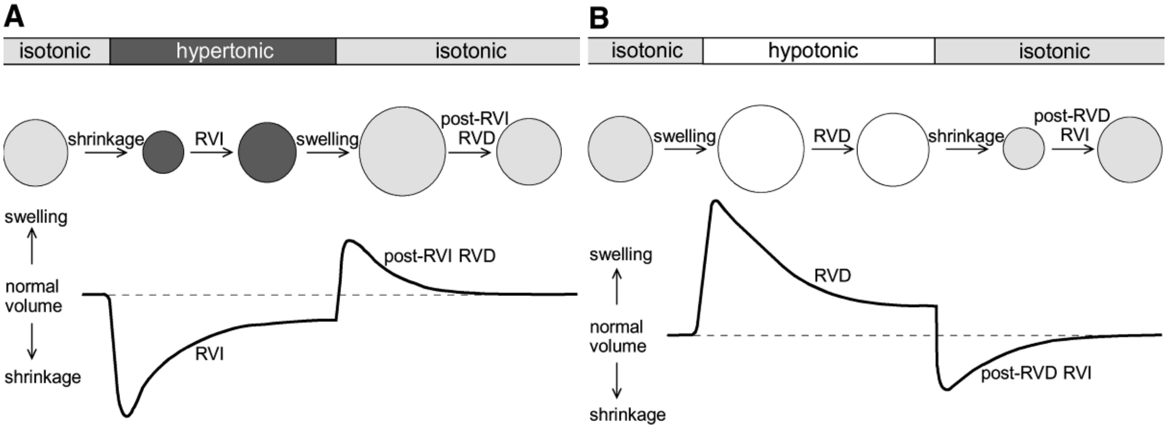

Figure 2.7 Non steady-state cell volume regulation under anisotonic conditions [31].

2.2.1 Passive Volume Regulation of Articular Chondrocytes

Effect of Extracellular Matrix (ECM)

Passive volume response of chondrocytes under hypotonic and hypertonic environment was analyzed by blocking the ion channels. Either inhibitors such as Benzenemethanol (REV 5901) or Bumetanide can be used [33]. Decreasing the temperature (4 °C) has also proved to be an alternative option [101]. Volume change of in situ chondrocytes was found to be similar with the isolated chondrocytes over 180 to 380 mOsm in bovine articular cartilage. Specifically, chondrocytes in mid zone (MZ) behaved following Boyle-van't Hoff law as a perfect osmometer. It means extracellular matrix will not restrict volume response of chondrocytes under these ranges of osmolarity change. However, rapid cell lysis was found for isolated chondrocytes under 180 mOsm while no further significant volume change occurred for in situ chondrocytes. Another interesting phenomena is that chondrocytes from the superficial zone (SZ) appear more sensitive to reduced osmolarity compared with MZ or DZ chondrocytes [33].

Effect of Cartilage Degeneration

Cartilage degeneration could affect PG content in the matrix thus affecting the ECM ion environment. It could change extracellular osmolarity [102, 103]. Based on Gibbs–Donnan equilibrium conditions, extracellular osmolarity in degenerated cartilage could be calculated. Over a wide range of extracellular osmolarity, the passive volume response of chondrocytes in human articular cartilage is not significantly different in non-degenerate or degenerate cartilage of the tibial plateau, or isolated from the ECM. However, at very low osmolarity, the swelling of chondrocytes within relatively non-degenerate cartilage was restricted, but was less so for in situ cells in degenerate cartilage and hardly at all for chondrocytes isolated from the ECM [101]. The most likely explanation is that the PG-rich chondron surrounding the chondrocyte could restrain further cell swelling at low osmolarity [104]. As for degenerated cartilage, the chondron surrounding chondrocytes was mechanically weaker thus has less restriction effect on chondrocyte swelling. Initial volume difference was also found in normal and degenerated articular cartilage. Chondrocyte volume within superficial and mid-zones, but not of deep zone cells was found to increase significantly with degree of degeneration. There was a 90% increase in the volume of MZ chondrocytes between grades 0 and 3 cartilage. However, there was not a linear relationship between chondrocyte volume and degree of cartilage degeneration, since the largest increase occurred between grades 1 and 2 [105].

Effect of Osmotic Loading Types

Significant different volume change response to static loading (4 min) and dynamic osmotic loading (0.0125 Hz, 4 min) were found in bovine articular chondrocytes [106]. For both types of loading, the average values of volume change (Δv) and time constant (τ) were significantly greater during the swelling response than the shrinking. Differences between Δv and τ observed during swelling and shrinking appear to be less evident at higher frequencies of osmotic loading compared to static osmotic loading experiments. The possible reason is that cell properties under absolute cell shrinking and swelling may be more similar at higher frequencies osmotic loading. Bovine articular chondrocytes also exhibited a trend of increasing changes in cell size with decreasing loading frequency. However, direct measurements of physiologic osmotic change in situ due to cartilage deformation are difficult [11,12]. The frequencies investigated in previous studies may represent those at the lower end of the physiologic range. All the studies may suggest the general phenomena that cell properties at static statue are different from transient statue. It may also reflect cell size-dependent, non-linear behavior of the cell properties in swelling and shrinking.

Effect of Long Term Culture

Cell volume of chondrocytes cultured in alginate beads for 12 days was found to vary with the extracellular osmolarity. The volume of cultured chondrocytes was highest at 280 mOsm, and lowest at 550 mOsm at both the interface and deep zones of alginate beads. Cell volumes at day 5 were similar to those at day 12 under all conditions tested implying adaptation to prevailing osmolarity over this culture period. No significant difference to change of osmolarity was found for cells from the interface zone and deep zone [28]. It is different from the explants result in which cells from the interface zone are more sensitive to the change of osmolarity [103, 107, 108]. Possible reasons for different cell volume response to osmolarity in isolated and in situ chondrocytes may include zonal variation in composition and fixed charge density (FCD) in native tissue, enzyme treatment when isolating the cells. Another interesting phenomena is that differences in initial cell volume in different regions in cartilage are reported to disappear in culture [109].

Effect of Solute Partition Coefficients

Intracellular partitioning of membrane-permeant solutes (glycerol, urea and other neutral solutes) could cause a partial volume recovery in response to osmotic loading based on prior theoretical and biomimetic experimental studies on articular chondrocytes [37, 110]. Osmotic loading with membrane-permeant glycerol (92 Da) and urea (60 Da) are observed to produce partial volume recoveries, whereas loading with 1,2-propanediol (76 Da) produces complete volume recovery. By curve fitting experimental results of partial volume recovery using standard Kedem-Katchalsky equations or triphasic theory, values for hydraulic permeability, water content, solute permeability and partition coefficient could be measured as shown in Table 2.1 [37]. For glycerol, the partition coefficient increases with osmolarity while urea exhibits no such dependence. Furthermore, a positive correlation between solute membrane permeability and the intracellular partition coefficient is observed. It was suggested that a solute’s cytoplasmic partition coefficient increases with increasing hydrophobicity [37].

Table 2.1 Curve-fitted material parameters from cell volume response experiments [37].

		Nonpermeating osmolyte curve-fit			Permeating osmolyte curve-fit			
Osmolyte	Osmolarity (mOsm)	Hydraulic permeability L_p (10^{-14} m^3/N•s)	Water content $\varphi^{w}{}_{ir}$	R^2	Solute permeability P^p (10^{-10} m/s)	Reflection coefficient σ	Partition coefficient $\kappa^{p}{}_{i}$	R^2
1,2 Propanediol	1000 ($n = 8$)	3.06 ± 1.35	0.55 ± 0.08	0.98 ± 0.01	843 ± 334	0.78 ± 0.15	1.00 ± 0.02	0.94 ± 0.04
	200 ($n = 7$)	2.47 ± 0.57	0.67 ± 0.06	0.99 ± 0.01	28.6 ± 14.4	0.82 ± 0.11	0.86 ± 0.09	0.93 ± 0.04
Urea	600 ($n = 8$)	3.14 ± 0.81	0.65 ± 0.08	0.98 ± 0.01	26.7 ± 15.7	0.77 ± 0.18	0.90 ± 0.02	0.95 ± 0.02
	1000 ($n = 8$)	3.16 ± 0.79	0.63 ± 0.06	0.98 ± 0.02	21.1 ± 12.9	0.75 ± 0.25	0.84 ± 0.07	0.93 ± 0.04
	200 ($n = 5$)	4.76 ± 1.94	0.58 ± 0.07	0.97 ± 0.03	5.38 ± 4.82	1.00 ± 0.00	0.48 ± 0.19	0.89 ± 0.05
	400 ($n = 5$)	4.40 ± 1.61	0.59 ± 0.06	0.99 ± 0.01	5.01 ± 3.11	1.00 ± 0.00	0.59 ± 0.11	0.93 ± 0.05
Glycerol	600 ($n = 5$)	4.36 ± 1.08	0.66 ± 0.08	0.99 ± 0.01	8.50 ± 3.58	0.85 ± 0.19	0.67 ± 0.04	0.92 ± 0.07
	1000 ($n = 7$)	5.50 ± 1.39	0.66 ± 0.06	0.99 ± 0.01	10.6 ± 2.83	0.59 ± 0.25	0.83 ± 0.06	0.94 ± 0.03

Measuring Techniques of Cell Volume Regulation

In order to capture the isolated or in situ cell images, label based methods such as fluorescent microscopy [105, 111] and label free methods such as phase contrast (PhC) or differential interference contrast (DIC) microscopy [112] could be used. As for label based methods, cells were stained with calcein-AM and z-stack confocal microscopy was used to record the cell image layer by layer. 3D reconstruction technique was used in calculating cell volume. However, fluorescent dyes have disadvantages, including potential cytotoxicity, the tendency to photobleach, and particularly for this case, a potential influence on the cell's response to osmotic changes. As for label free methods, 2D cell image captured using PhC or DIC technique was also used to calculate the cell volume. The sphere assumption was also needed. Normally, calibration using 3D fluorescent cell images by confocal microscopy is used for this method. The advantage of PhC or DIC technique is that it could capture the cell image in a short time and thus well record the process of cell volume response which is just several minutes [32, 35, 38, 113]. However, these methods require manually adjusting the focus plane during the cell volume change which potentially distorts the transient data. Recently, a new technique, quantitative phase analysis by wide-field digital interferometry (WFDI) is found to be useful for quantitatively recording cell volume response. Transient change of cell volume, area and dry mass could be recorded based on real time visualization of phase profile [114].

In order to analyze the passive volume response, ion channels have to be blocked to prevent regulated volume response. Benzenemethanol (REV5901) which blocks the osmolyte channel and Bumetanide (an inhibitor of the chondrocyte $Na^+\backslash K^+\backslash 2Cl^-$ cotransporter) could be used to inhibit ion channels [33]. Another method to inhibit ion channels is to keep the solution at low temperature (4 °C) since most of the ion channels only work properly at 37 °C [101]. NaCl was frequently used to adjust osmolarity in the saline solution. However it may change the ion environment thus affecting certain ion channel and cell function. Sucrose is commonly used now to change osmolarity of the saline solution. However it could change the nutrient environment thus affecting cell function.

2.2.2 Active Volume Regulation of Articular Chondrocytes

The ability of chondrocytes to regulate their volume under osmotic perturbation was proven by cell volume measurement. Regulated volume decrease of bovine articular chondrocytes was recorded using confocal microscope to visualize fluorescently-labelled cells. No significant RVD rate difference was found between SZ, MZ and DZ. No significantly different volume regulation rate was found between in situ chondrocytes and isolated chondrocytes [32, 34, 113]. It is possible that the signaling pathway involved in RVD remained intact after chondrocyte isolation and thus there is no role of cell-matrix interaction in mediating RVD. The measurements also confirmed that at the lower temperature, RVD was slower and more manageable analytically than at the ‘physiological’ temperature [32, 115].

The ability of regulate volume increase was proven using in situ and isolated chondrocytes which were loaded with calcein or fura-2. Following a 42% hyperosmotic challenge, chondrocytes rapidly shrunk, however, only 6% of the in situ or freshly isolated chondrocytes demonstrated RVI. This contrasted with 2D-cultured chondrocytes where 54% of the cells exhibited RVI. The rate of RVI was the same for all preparations. During the ‘post-RVD/RVI protocol’, 60% of the in situ and freshly isolated chondrocytes demonstrated RVD, but only 5% showed RVI [113]. The different RVD phenomena between in situ chondrocytes and isolated chondrocytes suggest that cytoskeletal integrity may play a role in regulating RVI activity. Another interesting phenomena is that no regulatory volume response was found in chondrocytes which is long term cultured in alginate bead. By day 5 and 12, around 20% swelling and 15% shrinkage were observed when the cells were cultured at 280 and 550 mOsm comparing to the cell volume at 380 mOsm [28].

2.2.2.1 Mechanism of Regulated Volume Decrease (RVD)

Taurine

In bovine chondrocytes, the increase in taurine flux following cell swelling was rapid both at normal (37 °C) and reduced (21 °C) temperature with no evidence of a lag phase at either temperature. The rate of taurine loss was significantly less at the later time points compared with those immediately following hypotonic shock. At comparable time points, the loss of taurine expressed as a percentage of total intracellular taurine at the initial time point was about two times greater at 37 °C than at the lower temperature [116, 117].

There was no marked difference in the sensitivity of the taurine transport pathway between in situ and isolated bovine articular chondrocytes exposed to similar osmotic challenges. Longer incubation of cartilage in anisotonic media has no subsequent response on the taurine transport pathway. For in situ and isolated chondrocytes, the point at which swelling-activated taurine efflux was stimulated (the "set-point") corresponded closely to the osmolarity of the incubation medium (180, 280 or 380 mOsmol/l). However, the volume of chondrocytes isolated into these media and measured by confocal microscopy was not different [117]. The data show that despite chronic exposure of chondrocytes to anisotonic media, the cells maintain a pre-determined volume that is the 'set-point' for the activation of the taurine transport pathway following acute hypotonic shock. The role of the pathway in RVD was determined in isolated calcein-loaded chondrocytes using fluorescence imaging. RVD was observed and inhibited by REV5901 (50 μM) and by NDGA (75 μM) [117]. However, the addition of compounds involved in activating RVD in other cell types (i.e. leukotrienes and lipoxins [118, 119]) directly to chondrocytes had no effect on the taurine transport pathway either in isotonic or hypotonic media. It suggests that the taurine pathway appears to play a role in chondrocyte RVD, but its activation does not involve metabolites of the arachidonic acid cascade[117].

Ca^{2+} and Actin

All cells showed an increase in Ca^{2+} at 250 mOsm and 96.9% of these cells demonstrated oscillations. When Ca^{2+} free medium was used to osmotically stimulate the cells, only 2.7% responded with a Ca^{2+} transient [36]. The effect was inhibited by thapsigargin which inhibit intracellular Ca^{2+} release or by removal of extracellular Ca^{2+}, indicating that the rise in Ca^{2+} reflects both influx from the extracellular medium and release from intracellular stores [115, 120]. Inhibition of the response by neomycin implicates activation of PLC and IP3 synthesis in the mobilization of Ca^{2+} from intracellular stores [120]. Pre-exposure to IL-1 significantly inhibited regulatory volume decrease (RVD) following hypo-osmotic swelling and reduced the change in cell volume and the time to peak Ca^{2+} in response to hyper-osmotic stress, but did not affect the peak magnitudes of Ca^{2+} [121, 122]. Insensitive to inhibitors of L-type voltage-activated Ca^{2+} channels (LVACC) or reverse mode Na^{+}/Ca^{2+} exchange (NCE) but could be significantly attenuated by ruthenium red, an inhibitor of transient receptor potential vanilloid (TRPV) channels and by Gd^{3+}, a blocker of stretch-activated cation (SAC) channels [120]. Recently, TRPV4 has been proved to be present in articular chondrocytes, and chondrocyte response to hypo-osmotic stress is mediated by this channel, which involves both an extracellular Ca^{2+} and intracellular Ca^{2+} release [122].

Actin organization destroyed in chondrocytes exposed to hypo-osmotic stress and subsequently fixed also indicated a progressive disorganization followed by a gradual reorganization. In the absence of extracellular Ca^{2+}, no reorganization of F-actin was observed. The correlation coefficient of actin restructuring and gelsolin was determined and found in all cases to be significant [36]. Latrunculin B effectively disrupted the F-actin cytoskeleton of freshly isolated bovine articular chondrocytes. Passive swelling was not significantly affected by disruption of the F-actin cytoskeleton. However, the cytoskeleton has a restraining role on the RVD resulting from hypo-osmotic challenge, which could be released to some extent by disruption of the cytoskeleton. The signal transduction pathways and the membrane transporters/ion channels involved in the RVD response may be substantially different due to highly unstable cytoskeletal modification [36, 123].

K^+ and Cl^-

When exposed to hyposmotic external solutions (approximately 5% or 32% decrease in osmolarity), isolated rabbit articular chondrocytes exhibited hyposmotic cell swelling, accompanied by the activation of the swelling activated Cl^- current ($I_{Cl,\ swell}$). $I_{Cl,\ swell}$ was practically time-independent at potentials negative to +50 mV but exhibited rapid inactivation at more positive potentials. $I_{Cl,\ swell}$ was potently inhibited by the Cl^- channel blockers 5-nitro-2-(3-phenylpropylamino) benzoic acid, glibenclamide, and tamoxifen, but was little affected by pimozide. $I_{Cl,\ swell}$ was practically time-independent at potentials negative to +50 mV but exhibited rapid inactivation at more positive potentials. $I_{Cl,\ swell}$ was potently inhibited by the Cl^- channel blockers 5-nitro-2-(3-phenylpropylamino) benzoic acid, glibenclamide, and tamoxifen, but was little affected by pimozide [124].

Non-specific volume-sensitive osmolyte channel was found to lead the K^+ flux during RVD in bovine articular chondrocytes [125]. It is insensitive to the ouabain (inhibitor of Na^+-K^+ pump) and bumetanide (inhibitor of NKCC). This kind of channel was also found in variety of cell types with some of the characteristics of an anion channel [126-129]. However specific inhibitors are not found although some Cl^- channel blockers (NPPB [128, 130]), antiestrogens (tamoxifen [130]) and anticalmodulin agents (pimozide [116, 131]) are effective in some cell types. In articular chondrocytes, the channel is also sensitive to pimozide. Surprisingly, tamoxifen, NPPB and DIDS (all inhibitors of volume-active anion channels) were rather poor inhibitors for the channel. It may suggest the different sensitivities of these drugs between cell types which caused be different potential targets either on the channel protein itself or on the regulatory subunit [124]. There was no evidence for volume-sensitive K^+ transporter mediated by the K^+-Cl^- cotransporter. The absence of K^+-Cl^- cotransport under normal conditions is indicated by the lack of effect of Cl^- replacement by NO_3^- on volume-sensitive K^+ flux. The lack of Ca^{2+}-sensitive K^+ flux in Ca^{2+} and ionomycin-treated chondroctes also proved the lack of Ca^{2+} activated K^+ channel [125]. However, there has been a report of the presence of a Ca^{2+}-sensitive K^+ channel in cultured sheep articular chondrocytes [132]. It is also found that K^+ channel activity of chondrocytes can be markedly influenced by culture conditions (fetal calf serum, confluent vs. non confluent cells [133]). K^+/H^+ exchange coupled to the Cl^-/HCO_3^- anion exchanger which was shown in Amphiuma red blood cells [131] also have not be found in articular chondrocytes [134].

2.2.2.2 Mechanism of Regulated Volume Increase (RVI)

Ca^{2+}-Actin-NKCC

In porcine articular chondrocytes, hyper-osmotic shock did not elicit an increase in Ca^{2+} in the presence of Ca^{2+}-free medium. It suggested that Ca^{2+} influx from the extracellular space is essential for Ca^{2+} transients or oscillations to occur [34]. Gadolinium significantly inhibited the Ca^{2+} response under hyper-osmotic conditions, as has been previously reported in other cell types, implicating mechano-sensitive channels as a potential transduction mechanism. It is also found that Ca^{2+} is released from intracellular stores following exposure to hyper-osmotic stress. This mechanism was examined using U73122 (a PLC inhibitor), thapsigargin (an inhibitor of Ca^{2+}-ATPases on endoplasmic reticulum), and low-molecular weight heparin (an inhibitor of IP3 sensitive stores on the endoplasmic reticulum). All three of these inhibitors significantly reduced the number of cells responding under all stimulation conditions [34]. Chondrocytes exposed to PTX showed a significant decrease in the number of cells responding with oscillations of Ca^{2+}. This finding suggests a role for heterotrimeric G-proteins in regulating Ca^{2+} influx to the cytosol. In addition, the activation of G proteins has been shown to lead to activation of the inositol phosphate pathway as well as store-operated Ca^{2+} influx [34].

In avian chondrocytes, following an increase in extracellular osmolality, there was a significant increase in cortical actin inhibited by the removal of extracellular calcium EGTA or by the addition of 100 mmol/L gadolinium chloride [113, 135]. It suggests the role of calcium-mediated polymerization of the actin cytoskeleton during RVI through stretch-activated calcium channels [34, 135] (Figure 2.8). Inhibition of actin polymerisation by removal of extracellular calcium and latrunculin was also found to significantly increase the rate of volume recovery and it was found to be bumetanide (inhibitor of NKCC) sensitive [113, 125, 135]. Thus Na^+-K^+-$2Cl^-$ (NKCC) co-transporter regulated by the actin cytoskeleton is involved in RVI (Figure 2.8). Furthermore, the increase in cortical actin inhibits the activation of the NKCC, potentially by regulating the phosphorylation of the transporter [136].

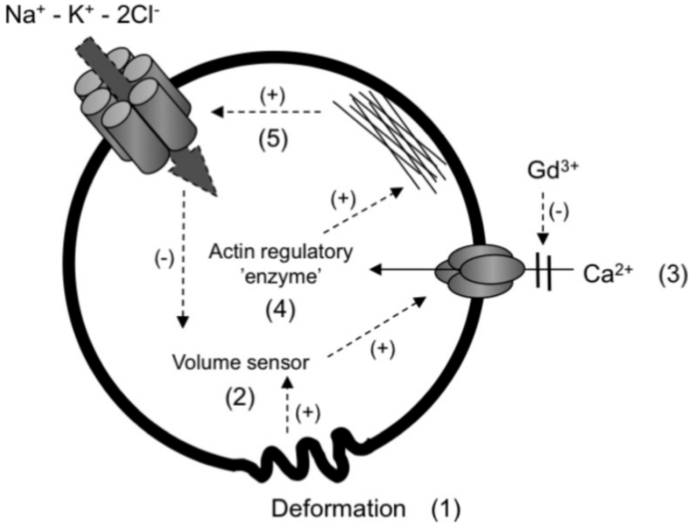

Figure 2.8 Proposed model of avian articular chondrocyte RVI [135].

Na^+-H^+ Exchange

For cells at steady state pH, resuspension in hyper-osmotic solutions elicited an alkalinization, which was significantly inhibited by removal of extracellular Na^+ ions, or treatment with amiloride (1 mM) or HOE-694 (10 mM), both inhibitors of Na^+/H^+ exchange. For cells acidified by ammonium rebound, recovery of pH towards resting levels was significantly stimulated by exposure to hyperosmotic solutions, and the effect was again attenuated by inhibition of Na^+/H^+ exchange. Determination of the rate of acid extrusion at different levels of acidification indicated that the affinity of acid extrusion systems for H^+ ions was increased by hypertonic shock. The response to hyperosmotic media could be abolished by treatment of chondrocytes with the non-specific kinase inhibitor staurosporine (10 nM), while the phosphatase inhibitor okadaic acid (1 mM) was able to augment recovery rates to values similar to those measured under hyperosmotic conditions. It is possible that these effects represent interference with the phosphorylation of serine/threonine residues in the cytoplasmic tail of NHE, the target for cytokine-induced stimulation of NHE [137]. The osmotic sensitivity of recovery was unaffected by exposure to the protein kinase C inhibitor calphostin C, but was abolished in cells treated with ML-7, a specific inhibitor of myosin light chain kinase. It means that increased osmolarity can modulate the activity of Na^+/H^+ exchange, in this case by altered patterns of phosphorylation of transporter-associated myosin [137].

2.2.3 IVD Cell Volume Regulation

2.2.3.1 Cell Volume Response and its Mechanism under Hypotonic Condition

Both passive and RVD were observed in porcine AF cells under hypo-osmotic stress [38] (Figure 2.9). The time constant for cell swelling in response to hypo-osmotic stress was small compared with volume recovery and was unaffected by either the magnitude of applied stress or the disruption of F-actin. These results suggest that cell swelling is a passive process which is mediated primarily by the permeability of the cell membrane to water and is independent of changes in F-actin structure [38].

In response to hypo-osmotic stress, AF cells swelled and disrupted F-actin, and exhibited Ca^{2+} transients in proportion to the magnitude of the stress. The transient disruption of F-actin was dependent on the presence of extracellular Ca^{2+} [38]. This finding is consistent with the findings of previous studies on articular chondrocytes [36, 123].

After swelling, AF cells underwent RVD at all magnitudes of hypo-osmotic stress. F-actin recovery towards baseline levels was also observed which is similar to articular chondrocytes [36, 123]. The extent of RVD was significantly diminished by F-actin breakdown using cytochalasin D or by the inhibition of swelling-induced F-actin disruption by removing extracellular Ca^{2+} [38]. This finding is consistent with the fact that a number of well characterized F-actin binding and severing proteins, such as gelsolin are Ca^{2+} dependent and have been implicated in the cellular response to hypo-osmotic stress [36]. Swelling-induced disruption of F-actin facilitated RVD, which was evidenced by a more rapid volume recovery with increased F-actin breakdown by increasing hypo-osmotic stress. The inhibition of F-actin breakdown in the absence of extracellular Ca^{2+} may act to diminish regulatory volume decrease (RVD) by maintaining a cortical barrier to the trans-membrane transport of small molecules and ions which are important for volume regulation [138]. Inhibition of RVD in the presence of cytochalasin D however, suggests a distinct mechanism whereby RVD may be attenuated by the inability of the disrupted F-actin to undergo dynamic polymerization/depolymerization. The interplay between these two distinct mechanisms is currently unclear and warrants further study.

Phalloidin treatment had no effect on the observed hypo-osmotically induced Ca^{2+} transients which suggests that AF cells respond to hypo- and hyper-osmotic stress by distinct mechanisms. One explanation for this difference is that even a highly stabilized F-actin network is unlikely to possess adequate stiffness to withstand the stresses generated during cell swelling [139, 140]. As a result, the proposed barrier function of cortical F-actin is not likely involved in the response to hypo-osmotic stress. The behavior of calcium signaling in AF cells is consistent with that seen in a number of other cell types which show differential responses to hypo- and hyper-osmotic stress [34, 36].

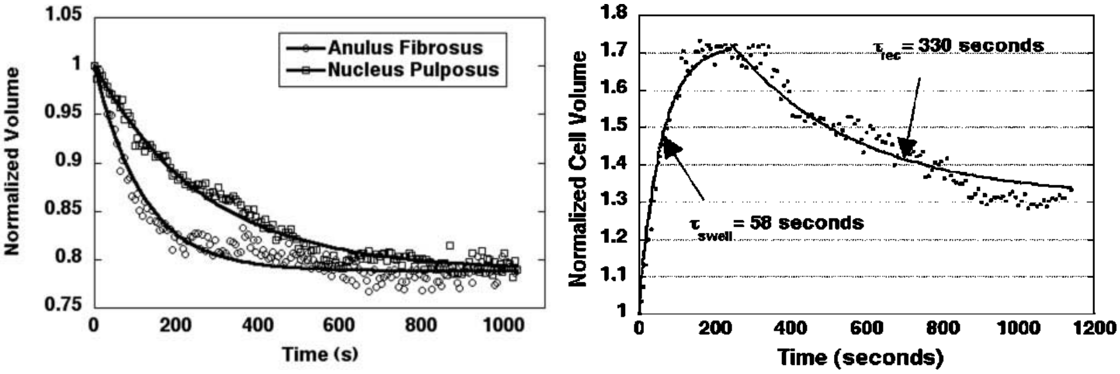

(a) (b)

Figure 2.9 Volume response of porcine IVD cells under osmotic pressure. a: Porcine AF cells after the application of hypo-osmotic stress [38]. b: Porcine IVD cells after the application of hyper-osmotic stress [35].

2.2.3.2 Cell Volume Response and its Mechanism under Hypertonic Condition

Cells from each of the three tissue zones decreased in volume significantly after exposure to hyperosmotic stress, but exhibited no significant regulatory volume increase over the time of testing either in the presence or absence of calcium transients [35]

(Figure 2.9). This response differs from the response observed in articular chondrocytes, in which the cells actively regulate their volume in a Ca^{2+} dependent manner and appear to decrease in volume at a faster rate [34, 113, 135]. The differences between IVD cells and articular chondrocytes are possibly due to intrinsic differences in cell properties or differences in their in vivo environment.

Porcine IVD cells respond to hyperosmotic stress by increasing the concentration of intracellular calcium through a mechanism involving F-actin. In response to hyperosmotic stress, control cells from all zones decreased in volume and cells from the AF and TZ exhibited calcium transients, while cells from the NP did not [35]. This response is in part dependent on the integrity and organization of the cytoskeleton, which differs significantly between cells of the NP and those of the AF or TZ [141]. Extracellular Ca^{2+} was necessary to initiate intracellular calcium transients. Stabilization of F-actin with phalloidin prevented the Ca^{2+} response in AF and TZ cells and decreased the rate of volume change in cells from all zones, coupled with an increase in the elastic moduli and apparent viscosity. Conversely, actin breakdown with cytochalasin D facilitated Ca^{2+} signaling while decreasing the elastic moduli and apparent viscosity of the NP cells. With cytochalasin D treatment, NP cells exhibited significantly greater decreases in volume than AF or TZ cells. Time constant for volume adaptation for NP cells was significantly higher than those of AF and TZ cells and was decreased by cytochalasin D treatment [35]. This response is in part dependent on the integrity and organization of the cytoskeleton, which differs significantly between cells of the NP and those of the AF or TZ [141].

In summary, the cell volume response and its regulation mechanisms are significantly different between articular chondrocytes and IVD cells as shown in Table 2.2.

Table 2.2 Volume regulation mechanisms in articular chondrocytes and IVD cells.

		Possible Mechanism	**Articular Chondrocytes**	**IVD cells**
Passive		☑	☑	☑
RVD	**Taurine**	☑	☑	▪
	Ca2+	☑	☑	☑
	Actin	☑	☑	☑
	K+	☑	☑	▪
	Cl-	☑	☑	▪
	KCC	☑	☒	▪
RVI	**Taurine**	☑	☒	☒
	Ca2+	☑	☑	☒
	Actin	☑	☑	☒
	NKCC	☑	☑	☒
	NHE	☑	☑	☒

2.2.4 Single Cell Modeling

Since it is difficult to observe the cell behaviors in vivo and in real time, finite element models are a useful method to simulate the cell-PCM-ECM mechanical environment, trans-membrane water or solute (ions or nutrient) transport and cell volume response. The complex nature of the cell was simplified using a series of mathematical models that attempt to predict cellular responses. The IVD cells and articular chondrocytes have been previously modeled with the elastic, biphasic theory and recently the triphasic/multiphasic theory. Validation of numerical simulation can be achieved by combining experimental testing with computational results to determine the accuracy of predictions. Characterization of the biomechanical and transport characteristics of the cell must be well researched before a single cell model can be created to ensure that it will accurately predict cellular behavior under changing conditions.

Accurate single cell models that are proven with validation help researchers characterize the differences between normal and abnormal IVD cell behaviors. Models could also track the behavior of the cells over time, allowing better understand of IVD cell behaviors as a result of various loading and environmental changes. These predictions may help researchers to understand IVD cell etiology related with human IVD degeneration and further develop possible therapeutic and regenerative treatments.

2.2.4.1 Biomechanical Response Simulation

IVD Cells

In order to simulate the biomechanical response of IVD cells, several types of single cell models include one phase, biphasic and triphasic theory were used in previous years. The IVD cell was considered as a single phase material such as a linear elastic and transversely isotropic solid. The model predictions for strain, dilatation, and apparent membrane stretch reflect cell-matrix interactions that are expected to occur at equilibrium. Both material properties of the extracellular matrix and geometric parameters of the cell are found to be important factors in determining the cellular and pericellular strain fields [142]. In contrast, changes in cellular morphology and orientation in response to mechanical stimuli have also been observed by experimental methods in a variety of other cell types [143-146].

Using the biphasic theory, the flow-dependent viscoelasticity of IVD cells could be described. A hyper-elastic constitutive law was used for the solid phase and the material anisotropy was considered by including a fiber-reinforced continuum law in the hyperelastic strain energy function for AF tissue [82]. Moreover, in situ geometry of IVD cells was measured experimentally using laser scanning confocal microscopy and three-dimensional reconstruction techniques [82, 147, 148] (Figure 2.10). Larger cellular strains were predicted in the anisotropic annulus fibrosus and transition zone compared to the isotropic nucleus pulposus under uni-axial tensile strain along the local collagen fiber direction. AF cells were predicted to experience approximately 3 times higher volumetric strain at equilibrium, as compared to the PCM domains [147]. NP cells and PCM regions were predicted to experience volumetric strains that were 1.9–3.7 and 1.4–2.1 times greater than the extracellular matrix, respectively [148]. The strain concentrations were generally found at the cell/PCM interface and stress concentration at the PCM/ECM interface [147, 148]. Furthermore, geometry of IVD cells in situ was also predicted to be an adaptation to reduce cellular strains during tissue loading[82]. Increased numbers of cells within a contiguous PCM was associated with an apparent increase of strain levels and decreased rate of fluid pressurization in the cell, with magnitudes dependent on the cell size, shape and relative position inside the PCM [147, 148].

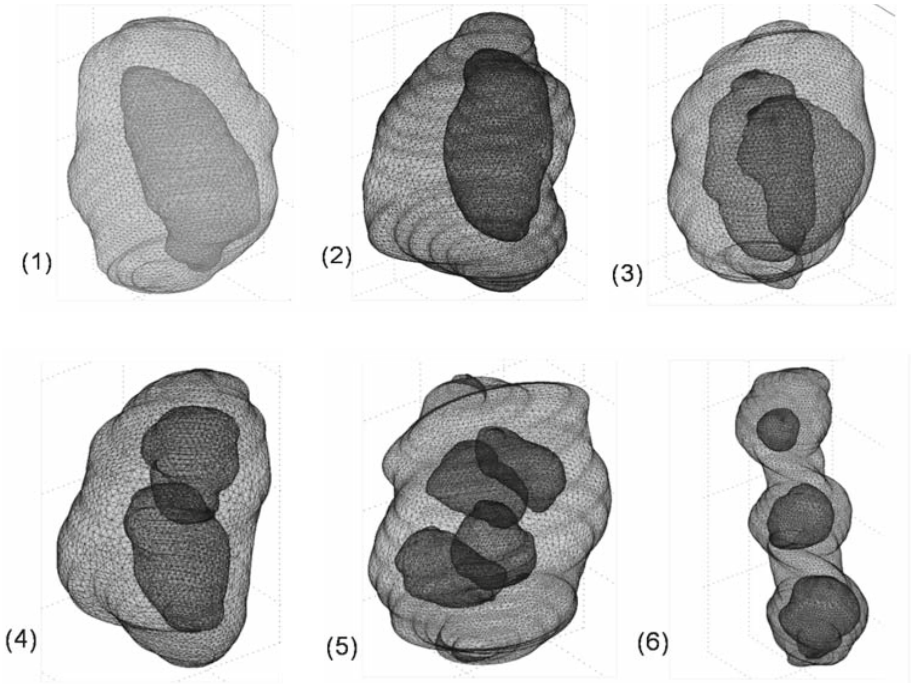

Figure 2.10 3D solid geometries in tetrahedron meshes in the nucleus pulposus. Models include different cell–matrix unit (CMU) subgroups [148]. (1) and (2): 1 cell CMUs. (3) and (4): 2 cell CMUs. (5) and (6): 3 or 4 cell CMUs.

Articular Chondrocytes

Biphasic theory was also used to simulate the biomechanical response of articular chondrocytes under static and cyclic compressive loading conditions [149, 150]. The microscale cartilage environment was represented as a three-zone biphasic region consisting of a spherical chondrocyte with encapsulating pericellular matrix (PCM) that was embedded in a cylindrical extracellular matrix (ECM). Strain/stress concentrations was found at the cell matrix border under both static and cyclic loading conditions. A nearly two-fold increase in strain and dilatation (volume change) at the cellular level was found under static compression, as compared to the macroscopic level [149]. This result is similarly observed in IVD cells [82, 147, 148]. The pericellular matrix was found to have a functional biomechanical role and work as a protective layer for articular chondrocytes [149]. Axial strain was significantly amplified in the range of 0.01-1.0Hz, with a decrease in amplification factor and frequency insensitivity at the higher frequencies. Matrix degradation due to osteoarthritis could significantly alter strain amplification factors when the loss of matrix stiffness was exclusive to the PCM [149, 150].

Recently, effect of the cell membrane on water transport in chondrocytes was considered by defining the cell as hydrogel like cytoplasm plus fluid filled membrane using mixture theory [151]. Under mechanical loading of isolated chondrocytes, the intracellular fluid pressure is on the order of tens of Pascals and the trans-membrane fluid outflow is on the order of picometers per second. This response takes several days to subside and consequently, the chondrocytes practically behaves as an incompressible solid whenever the loading duration is on the order of minutes or hours. When embedded in its extracellular matrix, the chondrocytes response is substantially different. Mechanical loading of the tissue leads to a fluid pressure difference between intracellular and extracellular compartments on the order of tens of kilopascals and the trans-membrane outflow is on the order of a nanometer per second. This response subsides in approximately one hour. The interstitial fluid flow in the extracellular matrix is directed around the cell, with peak values on the order of tens of nanometers per second [151]. The viscous fluid shear stress acting on the cell surface is orders of magnitude smaller than the solid matrix shear stresses resulting from the extracellular matrix deformation [152].

However, more accurate boundary conditions, such as displacement and fluid pressure in the near cell region, and physical assumptions representing loading and material properties appropriate to non-degenerate or pathological disk tissues could be implemented. Another potential limitation of the current model includes the assumption of linearity and elasticity for the solid phase of the NP as a biphasic material, although intrinsic viscoelasticity and nonlinear effects have been well documented for the NP extracellular matrix [153, 154]. Chemical and electrical effects were also expected to be considered in order to construct more realistic predictions of cell-level stimuli to analyze cell mechanobiology.

2.2.4.2 Cell Volume Regulation Simulation

Previously, Boyle-van't Hoff and Kedem & Katchalsky equations [39] were used to simulate the passive cell volume response under hypotonic and hypertonic condition. However, mechanical effects such as the cell membrane tension force or physicochemical factors such as the solute partition effect could not be considered. A more general approach mixture theory approach [40] was developed to incorporate these factors. Fundamental governing relationships for mechano-electrochemical transduction effects such as streaming potential, streaming current, diffusion (membrane) potential, and electro-osmosis could be deduced using this mixture theory. Specifically, stress, strain, and fluid velocity fields through a membrane during a one-dimensional steady diffusion process was simulated using this theory. Exchange of Na^+ and Ca^{2+} through the membrane were also analyzed [14]. Recently, several types of cell models were used to simulate cell volume response of articular chondrocytes and IVD cells by defining the cell as fluid-filled membrane or hydrogel/perfect osmometer like cytoplasm plus fluid filled membrane using the mixture theory [41, 42]. The cytoplasm and cell membrane were defined as a multiphasic mixture of solid phase (cytoskeleton), fluid phase (interstitial fluid), and sometimes a solute phase (ions).

Passive volumetric response of an isolated chondron under osmotic loading in a simple salt solution at equilibrium was simulated by defining the chondrocytes as an ideal osmometer with triphasic PCM [42] (Figure 2.11). The chondron boundary is assumed to be permeable to both water and ions, while the chondrocyte membrane is selectively permeable to only water. For the case of a neo-Hookean PCM constitutive law, the model is used to conduct a parametric analysis of the cell and chondron deformation under hyper- and hypo-osmotic loading. In combination with osmotic loading experiments on isolated chondrons, model predictions will aid in determination of pericellular fixed charge density and its relative contribution to PCM mechanical properties [42].

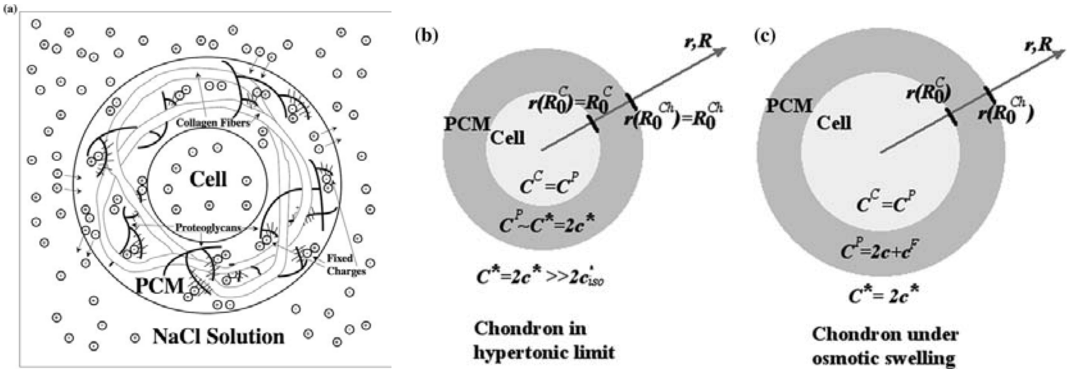

Figure 2.11 Mechano-chemical model of an isolated chondron at equilibrium in NaCl solution [42].

Passive response of cells to osmotic loading with neutrally charged solutes was also simulated by defining chondrocytes as fluid filled membrane. The volume response to osmotic loading is found to be very sensitive to the magnitude of cell membrane tension and the partition coefficient of the solute in the cytoplasm, which controls the magnitude of cell volume recovery [41]. The theoretical predictions of this model are comparable with experimental results available in the literature [110, 155, 156]. This cell model could aid in determination of cell water content, hydraulic permeability, solute permeability and partition coefficient by well experiment design [37].

Recently, governing equations for active transport across semi-permeable membranes were formulated within the framework of the theory of mixtures. In the mixture theory, which models the interactions of any number of fluid and solid constituents, a supply term appears in the conservation of linear momentum to describe momentum exchanges among the constituents. In past applications, this momentum supply was used to model frictional interactions only, thereby describing passive transport processes. However active transport processes, which impart momentum to solutes or solvent, may also be incorporated in this term. By projecting the equation of conservation of linear momentum along the normal to the membrane, a jump condition is formulated for the mechano-electrochemical potential of fluid constituents which is generally applicable to non-equilibrium processes involving active transport [157]. However, until now there is no constitutive relation from the experiment describing trans-membrane active transport.

CHAPTER 3 A SPECIALIZED MULTIPHASIC MODEL FOR IVD TISSUE

3.1 Introduction

Many studies concerning the fundamentals of the theory and development of mathematical models in the field of soft tissue biomechanics have been published [13, 14, 158-160]. Mixture theory was the most frequently used theory which considers the tissue as a mixture of continuum material. The interaction between each phase of the mixture determines the macroscopic behavior of the tissue. At first, the mixture theory is developed for deforming porous media [161] [162]. Later, the modem mixture theory was derived and applied in soft tissue. One of them is the well-known, biphasic theory for cartilage developed by Mow and co-workers [160], which considers tissue as a mixture of water and solid phases. By using this theory, biomechanical and fluid transport behaviors in hydrated soft tissue such as articular cartilage and hydrogels have been successfully investigated. Lai and co-workers also further developed a triphasic mechano-electrochemical theory by incorporating a third component (the ion phase). Therefore it could be used to describe the osmotic swelling behavior which is due to the negative charge of hydrated soft tissue [40]. Based on the triphasic theory, there are three phases in the soft tissue. The collagen-proteoglycan matrix was considered as the solid phase which was treated as the negatively charged due to the charged proteoglycan in the matrix. The interstitial water was considered as fluid phase while cation and anion were considered as ion phase.

Tertiary-mixture theory and thermodynamics laws were used to derive the formulation of the biphasic and triphasic theory [163] [164]. They were widely used for the analysis of tissue swelling, negative osmosis/pressure, electrokinetic phenomena, and fluid and ion transport in charged soft tissue [165-176]. Moreover, Gu et al. successfully extended the triphasic theory to describe the swelling and passive transport of multi-electrolytes with polyvalence through charged hydrated soft tissues and cell membranes [177]. Recently, Yao et al. successfully develop the specialized finite element formulation of the triphasic theory to analyze of mechano-electrochemical signals inside the cartilage and IVD tissue under various loading conditions [21-23]. Note that the mechano-electrochemical signals in bones have also been analyzed [178-180]. Microcontinuum models were also developed for charged hydrated soft tissues [181-183]. A similar multiphasic theory was also developed by Huyghe and Janssen for porous media.[184, 185]

The IVD is the largest avascular structure in the human body. Nutrients supplied by blood vessels at the margins of the disc plays a key role in maintaining IVD tissue health. The most basic nutrients consist of glucose, oxygen and lactate. It is difficult to measure the in vivo nutrient distribution inside the disc under physiological conditions. Therefore, numerical simulation is essential to determine the nutrient level as well as physical signals within the human IVD. In this study, a multiphasic theoretical model based on triphasic theory was developed by taking nutrient solutes into consideration. The nutrient solute transport inside human IVD under mechanical loading condition therefore could be simulated. Furthermore, by adding a supply term in mass conservation equation, this model is capable of taking the effect of cellular energy metabolism of IVD cells into consideration. In this chapter, the specialized multiphasic model and its weak form were presented.

3.2 A Multiphasic Theory for Physical Signals and Nutrient Solute Transport in IVD Tissue

In this section, the theory described is a specific form of the general multiphasic theory while all the deformation is assumed to be infinitesimal [40, 177]. The multiphase in the charged tissue consists of incompressible solid phase with fixed charges, interstitial water phase, ion phase with two monovalent species (e.g., Na^+ and Cl^-), and uncharged nutrient solute phases (o = glucose, lactate and oxygen).

3.2.1 Conservation of Mass

For solid, fluid and ion phases, conservation of mass could be described as follows under no chemical reaction assumption,

$$\partial \rho^{\alpha} \big/ \partial t + \nabla \cdot (\rho^{\alpha} \mathbf{v}^{\alpha}) = 0 \qquad (\alpha = s, w, +, -), \tag{3.1}$$

For nutrient solutes phase, conservation of mass could be described as follows by taking cellular energy metabolism into consideration (IVD cells consumed glucose and oxygen while producing lactate during glycolysis or oxidation),

$$\partial \rho^{n} \big/ \partial t + \nabla \cdot (\rho^{n} \mathbf{v}^{\mathbf{n}}) = Q^{n} \qquad (n = \text{glucose, lactate and oxygen}), \tag{3.2}$$

where ρ^{α} and ρ^{n} are the apparent mass density of each component. $\mathbf{v}^{\alpha}$ and $\mathbf{v}^{\mathbf{n}}$ represent the velocity. Q^{n} are the cellular metabolism rates (consumption/production rates) of nutrient solutes.

By neglecting the volume fractions of ions and nutrient solutes based on the apparent mass density condition, the continuity equation of the mixture is

$$\nabla \cdot \left(\phi^{s}\mathbf{v}^{s} + \phi^{w}\mathbf{v}^{w}\right) = 0\,. \tag{3.3}$$

Based on infinitesimal deformation assumption, the water volume fraction is related to the deformation by [40, 177]

$$\phi^{w} = \frac{\phi_{0}^{w} + e}{1 + e}, \tag{3.4}$$

where *e* is the dilatation of the solid matrix. It is related to the infinitesimal strain tensor **E** by *e*=tr(**E**); ϕ_{0}^{w} is the water volume fraction at the reference configuration (i.e., at *e*=0).

Assuming that the total quantity of fixed charged groups attached to the solid matrix are not changing with the extracellular ion concentration or matrix deformation, conservation of the fixed charge reads

$$\partial\left(\phi^{w}c^{F}\right)/\partial t + \nabla \cdot \left(\phi^{w}c^{F}\mathbf{v}^{s}\right) = 0\,. \tag{3.5}$$

For infinitesimal deformation, the fixed charge density can be expressed with the tissue deformation as

$$c^F = c_0^F \big/ (1 + e/\phi_0^w)\,, \tag{3.6}$$

where c_0^F is the FCD at the reference configuration (e=0).

Substituting equations (3.4) into (3.6), conservation of the fixed charge can also be expressed as

$$c^F = \frac{c_0^F (1-\phi^w)\phi_0^w}{(1-\phi_0^w)\phi^w}\,. \tag{3.7}$$

3.2.2 Conservation of Linear Momentum

In this multiphasic theory, by neglecting gravitational and magnetic forces, the gradient of the chemical/electrochemical potentials are driving forces, while it is balanced by the frictional force caused by the interaction of each phase. Therefore, momentum equations for the mixture (tissue) and each component can be expressed as equations (3.8-3.12).

Tissue:

$$\nabla \cdot \boldsymbol{\sigma} = 0\,, \tag{3.8}$$

Water:

$$-\rho^{\mathbf{w}} \nabla \mu^{\mathbf{w}} + f_{ws}\left(\mathbf{v}^{\mathbf{s}} - \mathbf{v}^{\mathbf{w}}\right) + f_{w+}\left(\mathbf{v}^{+} - \mathbf{v}^{\mathbf{w}}\right) + f_{w-}\left(\mathbf{v}^{-} - \mathbf{v}^{\mathbf{w}}\right) + f_{wn}\left(\mathbf{v}^{\mathbf{n}} - \mathbf{v}^{\mathbf{w}}\right) = 0\,, \tag{3.9}$$

Cation:

$$-\rho^{+}\nabla\tilde{\mu}^{+} + f_{+s}\left(\mathbf{v}^{\mathbf{s}} - \mathbf{v}^{+}\right) + f_{+w}\left(\mathbf{v}^{\mathbf{w}} - \mathbf{v}^{+}\right) + f_{+-}\left(\mathbf{v}^{-} - \mathbf{v}^{+}\right) + f_{+n}\left(\mathbf{v}^{\mathbf{n}} - \mathbf{v}^{+}\right) = 0\,, \tag{3.10}$$

Anion:

$$-\rho^{-}\nabla\tilde{\mu}^{-} + f_{-s}\left(\mathbf{v}^{\mathbf{s}} - \mathbf{v}^{-}\right) + f_{-w}\left(\mathbf{v}^{\mathbf{w}} - \mathbf{v}^{-}\right) + f_{-+}\left(\mathbf{v}^{+} - \mathbf{v}^{-}\right) + f_{-n}\left(\mathbf{v}^{\mathbf{n}} - \mathbf{v}^{-}\right) = 0\,, \tag{3.11}$$

Nutrient Solutes:

$$-\rho^{n}\,\nabla\,\mu^{n} + f_{ns}\left(\mathbf{v}^{\mathbf{s}} - \mathbf{v}^{\mathbf{n}}\right) + f_{nw}\left(\mathbf{v}^{\mathbf{w}} - \mathbf{v}^{\mathbf{n}}\right) + f_{n+}\left(\mathbf{v}^{+} - \mathbf{v}^{\mathbf{n}}\right) + f_{n-}\left(\mathbf{v}^{-} - \mathbf{v}^{\mathbf{n}}\right) = 0\,, \tag{3.12}$$

where $\boldsymbol{\sigma}$ is the total stress of the mixture (tissue); μ^{w} and μ^{n} are the chemical potentials of water and nutrient solutes per unit mass, respectively; $\tilde{\mu}^{+}$ and $\tilde{\mu}^{-}$ are the electrochemical potentials of cation and anion per unit mass, respectively. $f_{\alpha\beta}$ is the friction coefficient per unit tissue volume between the inter-diffusing α and β components. Here the friction coefficients in each unit of the tissue are assumed to be symmetric, i.e. $f_{\alpha\beta} = f_{\beta\alpha}$.

3.2.3 Constitutive Relationship

The total stress of the mixture with infinitesimal deformation could be expressed by equation (3.13). The constitutive relations for the chemical potential of water, the electrochemical potentials of monovalent ions and the chemical potential of nutrient solutes could be expressed as equations (3.14-3.17).

$$\boldsymbol{\sigma} = -p\mathbf{I} - T_c\mathbf{I} + \sigma^{\mathbf{e}} = -p\mathbf{I} - T_c\mathbf{I} + \lambda \mathrm{tr}(\mathbf{E}) + 2\mu\mathbf{E}, \tag{3.13}$$

$$\mu^{\mathbf{w}} = \mu_0^{\mathbf{w}} + \left[p - RT\varphi T\phi^{+} + c^{-} + c^{\mathbf{n}}\ ) + B_w\ \mathrm{tr}(\mathbf{E})\right] / \rho_{\mathbf{T}}^{\mathbf{w}}\ , \tag{3.14}$$

$$\tilde{\mu}^{+} = \mu_0^{+} + \left(RT/M_{+}\right)\ln\left(\gamma_{+}c^{+}\right) + F_c\psi/M_{+}\ , \tag{3.15}$$

$$\tilde{\mu}^{-} = \mu_0^{-} + \left(RT/M_{-}\right)\ln\left(\gamma_{-}c^{-}\right) - F_c\psi/M_{-}\ , \tag{3.16}$$

$$\mu^{n} = \mu_0^{n} + \left(RT/M_n\right)ln\left(\gamma_n c^{n}\right), \tag{3.17}$$

where p is the fluid pressure; T_c is the chemical expansion stress; $\sigma^{\mathbf{e}}$ is the elastic part of the stress in solid matrix; $\mathbf{E}$ is the strain tensor measured from the reference state; λ and μ are the elastic constants of the solid matrix; μ_0^{α} (α = w,+,–,n) is the reference chemical potential for α component; γ_{+}, γ_{-} and γ_n are the activity coefficients of cation, anion and nutrient solutes, respectively; ψ is the electrical potential; ϕ is the osmotic coefficient; B_w is the interphase coupling coefficient; R is the universal gas constant; T is the absolute temperature.

3.2.4 Fluxes

The fluxes of water, cation, anion and nutrient solutes relative to the solid phase can be expressed with the combination of the gradients of the (electro)chemical potentials, equations (3.18-3.21).

$$
\begin{aligned}
\mathbf{J}^{\mathbf{w}} &= \phi^{\mathbf{w}}\left(\mathbf{v}^{\mathbf{w}} - \mathbf{v}^{\mathbf{s}}\right) \\
&= -\phi^{w}\left(\mathrm{B}_{11}\rho^{w}\nabla\mu^{w} + \mathrm{B}_{12}\rho^{+}\nabla\tilde{\mu}^{+} + \mathrm{B}_{13}\rho^{-}\nabla\tilde{\mu}^{-} + \mathrm{B}_{14}\rho^{n}\nabla\mu^{n}\right) \ ,
\end{aligned}
\tag{3.18}
$$

$$
\begin{aligned}
\mathbf{J}^{+} &= c^{+}\,\phi^{w}\left(\mathbf{v}^{+} - \mathbf{v}^{\mathbf{s}}\right) \\
&= \mathrm{B}_{21}\,c^{+}\,\mathbf{J}^{\mathbf{w}} - c^{+}\,\phi^{w}(\mathrm{B}_{22}\rho^{+}\nabla\tilde{\mu}^{+} + \mathrm{B}_{23}\rho^{-}\nabla\tilde{\mu}^{-} + \mathrm{B}_{24}\rho^{n}\nabla\mu^{n}\ ) \ ,
\end{aligned}
\tag{3.19}
$$

$$
\begin{aligned}
\mathbf{J}^{-} &= c^{-}\,\phi^{w}\left(\mathbf{v}^{-} - \mathbf{v}^{\mathbf{s}}\right) \\
&= \mathrm{B}_{31}\,c^{-}\,\mathbf{J}^{\mathbf{w}} - c^{-}\,\phi^{w}(\mathrm{B}_{32}\rho^{+}\nabla\tilde{\mu}^{+} + \mathrm{B}_{33}\rho^{-}\nabla\tilde{\mu}^{-} + \mathrm{B}_{34}\rho^{n}\nabla\mu^{n}\ ) \ ,
\end{aligned}
\tag{3.20}
$$

$$
\begin{aligned}
\mathbf{J}^{\mathbf{n}} &= c^{n}\,\phi^{w}\left(\mathbf{v}^{\mathbf{n}} - \mathbf{v}^{\mathbf{s}}\right) \\
&= \mathrm{B}_{41}\,c^{n}\,\mathbf{J}^{\mathbf{w}} - c^{n}\,\phi^{w}(\mathrm{B}_{42}\rho^{+}\nabla\tilde{\mu}^{+} + \mathrm{B}_{43}\rho^{-}\nabla\tilde{\mu}^{-} + \mathrm{B}_{44}\rho^{n}\nabla\mu^{n}\ ) \ ,
\end{aligned}
\tag{3.21}
$$

where B_{ij}'s are the material coefficients that are functions of the frictional coefficients $f_{\alpha\beta}$ between α and β constituents.

Substituting constitutive equations (3.14-3.17) into momentum equations (3.9-3.12), relative fluxes of water, cation, anion and uncharged solute were expressed as equations (3.22-3.25), which are the well-known phenomenological relations in non-equilibrium thermodynamics [164]. For example, based on Nernst-Planck equation (ion flux through a hydrated tissue including convection) [186, 187], we augmented the ion flux equations (3.23-3.24). Note the activity coefficients (γ_{+}, γ_{-} and γ_{n}) are assumed as constant.

$$
\begin{aligned}
\mathbf{J}^{w} = &-k\nabla p - kB_{w}\nabla tr(\mathbf{E}) \\
&- RTk\left[(e^{+}-\phi)\nabla c^{+} + (e^{-}-\phi)\nabla c^{-} + (e^{o}-\phi)\nabla c^{0}\right] \\
&- F_{c}k(e^{+}c^{+} - e^{-}c^{-})\nabla\psi \ ,
\end{aligned}
\tag{3.22}
$$

$$\mathbf{J}^{+} = H^{+}c^{+}\mathbf{J}^{w} - \phi^{w}D^{+}\nabla c^{+} - F_{c}\phi^{w}\omega^{+}c^{+}\nabla\psi, \qquad (3.23)$$

$$\mathbf{J}^{-} = H^{-}c^{-}\mathbf{J}^{w} - \phi^{w}D^{-}\nabla c^{-} + F_{c}\phi^{w}\omega^{-}c^{-}\nabla\psi, \qquad (3.24)$$

$$\mathbf{J}^{\mathbf{n}} = H^{n}c^{n}\,\mathbf{J}^{\mathrm{w}} - \phi^{\mathrm{w}}\,D^{n}\,\nabla c^{n}, \qquad (3.25)$$

where k, e^{α}, H^{α}, D^{α}, and ω^{β} (α = +, –, n; β = +, –), represent, respectively, the hydraulic permeability of the water, the transport factor of the solute, the hindrance factor of the solute for the convection, the intra-tissue diffusivity of the solute, and the intra-tissue mobility of the solute [186, 188]. The relations of these phenomenological transport parameters to the frictional coefficients are shown in Appendix D.

In Equations (3.22-3.25), the relationship between diffusivity D^{α} and the mobility ω^{α} can be expressed by $D^{\alpha} = RT\omega^{\alpha}$ which is known as the Nernst-Einstein or the Einstein-Planck equation [187]. In equation (3.22), the forth term on the right side is the electro-osmosis induced water flux. Even when the numbers of cation and anion are identical, the electro-osmotic motion of water can still appear when e^{+} and e^{-} are not identical. Same findings were noted in the double-layer theory of the electro-osmosis.[189]

3.2.5 Boundary Conditions

Based on the continuity of solid displacement, total stress, the fluxes and (electro)chemical potential of each phases (water, ion and nutrient solutes) at the boundaries, the boundary conditions in this specialized multiphasic model are represented by equations (3.26-3.27). Due to the continuity of the (electro)chemical potentials, discontinuous ion concentrations or fluid pressure could be predicted in the interface between tissue and external bath solution.

$$\mathbf{u} = \mathbf{u}^*, \; \mu^w = \mu^{w*}, \quad \tilde{\mu}^+ = \tilde{\mu}^{+*}, \quad \tilde{\mu}^- = \tilde{\mu}^{-*}, \quad \mu^n = \mu^{n*}, \tag{3.26}$$

$$\boldsymbol{\sigma} \cdot \mathbf{n} = \mathbf{t}_{app}, \; \mathbf{J}^\alpha \cdot \mathbf{n} = \mathbf{J}^{\alpha*} \cdot \mathbf{n} \quad (\alpha = \mathrm{w}, +, -, \mathrm{n}), \tag{3.27}$$

where * indicates prescribe values (the quantities in the bathing solution); $\mathbf{t}_{\mathrm{app}}$ is the traction**;** **n** represents the outward unit normal to the boundary.

3.3 Dimensional Analysis of the Multiphasic Theory

In this section, a dimensionless equivalent formulation and weak form of the multiphasic theory were presented for finite element analysis of physic signals and nutrient solute transport in human IVD.

3.3.1 An Equivalent Electrochemical Potential Function

Due to the nonlinear jump conditions between elements and across the boundary of the interfaces [40, 184, 185], a simple transformation of the electrochemical potential function for water, ion and nutrient solute phases were done as shown in equations (3.28-3.31). The modified (electro)chemical potentials have the same dimension as ion concentration, to therefore avoid the potential mathematical complexity of logarithm in numerical implementation.

$$\varepsilon^{w} = \frac{\rho_T^{w}\left(\mu^{w} - \mu_0^{w}\right)}{RT}, \tag{3.28}$$

$$\varepsilon^{+} = \exp\left[\frac{M_{+}\left(\tilde{\mu}^{+} - \tilde{\mu}_0^{+}\right)}{RT}\right], \tag{3.29}$$

$$\varepsilon^{-} = \exp\left[\frac{M_{-}\left(\tilde{\mu}^{-} - \tilde{\mu}_0^{-}\right)}{RT}\right], \tag{3.30}$$

$$\varepsilon^{n} = exp\left[\frac{M_{n}\left(\mu^{n} - \mu_0^{n}\right)}{RT}\right]. \tag{3.31}$$

In these formulations, the solid displacement **u** and the modified (electro)chemical potentials ε^{α} (α = w,+,–,n) are opted for the primary degrees of freedom.

3.3.2 Governing Equations

In order to derive the dimensionless variables, governing equations and boundary/Initial conditions, three variables (length L, concentration C_0 and diffusivity D_0^n were chosen as the basic variables. The non-dimensional quantities are defined by

$$\bar{x} = \frac{x}{h},\ \bar{y} = \frac{y}{h},\ \bar{z} = \frac{z}{h},\ \bar{\mathbf{u}} = \frac{\mathbf{u}}{h},\ \bar{t} = \frac{t}{\tau},\ \tau = \frac{h^2}{H_A k_0},\ \bar{c}^{+} = \frac{c^{+}}{c_0},\ \bar{c}^{-} = \frac{c^{-}}{c_0},\ \bar{c}^{n} = \frac{c^{n}}{c_0^{n}}$$

$$\bar{\varepsilon}^{+} = \frac{\varepsilon^{+}}{c_0},\ \bar{\varepsilon}^{-} = \frac{\varepsilon^{-}}{c_0},\ \bar{\varepsilon}^{n} = \frac{\varepsilon^{n}}{c_0^{n}}$$

$$\bar{\boldsymbol{\sigma}} = \frac{\boldsymbol{\sigma}}{RT\,c_0},\ \bar{D}^+ = \frac{D^+}{D_0^+},\ \bar{D}^- = \frac{D^-}{D_0^-},\ \bar{D}^n = \frac{D^n}{D_0^n},\ \bar{\mathbf{J}}^{\mathbf{w}} = \frac{\mathbf{J}^{\mathbf{w}}\cdot h}{H_A k_0},\ \bar{\mathbf{J}}^+ = \frac{\mathbf{J}^+\cdot h}{H_A k_0 c_0}$$

$$\bar{\mathbf{J}}^- = \frac{\mathbf{J}^-\cdot h}{H_A k_0 c_0},\ \bar{\mathbf{J}}^{\mathbf{n}} = \frac{\mathbf{J}^{\mathbf{n}}\cdot h}{H_A k_0 c_0^n},\ \bar{Q}^n = \frac{Q^n}{c_0^n/\tau} = \frac{Q^n\cdot h^2}{H_A k_0 c_0^n}$$

where h is the thickness of the IVD, c_0 is the ion concentration at bath solution, c_0^n are reference concentrations of nutrient solutes at the endplate boundary respectively, H_A is the reference equilibrium modulus, k_0 is the reference permeability.

Based on the defined dimensionless variables and the equivalent electrochemical potential function, the new formulation of the governing equations of the specialized multiphasic theory can be obtained.

Non-dimensionalized Governing Equations:

Continuity Equations

Mixture: $$\bar{\nabla}\cdot(\bar{\mathbf{v}}^{\mathbf{s}} + \bar{\mathbf{J}}^{\mathbf{w}}) = 0 \qquad (3.32)$$

Water: $$\phi^w = \frac{\phi_o^w + e}{1+e} \qquad (3.33)$$

Ion: $$\bar{\partial}\left(\phi^{\mathbf{w}}\bar{c}^+\right)/\partial\bar{t} + \bar{\nabla}\cdot(\bar{\mathbf{J}}^+ + \phi^{\mathbf{w}}\bar{c}^+\bar{\mathbf{v}}^{\mathbf{s}}) = 0 \qquad (3.34)$$

$$\bar{\partial}\left(\phi^{\mathbf{w}}\bar{c}^-\right)/\partial\bar{t} + \bar{\nabla}\cdot(\bar{\mathbf{J}}^- + \phi^{\mathbf{w}}\bar{c}^-\bar{\mathbf{v}}^{\mathbf{s}}) = 0 \qquad (3.35)$$

$$\bar{c}^{F} = \frac{\bar{c}_0^{F}\,(1-\phi^{\mathbf{w}})\phi_0^{\mathbf{w}}}{(1-\phi_0^{\mathbf{w}})\phi^{\mathbf{w}}} \tag{3.36}$$

Nutrient solutes:

$$\bar{\partial}\left(\phi^{\mathbf{w}}\bar{c}^{n}\right)\Big/\bar{\partial}\bar{t} + \bar{\nabla}\cdot(\bar{\mathbf{J}}^{\mathbf{n}} + \phi^{\mathbf{w}}\bar{c}^{n}\bar{\mathbf{v}}^{\mathbf{s}}) = Q^{n} \tag{3.37}$$

Momentum Equations

Tissue:

$$\bar{\bar{\nabla}}\cdot\bar{\boldsymbol{\sigma}} = 0 \tag{3.38}$$

Water:

$$\bar{\mathbf{J}}^{\mathbf{w}} = -\frac{RTk\,c_0}{H_A k_0}\left(\overline{\nabla}\overline{\varepsilon}^{\mathbf{w}} + \frac{\bar{c}^{+}}{\bar{\varepsilon}^{+}}\overline{\nabla}\overline{\varepsilon}^{+} + \frac{\bar{c}^{-}}{\bar{\varepsilon}^{-}}\overline{\nabla}\overline{\varepsilon}^{-} + \frac{\bar{c}^{\mathbf{n}}}{\bar{\varepsilon}^{\mathbf{n}}}\overline{\nabla}\overline{\varepsilon}^{\mathbf{n}}\right) \tag{3.39}$$

Cation:

$$\bar{\mathbf{J}}^{+} = \bar{c}^{+}\bar{\mathbf{J}}^{\mathbf{w}} - \frac{D_0^{+}}{H_A k_0}\frac{\phi^{\mathbf{w}}\bar{c}^{+}\bar{D}^{+}}{\bar{\varepsilon}^{+}}\overline{\nabla}\overline{\varepsilon}^{+} \tag{3.40}$$

Anion:

$$\bar{\mathbf{J}}^{-} = \bar{c}^{-}\bar{\mathbf{J}}^{\mathbf{w}} - \frac{D_0^{-}}{H_A k_0}\frac{\phi^{\mathbf{w}}\bar{c}^{-}\bar{D}^{-}}{\bar{\varepsilon}^{-}}\overline{\nabla}\overline{\varepsilon}^{-} \tag{3.41}$$

Nutrient solutes:

$$\bar{\mathbf{J}}^{\mathbf{n}} = \bar{c}^{\mathbf{n}}\bar{\mathbf{J}}^{\mathbf{w}} - \frac{D_0^{\mathbf{n}}}{H_A k_0}\frac{\phi^{\mathbf{w}}\bar{c}^{\mathbf{n}}\bar{D}^{\mathbf{n}}}{\bar{\varepsilon}^{\mathbf{n}}}\overline{\nabla}\overline{\varepsilon}^{\mathbf{n}} \tag{3.42}$$

Constitutive Relation

Tissue:

$$\bar{\boldsymbol{\sigma}} = -\left[\bar{\varepsilon}^{\mathbf{w}} + \phi(\bar{c}^{+} + \bar{c}^{-} + \frac{c_0^{n}}{c_0}\bar{c}^{n}) - \bar{p}_0\right] + \left(\frac{\lambda + B_w}{RT\,c_0}\right)\bar{\bar{\nabla}}\cdot\bar{\mathbf{u}} + \frac{\mu}{RT\,c_0}[\overline{\nabla}\overline{u} + (\overline{\nabla}\overline{u})^{\mathbf{T}}] \tag{3.43}$$

Water: $$\bar{\varepsilon}^{\mathbf{w}} = \frac{p}{RT\,c_0} - \phi(\bar{c}^{+} + \bar{c}^{-} + \frac{c_0^n}{c_0}\bar{c}^{n}) + \frac{B_w}{RT\,c_0}e \tag{3.44}$$

Cation: $$\bar{\varepsilon}^{+} = \gamma_{+}\bar{c}^{+}\, exp(\frac{F_c\psi}{RT}) \tag{3.45}$$

Anion: $$\bar{\varepsilon}^{-} = \gamma_{+}\bar{c}^{-}\, exp(\frac{F_c\psi}{RT}) \tag{3.46}$$

Nutrient solutes: $$\bar{\varepsilon}^{n} = \gamma_{n}\bar{c}^{n} \tag{3.47}$$

In this study, notice that the chemical expansion stress T_c shown in equation (3.13) was neglected here for infinitesimal strain. The hindrance factor H^{α} and transport factor e^{α} (α = i, n) have not been determined for IVD tissue. The values of these parameters were assumed to be unity in equations (3.40-3.42). The interphase coupling coefficient B_w was also assumed to be zero in our further simulation.

Boundary Conditions

According to equations (3.26-3.27), the boundary conditions can be expressed as:

$$\bar{\mathbf{u}} = \bar{\mathbf{u}}^{*},\ \bar{\varepsilon}^{\alpha} = \bar{\varepsilon}^{\alpha *} \qquad (\alpha = \text{w},+,–,\text{n}), \tag{3.48}$$

$$\bar{\boldsymbol{\sigma}} \cdot \mathbf{n} = \bar{\boldsymbol{\sigma}}^{*} \cdot \mathbf{n},\ \ \bar{\mathbf{J}}^{\boldsymbol{\alpha}} \cdot \mathbf{n} = \bar{\mathbf{J}}^{\boldsymbol{\alpha} *} \cdot \mathbf{n} \qquad (\alpha = \text{w},+,–,\text{n}), \tag{3.49}$$

where **n** is the surface normal of the boundary, and * stands for the quantities in the bathing solution.

3.3.3 The Weak Formulation

In this section, the finite element formulation was constructed using the standard Galerkin weight residual method [176]. Let vector **w** and four scalar functions $w^{(1)}$, $w^{(2)}$, $w^{(3)}$ and $w^{(4)}$ be arbitrary admissible weighting functions for the five main dimensionless governing equations (3.32),(3.34-3.35),(3.37-3.38).

$$\int_{\Omega} w^{(1)}\left[\overline{\nabla}\cdot(\overline{\mathbf{v}}^{\mathbf{s}}+\overline{\mathbf{J}}^{\mathbf{w}})\right]\mathrm{d}\Omega=0\,, \tag{3.50}$$

$$\int_{\Omega} w^{(2)}\left[\partial\left(\phi^{\mathbf{w}}\overline{c}^{+}\right)\big/\partial\overline{t}+\overline{\nabla}\cdot(\overline{\mathbf{J}}^{+}+\phi^{\mathbf{w}}\overline{c}^{+}\overline{\mathbf{v}}^{\mathbf{s}})\right]\mathrm{d}\Omega=0\,, \tag{3.51}$$

$$\int_{\Omega} w^{(3)}\left[\partial\left(\phi^{\mathbf{w}}\overline{c}^{-}\right)\big/\partial\overline{t}+\overline{\nabla}\cdot(\overline{\mathbf{J}}^{-}+\phi^{\mathbf{w}}\overline{c}^{-}\overline{\mathbf{v}}^{\mathbf{s}})\right]\mathrm{d}\Omega=0\,, \tag{3.52}$$

$$\int_{\Omega} w^{(4)}\left[\partial\left(\phi^{\mathbf{w}}\overline{c}^{n}\right)\big/\partial\overline{t}+\overline{\nabla}\cdot(\overline{\mathbf{J}}^{\mathbf{n}}+\phi^{\mathbf{w}}\overline{c}^{n}\overline{\mathbf{v}}^{\mathbf{s}})\right]\mathrm{d}\Omega=0\,, \tag{3.53}$$

$$\int_{\Omega} \mathbf{w}\cdot\overline{\nabla}\cdot\overline{\boldsymbol{\sigma}}\,\mathrm{d}\Omega=0\,, \tag{3.54}$$

Based on the divergence theorem, equations (3.50-3.54) could be expressed as

$$\int_{\Omega} \mathrm{tr}[(\overline{\nabla}\mathbf{w})^{\mathrm{T}}\cdot\overline{\boldsymbol{\sigma}}]\,\mathrm{d}\Omega=\int_{\Gamma_{\mathrm{t}}}\mathbf{w}\cdot\overline{t}^{*}\,\mathrm{d}\Gamma\,, \tag{3.55}$$

$$\int_{\Omega} w^{(1)}\,\overline{\nabla}\cdot\overline{\mathbf{v}}^{\mathbf{s}}\,\mathrm{d}\Omega+\int_{\Omega}\overline{\mathbf{J}}^{\mathbf{w}}\cdot\overline{\nabla}\,w^{(1)}\,\mathrm{d}\Omega=-\int_{\Gamma_{J^{w}}} w^{(1)}\,\overline{\mathbf{J}}^{\mathbf{w}*}\cdot n\,\mathrm{d}\Gamma\,, \tag{3.56}$$

$$\int_{\Omega} w^{(2)} \bar{\partial}\left(\phi^{\mathbf{w}} \bar{c}^{+}\right) / \partial \bar{t} \mathrm{d}\Omega + \int_{\Omega} \bar{\mathbf{J}}^{+} \cdot \bar{\nabla} w^{(2)} \mathrm{d}\Omega + \int_{\Omega} w^{(2)} \bar{\nabla} \cdot (\phi^{\mathbf{w}} \bar{c}^{+} \bar{\mathbf{v}}^{\mathbf{s}}) \mathrm{d}\Omega = -\int_{\Gamma_{J^{+}}} w^{(2)} \bar{\mathbf{J}}^{+*} \cdot n \mathrm{d}\Gamma , \tag{3.57}$$

$$\int_{\Omega} w^{(3)} \bar{\partial}\left(\phi^{\mathbf{w}} \bar{c}^{-}\right) / \partial \bar{t} \mathrm{d}\Omega + \int_{\Omega} \bar{\mathbf{J}}^{-} \cdot \bar{\nabla} w^{(3)} \mathrm{d}\Omega + \int_{\Omega} w^{(3)} \bar{\nabla} \cdot (\phi^{\mathbf{w}} \bar{c}^{-} \bar{\mathbf{v}}^{\mathbf{s}}) \mathrm{d}\Omega = -\int_{\Gamma_{J^{+}}} w^{(3)} \bar{\mathbf{J}}^{-*} \cdot n \mathrm{d}\Gamma , \tag{3.58}$$

$$\int_{\Omega} w^{(4)} \bar{\partial}\left(\phi^{\mathbf{w}} \bar{c}^{\mathbf{n}}\right) / \partial \bar{t} \mathrm{d}\Omega + \int_{\Omega} \bar{\mathbf{J}}^{\mathbf{n}} \cdot \bar{\nabla} w^{(4)} \mathrm{d}\Omega + \int_{\Omega} w^{(4)} \bar{\nabla} \cdot (\phi^{\mathbf{w}} \bar{c}^{\mathbf{n}} \bar{\mathbf{v}}^{\mathbf{s}}) \mathrm{d}\Omega = -\int_{\Gamma_{J^{+}}} w^{(4)} \bar{\mathbf{J}}^{\mathbf{n}*} \cdot n \mathrm{d}\Gamma , \tag{3.59}$$

where $\mathbf{t}^{*} = \boldsymbol{\sigma}^{*} \cdot \mathbf{n}$ is the traction on the boundary of the tissue and * stands for the quantities on the tissue boundary.

In this specialized multiphasic model, there are five primary degrees of freedom (the solid displacement $\mathbf{u}$ and the modified (electro)chemical potentials ε^{α} for water, cation, anion and nutrient solutes). In the finite element analysis, governing equations for each degree of freedom were solved independently. The weak formulation was solved under PDE mode of commercial finite element software COMSOL (COMSOL Inc., Burlington, MA). Using Sun et al.[176] as reference, the modified Newton-Raphson iterative procedure was employed to handle the nonlinear terms in the above set of equations. Implicit Euler backward scheme was used to solve the resulting first-order ordinary differential equations with respect to time.

3.4 Summary

Based on the well-known triphasic theory, we further developed a multiphasic model by adding the nutrient solute phase into the model. Effect of cellular energy metabolism was considered in this model by adding a new supply term in the continuity equations for the nutrient solutes. Therefore, this model could be used to simulate the interaction between nutrient solute transport and mechanical loading in IVD tissue.

In this chapter, using mass, linear momentum conservation laws and thermo-dynamic constitutive relationships, the deduction flow for the governing equations of each phase were presented. The dimensional analysis and finite element formulation have also been described here. The relationships between the phenomenological transport parameters and the frictional coefficients have been provided in the Appendix C. The governing equations were derived based on five primary degrees of freedom (the solid displacement **u** and the modified (electro)chemical potentials ε^{α} for water, cation, anion and nutrient solutes). They were all solved independently in the finite element simulation in Chapter 4.

CHAPTER 4 EFFECT OF CARTILAGE ENDPLATE ON CELL BASED DISC REGENERATION: A FINITE ELEMENT ANALYSIS

4.1 Introduction

Low back pain is a major public health problem which causes significant social and economic burdens in the United States [1-3]. Although the exact cause for low back pain is unclear, the degenerative changes of the intervertebral disc (IVD) have been implicated as a possible primary etiologic factor [190, 191]. One of the factors which may lead to disc degeneration is the nutrient supply deficiency in the IVD [57, 192]. The nutrient environment inside the IVD has a significant effect on cell viability, proliferation rate, and cell energy metabolism [15-18, 44, 45, 193]. A fall in nutrient supply leads to a lowering of oxygen tension, glucose concentration, or pH (due to increased lactate concentrations). As a result, the ability of the disc cells to synthesize matrix proteins (e.g., collagen and proteoglycan) [194-196], and maintain its extracellular matrix (ECM) homeostasis (synthesize/breakdown) may be impaired, thus, leading to the onset of disc degeneration.

The IVD is the largest avascular cartilaginous structure in human body which lies between the bony vertebral bodies. It contributes to the flexibility and load support in the spine. To accomplish these functions, the disc has a unique architecture consisting of a centrally located nucleus pulposus (NP) surrounded superiorly and inferiorly by cartilage endplates (CEP) and peripherally by the annulus fibrosus (AF) [197]. The NP is composed of rich hydrophilic proteoglycans with negative charge, which helps to sustain axial compression. The AF is formed by a series of lamellae (concentric rings) within which the rich collagen fibers lie parallel. This highly organized collagen fiber bundle helps to resist tension and shearing forces. The CEP is a thin layer of hyaline cartilage surrounding the cranial and caudal surfaces of the disc, playing an important role in fluid and solute transport in/out of the disc.

The nutrients in the disc are mainly supplied by the capillaries and canals in the vertebral body [198-200]. The nutrients have to penetrate through the cartilage endplate layer to reach the disc extracellular matrix. It is believed that the endplate route is the main pathway for nutrition supply to the disc cell [192, 196]. Due to aging and other pathological conditions, the CEP may calcify, which reduces proteoglycan and water content, thus changing the transport properties (e.g., hydraulic permeability and solute diffusivities) of the endplate [92, 201]. Convection and diffusion through the calcified endplate is likely to be stinted thus affecting the nutrition supply to the disc [196, 202]. Therefore, under physiological loading conditions, the calcification of the CEP may significantly affect the nutrient concentrations within the disc.

Since the *in vivo* biomechanical response, transport of solutes, and cellular activities in the human IVD are difficult to measure, numerical simulation using finite element models (FEM) became an essential tool to help understand the biomechanical and nutrient environment in the IVD. Earlier studies have been limited to analyzing diffusion of the nutrient solutes inside the disc without considering the mechanical loading [19, 20]. Based on the mixture theory, we developed a multiphasic mechano-electrochemical finite element model to study the effects of static and dynamic loading on fluid and solute transport inside the human IVD [21-24]. Most recently, cellular energy metabolic rates were considered in finite element models to predict the nutrient environment within the IVD [24, 203, 204]. In these studies, the consumption rates of oxygen and glucose, as well as the production rate of lactate, were coupled with local oxygen concentrations and pH values. In addition, the relationship between cell viability and glucose concentration was also incorporated into the finite element models of the human IVD [193, 205, 206]. However, to our knowledge, the effect of cartilage endplate calcification on nutrient transport (diffusion and convection) inside the human IVD has not been fully elucidated under physiological loading conditions (i.e., day-night cyclic loading). Recently, the injection of IVD cells/stem cells in the NP region has been proposed for IVD regeneration in cell based therapies for low back pain treatment [25-27]. The success of this therapeutic approach first depends on the cell viability after the injection. Usually, the nutrient transport in degenerated discs is hindered by the calcified endplate. The increased nutrient demand due to the increase of cell density may further deteriorate the nutrient environment in the degenerate disc. Without restoring the nutrient environment, this procedure may accelerate the process of degeneration [26]. However, the impact of a cell injection coupled with already present degeneration on the nutrient environment of the disc has not been determined.

Therefore, the objective of this study was to further develop a multiphasic mechano-electrochemical 3D finite element model of human IVD by considering the disc cell energy metabolism. This model was then applied to examine the effects of endplate calcification and the injection of IVD cells on the nutrition environment inside the human IVD under physiological loading conditions. The effect of endplate calcification was simulated by a reduction of the tissue porosity (i.e., water volume faction). The effect of a cell injection was simulated by increasing the cell density in the NP region. The role of physiological mechanical loading in regulating the disc nutrient environment was also clarified by considering strain-dependent transport properties (e.g., hydraulic permeability and solute diffusivities). This study is important for understanding the pathology of IVD degeneration and provided new insights into cell based therapies for low back pain.

4.2 Materials and Methods

4.2.1 Theoretical Formulation

The theoretical framework used in our simulation was based on the specialized multiphasic weak formulations developed in Chapter 3. The human disc was modeled as an isotropic inhomogeneous mixture consisting of an intrinsically incompressible elastic solid (with fixed charge), water, ions (Na^+ and Cl^-), and nutrient solute (oxygen, glucose and lactate) phases. Moreover, in this study, the following experimentally determined constitutive relationships were used for strain-dependent hydraulic permeability (k) and solute diffusivities (D^i, D^n):

$$k = a_1\left(\frac{\phi^w}{1-\phi^w}\right)^{b_1} \tag{4.1}$$

$$\frac{D^\alpha}{D_0^\alpha} = exp\left[-a_2\left(\frac{r^\alpha}{\sqrt{k}}\right)\right]^{b_2} \tag{4.2}$$

where D_0^{α} and r^{α} (α = ions and nutrient solutes) are the diffusivity in aqueous solution and hydrodynamic radius of ions and nutrient solutes. *a* and *b* are material constants related to tissue composition and structure (Table 4.1). Since the tissue porosity was related to the tissue dilatation and the porosity at the reference configuration, the hydraulic permeability, ion diffusivity, and nutrient solute diffusivity were all strain-dependent.

The energy metabolic rates of the disc cells were taken into consideration based on the experimental results in the literature. The consumption rate of oxygen (equation 4.3) depended on oxygen concentration, as well as pH value [17]. The rate of production of lactate (equation 4.4) was based on that of NP cells in the literature [16]. A linear relationship between the pH value and lactate concentration (equation 4.5) was used to calculate the pH values in the disc [16, 203]. The glucose is primarily consumed through the process of glycolysis, in which one molecule of glucose is broken down into two lactate molecules [194, 207]. Thus, the consumption rate of glucose was set as half of the lactate production rate in this study (equation 4.6). The following constitutive relations for the disc cell metabolic rates were used in this study:

$$Q^{oxy} = -\frac{V'_{max}(pH-4.95)c^{oxy}}{K'_{m}(pH-4.59)+c^{oxy}}\rho_{cell} \tag{4.3}$$

$$Q^{lac} = exp(-2.47+0.93\,pH+0.16[Q_2]-0.0058[Q_2]^2)\rho_{cell} \tag{4.4}$$

$$pH = -0.092\,c^{lac}+7.33 \tag{4.5}$$

$$Q^{glu} = -\frac{1}{2} Q^{lac} \tag{4.6}$$

where the unit of oxygen consumption rate Q^n (n = oxygen, glucose, and lactate) is nmol/l/h, the unit of oxygen concentration c^{oxy} is µM, V'_{max} is 5.27 nmol/million cells/hr in the NP region and 3.64 nmol/million cells/hr in the AF region. K'_m is 3.4 µM in the NP region and 12.3 µM in the AF region, the unit of oxygen tension $[Q_2]$ is kPa which could be converted into to µM using oxygen solubility in water (1.0268 µmol/kPa-100ml), the unit of lactate concentration c^{lac} is mM, the units of lactate production rate Q^{lac} and glucose consumption rate Q^{glu} are nmol/l/h. Note that the single cell metabolic rates in the CEP were assumed to be equal to the values in the NP due to the lack of experimental data in the CEP.

4.2.2 Initial and Boundary Conditions

The human IVD was modeled as an inhomogeneous material with three different regions (NP, AF and CEP, Figure 4.1a). Responses of nutrient solute transport in the human lumbar disc to unconfined compression (cyclical loading) were analyzed. For this 3D problem of interest, only the upper quadrant of the sample was modeled due to the symmetry with respect to plane X=0 and plane Z=0.

Initial conditions:

$$t = 0,\ \mathbf{u} = 0,\ \varepsilon^w = \varepsilon^{w*},\ \varepsilon^i = \varepsilon^{i*},\ \varepsilon^n = 0 \tag{4.7}$$

Boundary conditions:

$$x = 0:\ u_x = 0,\ \sigma_{xy} = \sigma_{xz} = 0,\ \mathbf{J}^w = 0,\ \mathbf{J}^\alpha = 0 \tag{4.8}$$

z = 0: $u_z = 0$, $\sigma_{zx} = \sigma_{zy} = 0$, $\mathbf{J}^w = 0$, $\mathbf{J}^\alpha = 0$ (4.9)

Top CEP surface: $\boldsymbol{u} = -\mathbf{u}(t)$, $\varepsilon^w = \varepsilon^{w*}$, $\varepsilon^i = \varepsilon^{i*}$, $\varepsilon^n = \varepsilon_T^{n*}$ (4.10)

Lateral AF surface: $\boldsymbol{\sigma} \cdot \mathbf{n} = 0$, $\varepsilon^w = \varepsilon^{w*}$, $\varepsilon^i = \varepsilon^{i*}$, $\varepsilon^n = \varepsilon_L^{n*}$ (4.11)

(α: ions and nutrient solutes)

Here u_x and u_z are the components of the solid displacement **u** in X and Z directions, respectively. –**u**(t) is the pre-described displacement history (Figure 4.1d) to simulate physiological loading during the day and night.

4.2.3 Finite Element Analysis

A human lumbar IVD was modeled as an inhomogeneous material with three distinct regions: NP, AF and CEP (Figure 4.1a). The size and geometry of the human IVD in the simulation are based on previous experimental results [23, 208]. The thickness of the IVD sample was 10 mm. The thickness of the CEP was 0.6 mm [57, 209]. To investigate the effect of the CEP thickness on the nutrient environment, a thin calcified CEP with the thickness of 0.3mm was also defined and simulated. The IVD sample was initially equilibrated under pre-loaded conditions to maintain the original disc thickness. The solute concentrations at the boundaries were: c^{NaCl} is 0.15 M, c^{glu} is 4 mM at the CEP boundary and 5 mM at the lateral AF surface, c^{lac} is 0.8 mM at the CEP boundary and 0.9 mM at the lateral AF surface, c^{oxy} is 5.1 kPa at the CEP boundary and 5.8 kPa at the lateral AF surface. The IVD sample was then subjected to a cyclical loading between the two endplates (Figure 4.1d). The amplitude of the compressive strain on the whole disc for the cyclical loading was 10%. The cyclic loading included

16-hour compression and 8-hour recovery to mimic the physiological diurnal disc height changes [20]. The boundary of CEP was permeable to both water and solutes.

The 3D weak form of the finite element formulation was based on the previous work [23, 202, 210]. COMSOL software (Version 3.4, COSMOL Inc., Burlington, MA) was used to solve this 3D initial- and boundary-value problem. The program was set to the weak form mode. The upper right quadrant of the disc was modeled with 7016 second-order, tetrahedral Lagrange elements (Fig. 4.1a). As for the cyclic loading, the maximum time step for beginning each ramp compression was 10 seconds. The time step used in cyclic loading ranged from 5 seconds to 100 seconds. The convergence of the numerical model was examined by refining the mesh and tightening the tolerance. The numerical accuracy of this study was validated with the results of the 3D stress relaxation cases published in the literature [22, 23].

In this study, the effect of endplate calcification on nutrient solute transport was simulated by a reduction of the tissue porosity (i.e., water volume faction), since the hydraulic permeability and solute diffusivity are related to the tissue water content, see equations (4.1-4.2). The tissue porosity of normal CEP was 0.6, while this value in calcified endplate was 0.48 (i.e., a 20% reduction) [57, 201]. In addition, the cell density in the NP region was increased by 50%, 100%, and 150% in order to analyze the effect of cell injections in cell based therapies for low back pain treatment. The material properties for the AF, NP, and CEP were summarized in Table 4.1.

4.3 Results

The biomechanical response (strain, stress, water flux, and water pressure), electrical signals (ion concentrations and ion current/potential), and nutrient solutes transport (oxygen, glucose, and lactate concentration) in the human IVD under the physiological loading were simultaneously obtained from this multiphasic finite element model of the IVD. Only the results for the oxygen, glucose, and lactate concentration profiles were reported here.

4.3.1 Effect of Diurnal Cycle Loading

The human IVD was subjected to a diurnal cyclic loading, including a 16-hour compression and 8-hour recovery. The oxygen, glucose, and lactate concentration distributions in the normal IVD at the end of the day (i.e., the end of compression), as well as at the beginning of the day (i.e., the end of recovery), were shown in Figure 4.2. It was apparent that the nutrient concentration profiles remained almost identical during the day and night. The changes of the concentration profiles were less than 1% under the diurnal cyclic loading. Although the nutrient concentration levels were different compared to the IVD with a normal CEP, the concentration profiles also remained almost identical during the day and night in the IVD with a calcified CEP (results not shown).

The nutrition concentration distributions were not uniform in the human IVD (Figure 4.3). Generally, the oxygen and glucose concentrations decreased moving away from the blood supply at the margin of the disc. In contrast, the lactate concentration increased toward the center of the disc. Significant nutrient concentration gradients existed inside the disc with a normal CEP. The posterolateral region of the disc within the AF possessed the lowest glucose concentration of 0.540 mM, compared to the concentration of 5mM at the lateral boundary of the AF. This region also had the highest lactate concentration of 5.207 mM, compared to the concentration of 0.9mM at the at the lateral boundary of the AF. The center region of the disc within the NP possessed the lowest oxygen concentration of 0.3 kPa, compared to the concentration of 5.1 kPa at the boundary of the CEP.

4.3.2 Effect of CEP Calcification

The calcification of the CEP dramatically decreased the glucose and oxygen concentrations and increased the lactate concentration inside the IVD (Figure 4.3). There were 69.3% and 33.9% decreases in minimum glucose and oxygen concentrations in the disc with a calcified endplate, respectively. In contrast, there was a 7.3% increase in maximum lactate concentration in the disc with the calcified endplate. Moreover, the nutrient concentration levels in the NP region, compared to the AF region, were more significantly affected by the calcified CEP (Figure 4.4). There were 23.0% and 23.7% decreases in the mean concentrations of oxygen and glucose in the NP region, while 5.1% and 8.2% decreases were found in the AF region. Meanwhile, a 16.5% percent increase of mean lactate concentration was found in the NP region while an 8.7% increase was found in the AF region. The mean concentration was calculated by: $c_{mean}^{\alpha} = \iiint_V c^{\alpha}\, dxdydz / \iiint_V dxdydz$, α = oxygen, glucose, and lactate.

4.3.3 Effect of NP Cell Injection

The increase in cell density within the NP region due to the NP cell injection significantly decreased the extreme oxygen and glucose concentrations (lowest concentration inside the disc), while increasing the extreme lactate concentration (highest concentration inside the disc), as shown in Figure 4.5. The magnitude of the change of the extreme concentrations due to the cell injection also depended on the conditions of the CEP (i.e., normal, calcified, and thin calcified). Moreover, the condition of the CEP had a more significant impact on the extreme glucose concentration, than on the extreme lactate and oxygen concentrations. Specifically, the extreme glucose concentration sharply reached zero (Figure 4.5) when the NP cell density increased only 50% with the calcified CEP. Glucose concentration is a limiting factor for disc cell viability [15, 44, 45]. A Critical Zone was defined as a disc region in which the glucose concentration is lower than 0.5mM [15]. With the normal CEP, a small volume Critical Zone (0.016 cm^3) appeared in the AF region when the NP cell density increased 50% (Figure 4.6a-b). With the calcified CEP, a 50% increase of the NP cell density caused a 105. 6% increase in the volume of the Critical Zone (Figure 4.6c-d). With the thin calcified CEP, the increase in the volume of the Critical zone was reduced to 75.8% (Figure 4.6e-f).

Table 4.1 Disc tissue properties used in the numerical model.

	NP	AF	CEP
Initial water content ϕ_0^w	0.86 [a]	0.75 [a]	Normal: 0.6 [b], Calcified: 0.45
Elastic constant λ (MPa)	0.02 [c]	0.2 [c]	0.1 [d]
Elastic constant μ (MPa)	0.015 [c]	0.15 [c]	0.2 [d]
Cell density (cells/mm^3)	Normal: 4000 [e], Cell based therapy: 6000, 8000, 10000	9000 [e]	15000 [e]
Parameter for hydraulic permeability k	a_1=0.00339 nm^2 [f], b_1=3.24 [f]	a_1=0.00044 nm^2 [g], b_1=7.193 [g]	a_1=0.0248 nm^2 [h], b_1=2.154 [h]
Parameter for diffusivity D^α α: ions and nutrient solutes	a_2=1.25 nm [i], b_2=0.681 [i]	a_2=1.29 nm [i], b_2=0.372 [i]	a_2=1.29 nm [i], b_2=0.372 [i]

where r_s^α is hydrodynamic radius of ions and nutrient solutes (r_s^+ = 0.197 nm; r_s^- = 0.142 nm; r_s^{oxy} = 0.1 nm; r_s^{lac} = 0.255 nm; r_s^{glu} = 0.3 nm), D_0^α is diffusivity of ions and nutrient solutes in aqueous solution (D_0^+ = 1.28*10^{-9} m^2/s, D_0^- = 1.77*10^{-9} m^2/s, D_0^{oxy} = 3.0*10^{-9} m^2/s, D_0^{oxy} = 1.28*10^{-9} m^2/s, D_0^{glu} = 0.92*10^{-9} m^2/s).

[a] Yao and Gu, 2007.
[b] Roberts et al., 1989; Setton et al., 1993.
[c] Yao and Gu, 2006.
[d] Mow et al., 2002; Yao and Gu, 2004.
[e] Maroudas et al., 1975.
[f] Gu et al., 2003, from agarose gels.
[g] Gu and Yao, 2003, from porcine AF tissue.
[h] Maroudas et al., 1975; Yao and Gu, 2004.
[i] Gu et al., 2004, from porcine AF tissue and agarose gels.

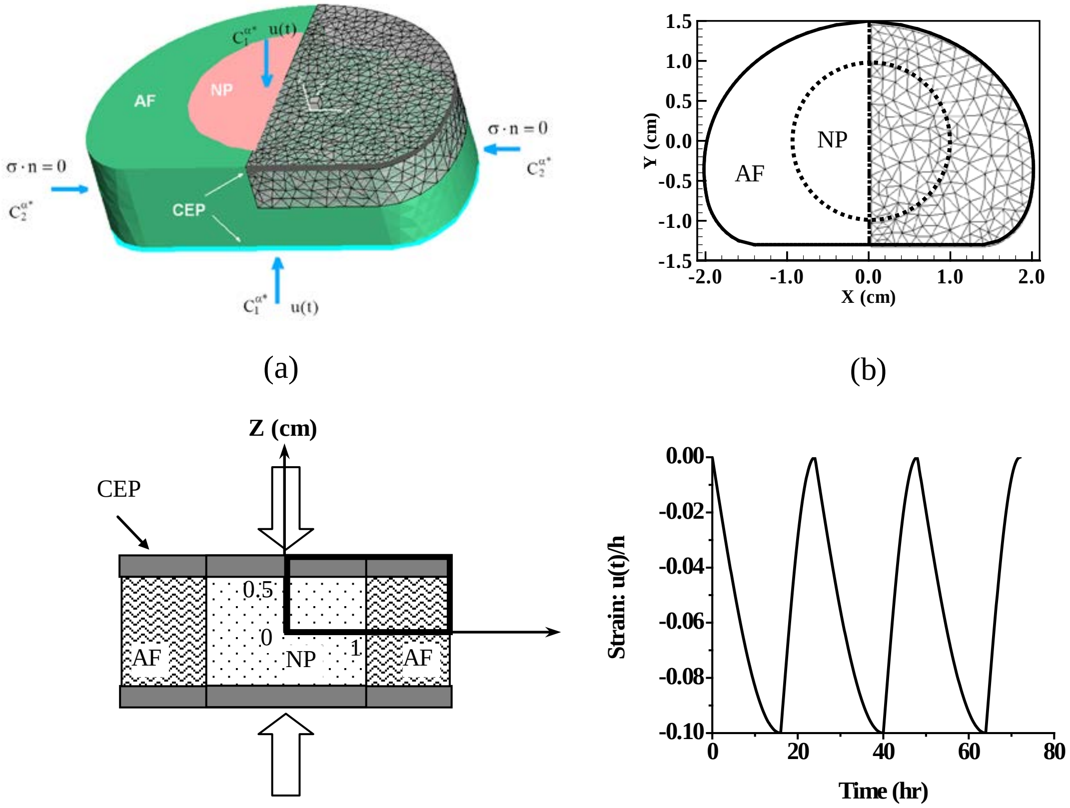

(a) (b)

(c) (d)

Figure 4.1 Geometry of the human lumbar IVD model and loading protocol in the simulation. (a) 3D view of the disc model, (b) disc geometry, (c) test configuration, and (d) cyclic loading on the top and bottom of the disc (Strain = cyclic displacement u(t) / initial height of the disc h).

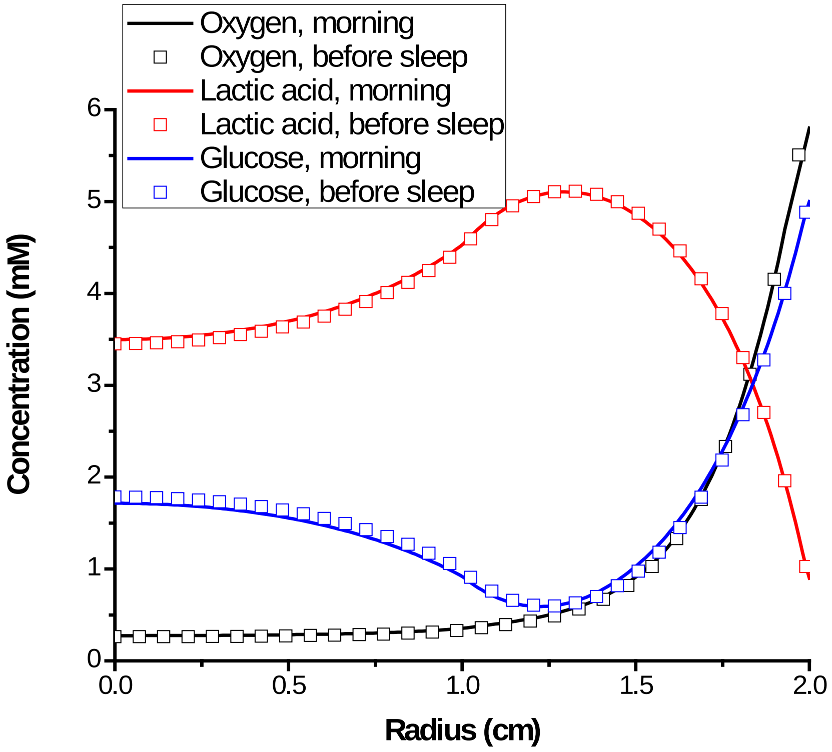
Oxygen, morning
Oxygen, before sleep
Lactic acid, morning
Lactic acid, before sleep
Glucose, morning
Glucose, before sleep
Concentration (mM)
0
1
2
3
4
5
6
0.0
0.5
1.0
1.5
2.0
Radius (cm)

(a)

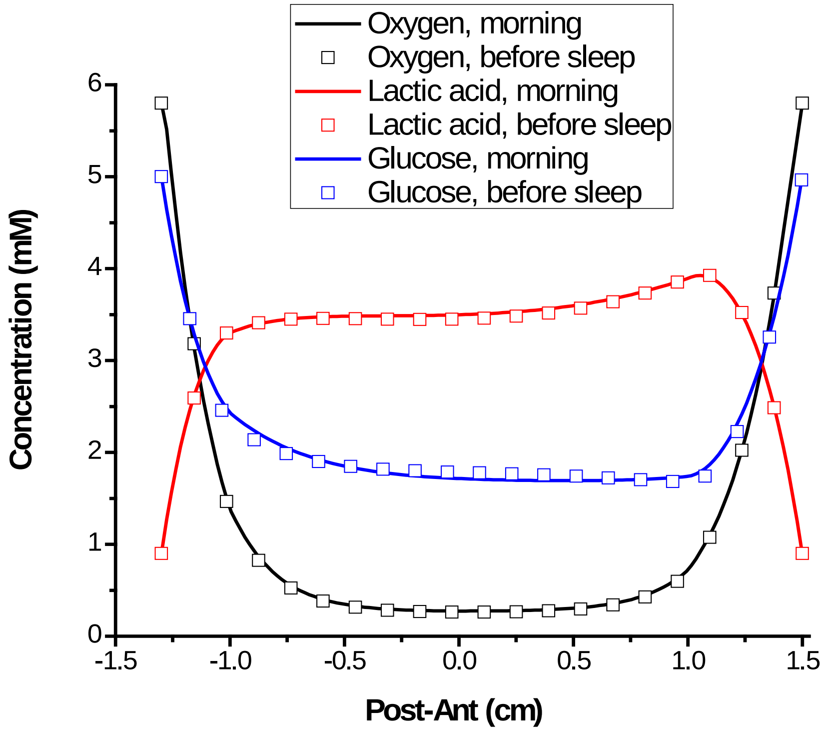

(b)

Figure 4.2 Nutrient solute (oxygen, glucose and lactate) concentration distributions inside the human IVD in the morning (end of the recovery) and at night (end of the compression): (a) in the x-direction from the center to the lateral and (b) in the y-direction from the posterior to the anterior.

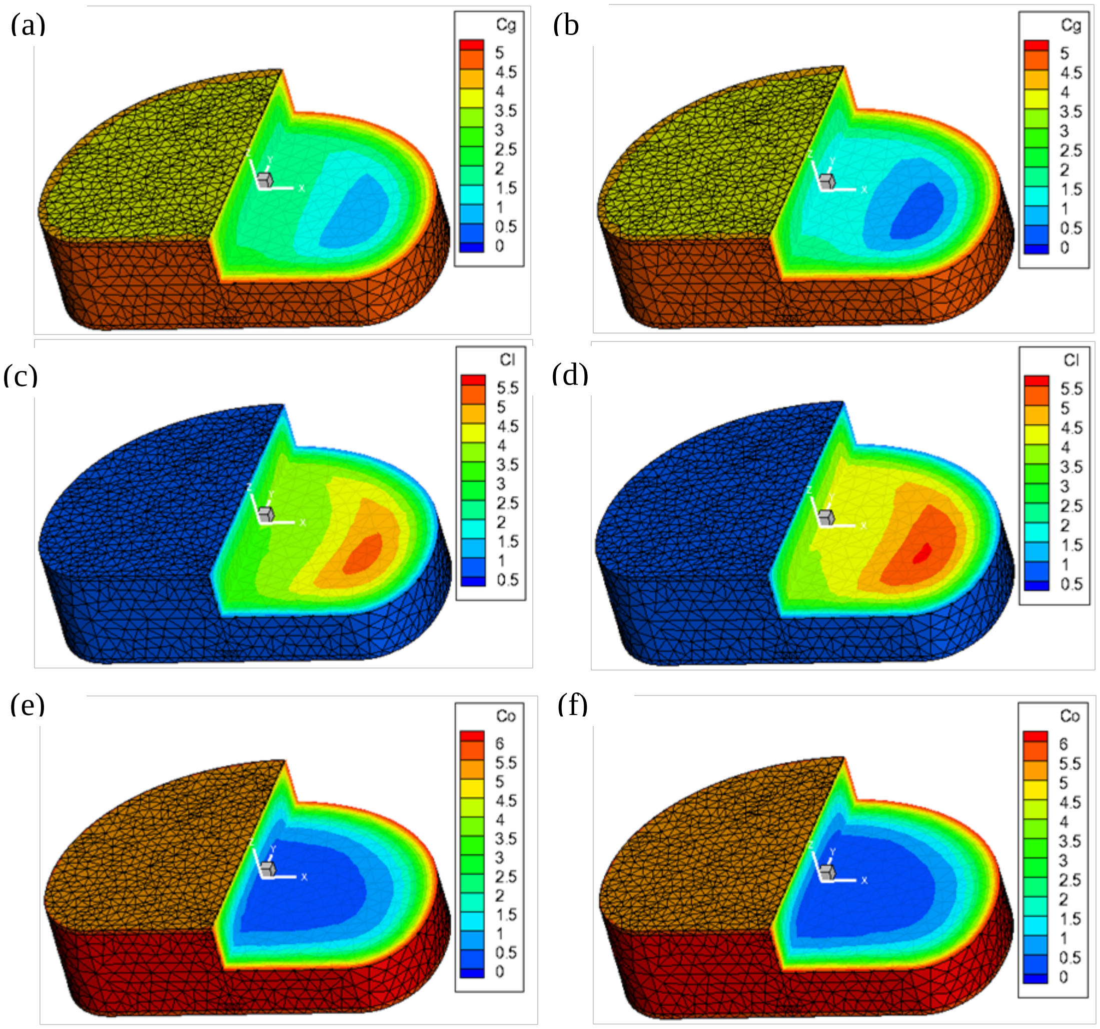

Figure 4.3 Effect of CEP calcification on 3D nutrient solute (oxygen c_o, glucose c_g and lactate c_l) concentration distributions inside the human IVD: (a) (c) (e) with a normal CEP and (b) (d) (f) with a calcified CEP. (Concentration unit: mM)

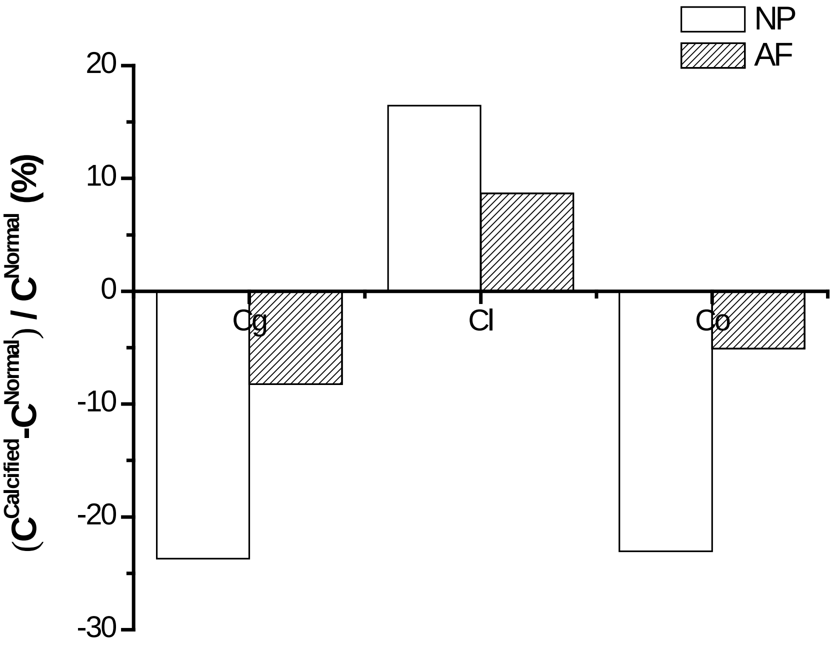

Figure 4.4 Effect of CEP calcification on mean concentrations in the NP and AF regions. The change of the concentration was normalized by the concentration with a normal CEP.

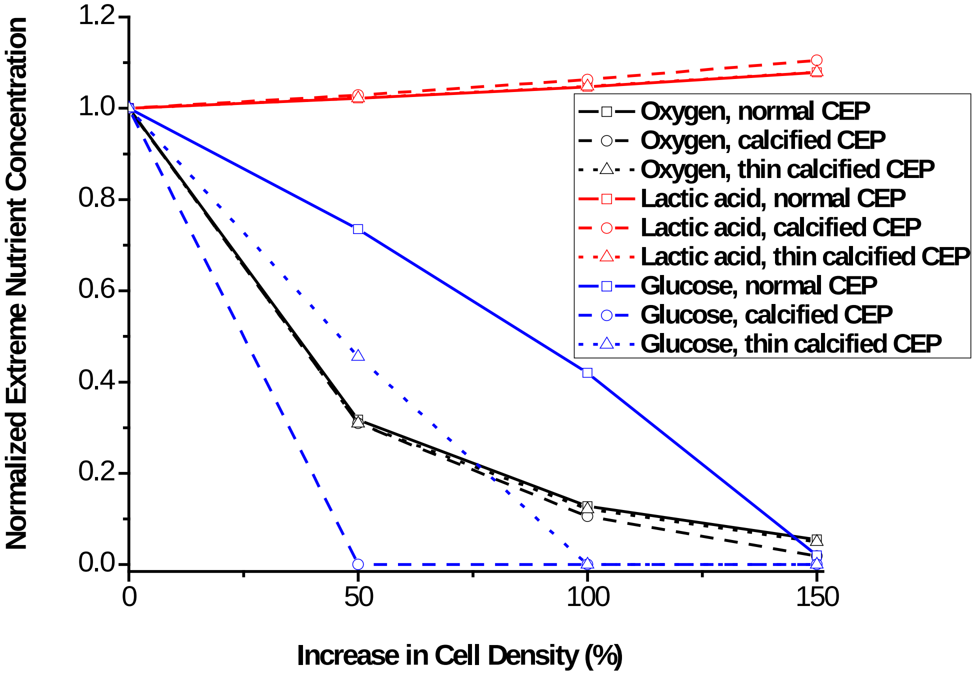

Figure 4.5 Effect of increase in cell density on the extreme nutrient concentrations inside human IVD. Cell density in the NP region is increased by 50%, 100%, and 150%. The simulated cases include disc with a normal CEP, calcified CEP, and thin calcified CEP (50% of the full thickness).

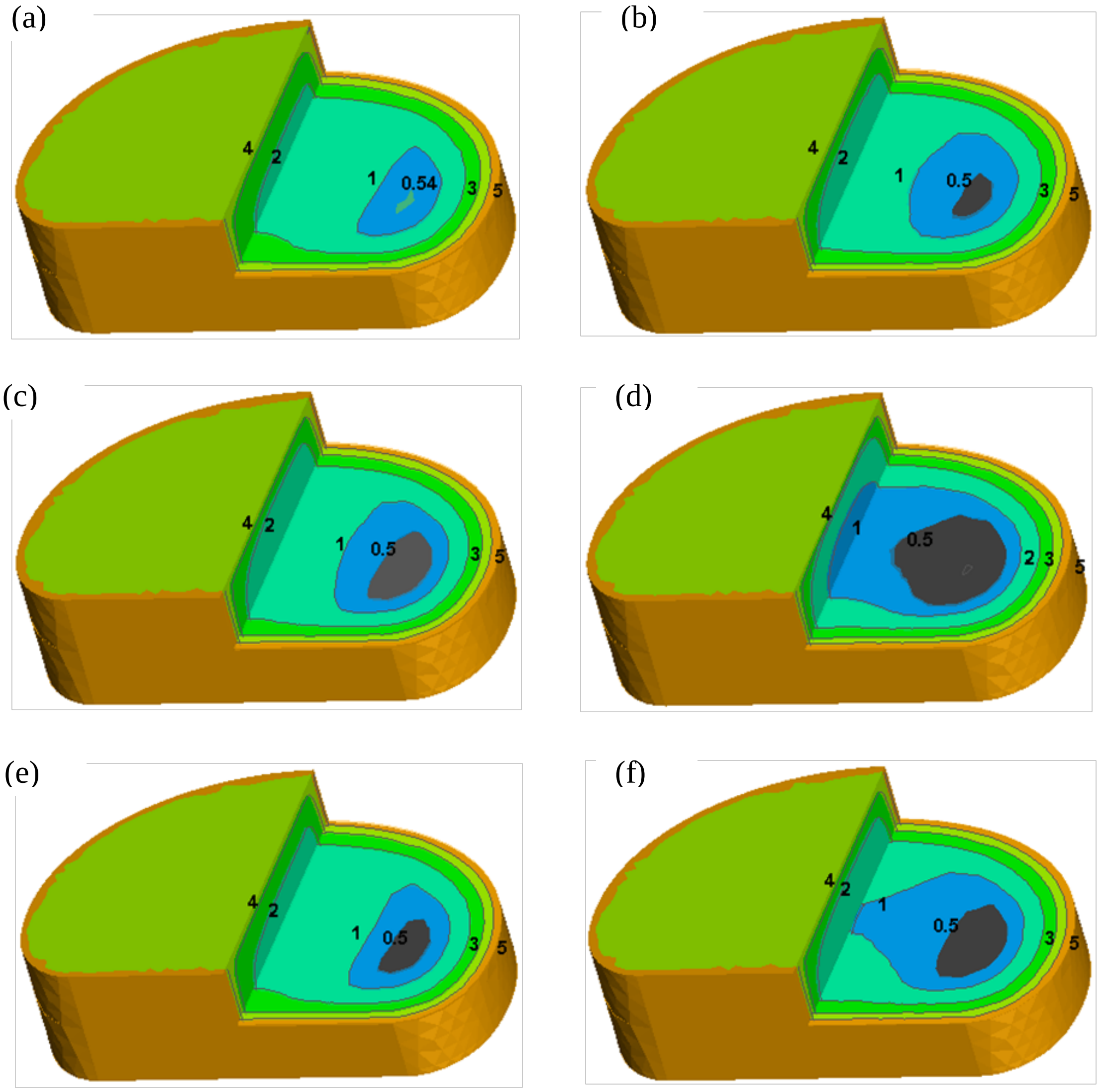

Figure 4.6 Effect of increase in cell density on 3D glucose concentration distribution in the disc with a normal CEP (a) (b), calcified CEP (c) (d), and thin calcified CEP (e) (f). The grey color regions indicate the Critical Zones in which the glucose concentration is lower than 0.5 mM [15].

4.4 Discussion

The object of this study was to develop a multiphasic mechano-electrochemical 3D finite element model of human IVD to investigate the effects of endplate calcification and the injection of IVD cells on the nutrition environment inside the human IVD under physiological loading conditions. In comparison with earlier models [19-24, 203-205], the present study is the first to compute the 3D concentration profiles of oxygen, glucose, and lactate in a human lumbar disc under physiological diurnal cyclic loading. For the baseline case (i.e., no CEP calcification and no cell injection), the computed minimum oxygen concentration of 0.3 kPa at the center region of the disc falls within measured range of 0.3-1.1 kPa [207]. The computed minimum glucose concentrations of 0.54 mM in the inner AF is in agreement with the measured range of 0.5-2.5 mM in the AF of scoliotic discs [45]. The computed maximum lactate concentration of 5.21 mM also falls within measured range of 2-6 mM [211]. These agreements between the model predictions and experimental measurements validated the present finite element model of human IVD to a certain extent. In addition, the values of the extreme oxygen, glucose, and lactate concentrations in the disc with a normal CEP are also consistent with the previous simulation studies [193, 212, 213].

The advantage of our model was that it was capable of simulating the nutrient solute transport inside the disc coupled with mechanical loading. The strain dependent hydraulic permeability and nutrient solute diffusivities, as shown in Equations (4.1-4.2), were determined in previous experimental studies (Table 4.1). A decrease in water content due to the tissue consolidation could thus reduce the hydraulic permeability and solute diffusivities. Consequently, the convection and diffusion could be hindered. The human IVD experiences a diurnal cyclic loading *in vivo* [20]. In this study, a cyclical loading (compression during the day then recovery during the night) was considered to mimic the physiological loading on the IVD. Our results showed that there were no significant differences in nutrient solute concentration distributions inside the disc between the day and night (Figure 4.2). It indicated that the loading induced fluid flow doesn't alter the nutrient transport and the nutrient environment maintains stable inside the IVD under the physical diurnal loading condition. Previous studies [214-216] have proposed that fluid flow induced by the mechanical loading may enhance or hinder the solute transport in the disc. However, for small solutes such as oxygen, glucose, and lactate, diffusion is a dominate transport mechanism inside the disc since the convective contribution by 'pumping' of small solutes is relatively small [20, 92, 207, 217]. Although several studies have shown that the long-term sustained static compression may change the nutrient concentration distribution inside the IVD [21, 22, 24, 205, 206], the present study further confirmed that the nutrient environment maintains a stable state under the physiological diurnal loading condition. With a stable nutrient environment, the disc cell energy metabolism also keeps a constant rate during the day and night under the physiological condition. This may be beneficial to disc cell homeostasis.

Along with the aging process, calcification of the CEP may appear and cause perturbation in its transport properties [92, 201]. The reduction of the fluid and solute permeability due to the CEP calcification may impede nutrition supply to the disc [193, 212, 213]. As shown in our results, calcification of the CEP significantly changed the nutrient solute distribution inside the human IVD, including a significant fall of the minimum oxygen and glucose concentrations and a significant increase of maximum lactate concentration (Figure 4.3). Moreover, the effect of CEP calcification was more significant in the NP region (Figure 4.4) as the main source of nutrition supply for the NP is from capillaries and canals in the vertebral body adjacent to the endplate [198-200]. Our results also showed that the CEP calcification significantly increased the size of the Critical Zone (Figure 4.6). Note that the Critical Zone was defined as a disc region in which the glucose concentration is lower than 0.5mM. The glucose concentration is a limiting factor for the disc cell viability. A previous cell culture study has shown that disc cell death occurs if the glucose concentration is lower than 0.5 mM for more than 3 days [44]. Therefore the CEP calcification results in a decrease of nutrient supply to the disc. This may lead to changes in the disc cell viability and cellular metabolism, which in turn alters the extracellular matrix homeostasis (breakdown/synthesize). The imbalance of the matrix synthesis and degradation implies the onset of the process of disc degeneration.

In order to develop new treatments for the IVD degeneration associated low back pain, injection of autologous NP/chondrocyte cells or mesenchymal stem cells (MSCs) to the degenerated disc has been proposed for disc regeneration [25-27]. Our results have shown that increasing the cell density in the NP region may increase cellular metabolism, which in turn caused further deterioration of the nutrient environment in the degenerated disc. Even in a disc with a normal CEP, a critical zone appeared immediately once the cell density in the NP region increased by 50% (Figure 4.5(b)). The critical zone was doubled with the presence of a calcified CEP. Interestingly, after cutting down the calcified CEP to a half of its thickness, the volume of the Critical Zone was decreased to a half of its volume with the full thickness CEP. Our results suggested that nutrient supply was an essential factor which needs to be considered in cell based therapies for human IVD regeneration. Unless it can be assured that a degenerate disc has a nutrient supply which can support the implanted cells, treatment using a cell therapy approach is both pointless and unethical [218]. Our results also suggested that reducing the thickness of the calcified CEP could be an option to restore the nutrient environment in degenerative discs for cell based therapies. In addition, in order to address the nutrition supply concern, large animal species will be a more appropriate model for testing this approach.

There are a few limitations in our finite element model. In order to improve the accuracy of the simulation, more information about the geometry of the CEP and the region of calcification are needed. The simplified geometry in this study may overestimate the size of the CEP. The mechanical and transport properties (Table 4.1) used in this study are mainly from the animal data. These properties for human IVD, especially for the CEP, are largely unavailable. The anisotropy of the mechanical and transport properties need to be considered, especially in the AF region, in our future work [219, 220]. As for energy metabolism properties in the NP and AF, there is barely any data available for the human IVD. Consequently, bovine and porcine cell data were used in this study. Moreover, the glucose consumption rate (GCR) was assumed to be the half of the lactic production rate based on the glycolysis assumption. The GCR may also depend on the oxygen level [44]. Meanwhile, the cell viability needs to be considered in future studies by correlating it with the pH value and glucose concentration. The development of a new constitutive relation for IVD cell viability, based on experiment data, is needed to further improve our model.

The effect of mechanical strain on fix charge density was incorporated in this model, see equations (3.4) and (3.6-3.7). Mechanical loading could alter extracellular osmotic environment by changing the fixed charge density in the ECM. Moreover, disc degeneration will induce loss of PG content from the matrix, resulting in change of fix charge density and the extracellular osmotic environment. Previous studies have found that cellular responses such as gene expression and collagen synthesis were significantly affected by the osmotic environment [55,56]. Therefore, the energy metabolic activities of IVD cells may also be changed due to the change in the extracellular osmotic environment. A more accurate prediction of the nutrient distribution in the human IVD could be expected once the effects of osmolarity on energy metabolic activities of IVD cells are quantitatively characterized in the future.

4.5 Summary

In summary, we found that the nutrient solute distribution inside the disc was maintained at a stable state during the day and night. The physiological diurnal cyclic loading didn't change the nutrient environment in the human IVD. The cartilage endplate played a significant role in the nutrient supply to the human IVD. Calcification of the cartilage endplate significantly reduced the nutrient levels in the human IVD. Therefore, in cell based therapies for IVD regeneration, the increased nutrient demand by cell injection needs to be seriously considered. Excessive amounts of injected cells may cause further deterioration of the nutrient environment in the degenerated disc. This study is important for understanding the pathology of IVD degeneration and providing new insights into cell based therapies for low back pain.

CHAPTER 5 VISCOELASTIC PROPERTIES OF CARTILAGE ENDPLATE

5.1 Introduction

The IVD is comprised of three major components: AF, NP, and cartilaginous end-plate (CEP) (Figure 5.1). The NP is composed of randomly oriented collagen fibrils enmeshed in a mucoprotein gel. It is surrounded on its periphery by the AF, and superiorly and inferiorly by CEPs. The AF is formed by a series of concentric encircling lamellae, which are free from macroscopic ruptures. The CEP is a thin layer of hyaline cartilage surrounding the cranial and caudal surfaces of the central regions of the disc. The human disc is comprised mostly of water (65-90% wet weight) with significant quantities of collagen (15-65% dry weight), proteoglycan (PG) (10-60% dry weight) and other matrix proteins (15-45% dry weight) [221]. Differences in biochemical composition and structure distinguish the different regions of the disc, suggesting that each component may have a unique mechanical role [197].

The IVD is the largest avascular structure in the human body. The nutrients that disc cells require for maintaining disc health are supplied by blood vessels at the margins of the disc. Two possible pathways for nutrient transport into IVD include through the CEP as well as through the periannular [12]. Most in vivo studies (using animal models) and in vitro studies suggested that the end-plate route (perpendicular to the CEP at the central portion of the disc) was the main pathway for exchange of fluid and solutes between the NP (and inner AF) and surrounding blood vessels [12, 54, 207, 214, 222]. Therefore, the knowledge of transport properties of the CEP is crucial for understanding the mechanism of disc nutrition.

Transport of fluid and solutes (including ions) in tissue is mainly governed by transport properties such as hydraulic permeability and solute diffusivities [40, 100], which are all mechanical strain dependent. Although many studies have been done to determine the mechanical and transport properties of the AF and NP, the presence of CEP data is rare. Currently, the understanding of the mechanical and transport behaviors of the CEP mainly comes from present knowledge of articular cartilage. However, the finding of significant differences in the biochemical composition of the human CEP and human articular cartilage strongly suggests that the mechanisms for viscoelastic behavior and fluid and solute transport might be fundamentally different for the two tissues in suit [57, 223]. Based on the biphasic theory, Setton *et al* studied the compressive mechanical properties of the baboon CEP using a confined compression test [223]. The specimens (6mm diameter) were prepared from the central portion of the CEP and loaded in the direction perpendicular to the CEP. The compressive aggregate modulus of the baboon CEP is similar to that of bovine and human articular cartilages; however, the permeability of the end-plate is significantly different from human articular cartilage. To date, this is the only study that determined mechanical and fluid transport properties of the CEP. The transport behaviors of solutes of different sizes and conformations were studied in human CEP by Roberts *et al* [92]. The partition coefficient and diffusion distance of solutes ranging in molecular weight from 115 to 70,000d were measured. To date, mechanical and transport properties of CEP still have not been well characterized. In this study, we will determine the compressive mechanical properties and hydraulic permeability of the bovine cartilage endplate and further characterize its related biochemical composition.

5.2 Materials and Methods

5.2.1 Specimen Preparation

Bovine (2-4 years old) cartilaginous endplates were harvested from bovine tails (C2-4) obtained from a local slaughterhouse within 4 hours of death. The discs were opened with a scalpel, then immediately wrapped in a plastic membrane and gauze soaked in a normal saline solution with protease inhibitors and stored at -80°C until mechanical testing. In total, fourteen morphologically healthy bovine CEPs in the center region and eighteen bovine CEPs in the lateral region were sectioned and used for mechanical testing. The geometry, composition, and resting stress of the bovine caudal disks were demonstrated to be similar with that of human lumbar disks [224, 225].

Cylindrical tissue plugs together with the bone were obtained from the center and lateral regions of the bovine disc (Figure 5.1a), using a 5mm corneal trephine. Care was taken when separating the disc tissue from the bone under a dissecting microscope (Olympus SZX7). A sledge microtome (Leica SM2400) was used to remove the NP or AF tissue above the CEP to prepare disk shaped samples with an average height of 0.6 mm and a diameter of 5mm. The thickness of the CEP has been found to be ~0.6 mm in our histological study as well as in the literature [57].

In addition, sagittal and frontal slices were taken from adjacent tissue plugs together with the bone from the center and lateral regions for histological study. The segments were rapidly fixed in 10% neutral buffered formalin, decalcified, and paraffin wax embedded. Ehrlich’s hematoxylin and eosin (H&E) was used with the wax sections

(7μm) in order to study morphological characteristics and histological parameters of the cartilage endplate, including the tissue thickness in the center and lateral regions.

5.2.2 Mechanical Characterization

A Perkin-Elmer 7e Dynamic Mechanical Analyzer (DMA) was used for the mechanical tests of the CEP from the center and lateral regions. The DMA displacement and force measurement precision was 0.5 μm and 0.5 mN, respectively. A test chamber was designed for uniaxial confined compression testing (Figure 5.1b). A smooth and stainless steel ring was used to prevent radial deformation. The specimens were then compressed axially by the test probe (5mm diameter) on top and a rigid porous permeable porous platen (20μm average pore size) on the bottom [226-228]. Figure 5.1c shows schematically the mechanical testing protocol which will be described in further detail as follows.

Similar to the mechanical testing protocol in our previous studies on IVD tissues, hydrogels and the TMJ disc [227-229], the specimens were firstly subjected to a minute compressive tare load (0.01 N) to measure initial height for all mechanical tests. Then PBS (pH 7.4) was carefully injected into the testing chamber and the equilibrium swelling pressure of the specimen (after ~40 minutes) was measured with the strain held constant at the initial height. Due to the unique swelling property of CEP in PBS, interdigitation between the porous platen and the specimen was ensured and the specimen was fully confined at its periphery. Secondly, a creep test (2 hour) was performed by applying a stress equal to 1.2 times the equilibrium stress at the initial height. The criterion for choosing the amplitude of load for the creep test was based on the fact that the resultant creep strain at the end of the creep test was on average 3-4% of the initial specimen height. This small creep strain was chosen to satisfy the hypothesis of the linear biphasic theory for following curve fitting. It was also proved that a steady state of creep was achieved after 2 hours of compression in all samples.

By curve-fitting the creep data to the biphasic theory developed by Mow *et al.* [160], the equilibrium compressive aggregate modulus (H_A) and hydraulic permeability coefficient (k) were determined for the CEP in both the center region and lateral region.

5.2.3 Biochemical Analysis

CEPs from the center and lateral regions, and NP and AF (control groups) from six bovine caudal disks were lyophilized to measure the dry weight, and the water content was determined using the difference between the wet and dry tissue weight. The lyophilized tissue was then assayed for total collagen and glycosaminoglycans (GAG) content. A modified chloramine-T hydroxyproline assay (Bergman and Loxley, 1970) was used to determine the total collagen content (μg collagen/μg dry tissue, unit: %). Collagen standards (Accurate Chemical and Scientific Corporation, Westbury, NY) were chosen for a more direct comparison instead of using hydroxyproline standards. The Blyscan Glycosaminoglycan Assay kit (Biocolor, Newtonabbey, Northern Ireland) was used to determine the total glycosaminoglycans (GAG) content based on 1,9-dimethylmethylene blue dye binding, with standards provided by the manufacturer.

5.2.4 Statistical Analysis

Regional differences between the biphasic viscoelastic properties of the CEP and biochemical quantities of CEP, NP and AF were examined using SPSS statistic software. Student’s t-test and One-way ANOVA (Tukey’s post hoc tests) were performed to determine if significant regional differences existed in the mechanical properties of CEP and the biochemical properties between CEP, NP, and AF. Statistical differences were reported at p-values < 0.05.

5.3 Results

5.3.1 Macroscopic and Histological Appearance

Eighteen bovine discs were dissected and morphologically analyzed for degeneration grade. All of them could be classified as grade I based on the Thompson grading system [230]. The lamellae structure in the AF region was visible and the nucleus was gelatinous. A thin hyaline cartilage layer called the CEP was found between the interface of the disc and bone. CEP swelled immediately once exposed to PBS solution, as well as NP and AF tissue. Based on our histology study, the cell density in the CEP layer was much higher than that in both the NP and AF regions (Figure 5.2). The collagen fibers in the NP region were arranged parallel to the NP/CEP interface, while those in the AF region were at an angle to the AF/CEP interface. The collagen fibers from the disc also seemed to continue into the endplate. However, the collagen fiber content in the endplate appeared to be much higher than in the NP and AF regions. In addition, the thickness of the endplate did not vary significantly with the regions, with a value of 0.60±0.08 mm in the center region and 0.61±0.05 mm in the lateral region (n=6 each region).

5.3.2 Creep Compression Behavior

The initial heights of the CEPs were measured before the creep test and the values were also consistent with the initial height measured in our histological studies (Table 5.1). The creep data were well fitted to the biphasic theory in determining the equilibrium compressive aggregate modulus and hydraulic permeability (Figure 5.3). A significant regional difference was found for the aggregate modulus in the CEP; 0.23±0.15 MPa in the center region was approximately 1/3 of that in the lateral region (0.83±0.26 MPa). No significant regional differences were observed for the hydraulic permeability in the CEP (center region: $0.13\pm0.07\times10^{-15}$ m^4/Ns and lateral region: $0.09\pm0.03\times10^{-15}$ m^4/Ns). A significant regional difference was also found for the swelling pressure in the CEP (center region: 0.09±0.05 MPa and lateral region: 0.21±0.07 MPa) (Table 5.1).

5.3.3 Biochemical Composition

Mean and standard deviation values of the water content (% wet weight), total collagen content (% dry weight), and total GAG content (% dry weight) of bovine CEP as well as NP and AF were shown in Figure 5.5. A significant regional difference was found for water content in the CEP between the center and lateral regions (center region: 75.6±3.1% and lateral region: 70.0±1.8%). Compared with that in the NP region (79.7±2.1%), the water content was significantly lower in the CEP.

A significant regional difference was also found for GAG content in the CEP between the center and lateral regions (center region: 20.4±3.1% and lateral region: 11.8±2.1%). Compared with that in the NP region (26.8±6.2%), the GAG content was significantly lower in the CEP. For collagen content, a significant regional difference was also found in the CEP between the center and lateral regions (center region: 41.1±9.5% and lateral region: 73.8±10.8%). Compared with that in the NP and AF regions (NP: 28.5±5.0% and AF: 54.2±12.9), collagen content was significantly higher in the CEP at the center and lateral regions, respectively.

Table 5.1 Results (mean ± SD) of biphasic viscoelastic properties for bovine CEP in the central and lateral regions. Statistical differences were found for the aggregate modulus between the central and lateral regions of the endplate, while no statistical regional difference was found for the permeability between the regions.

	Central region (n=14)	Lateral region (n=18)
Initial height (mm)	0.60±0.07	0.59±0.08
Aggregate modulus H_A (MPa)	0.23±0.15	0.83±0.26
Permeability k (10^{-15} m^4/Ns)	0.13±0.07	0.09±0.03
Swelling pressure (MPa)	0.09±0.05	0.21±0.07

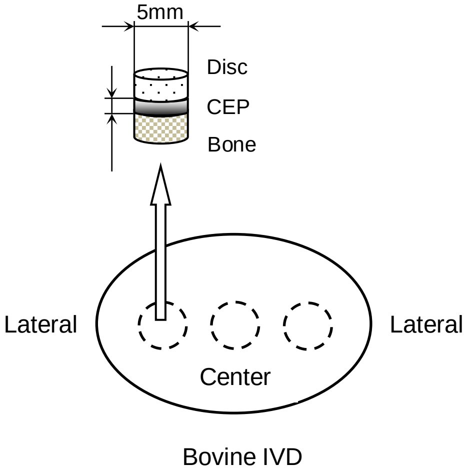
5mm
Disc
CEP
Bone
Lateral
Lateral
Center
Bovine IVD

(a)

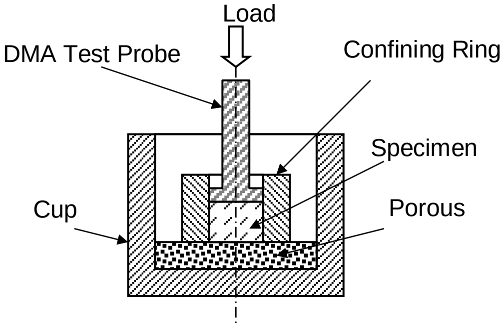
Load
DMA Test Probe
Confining Ring
Specimen
Cup
Porous

(b)

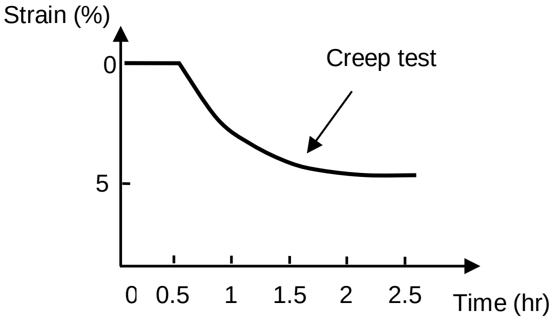

(c)

Figure 5.1 (a) Schematic of specimen preparation. The region and size of test specimens are shown. (b) Schematic of a uniaxial and confined compression test chamber. (c) Schematic of the mechanical testing protocol.

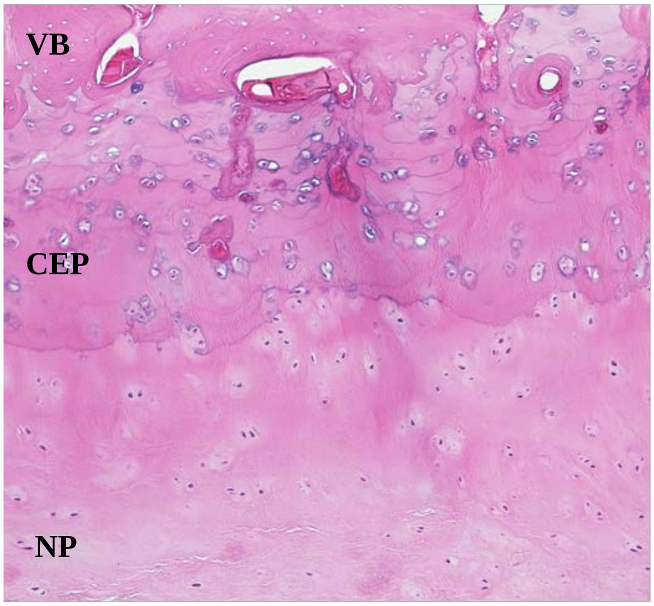

(a)

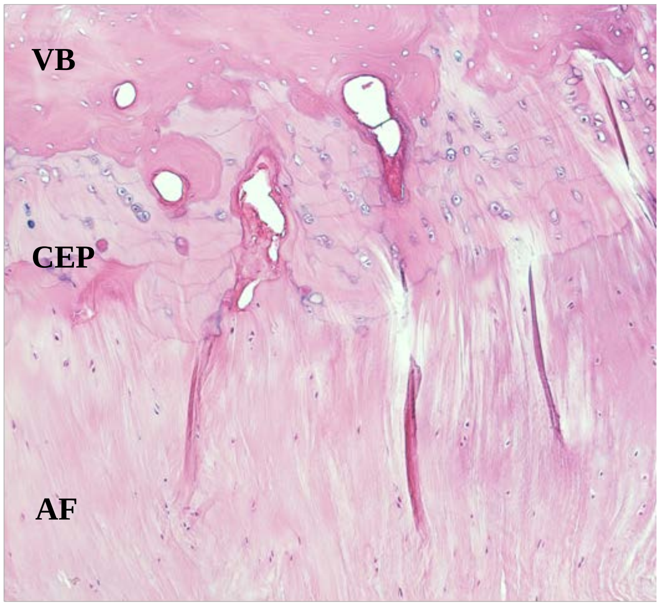

(b)

Figure 5.2 Histological section of bovine C2-3 (original magnification ×10), showing (a) the nucleus pulposus (NP), the cartilage endplate (CEP), and the vertebral body (VB) and (b) the annulus fibrosus (AF), the CEP, and the VB.

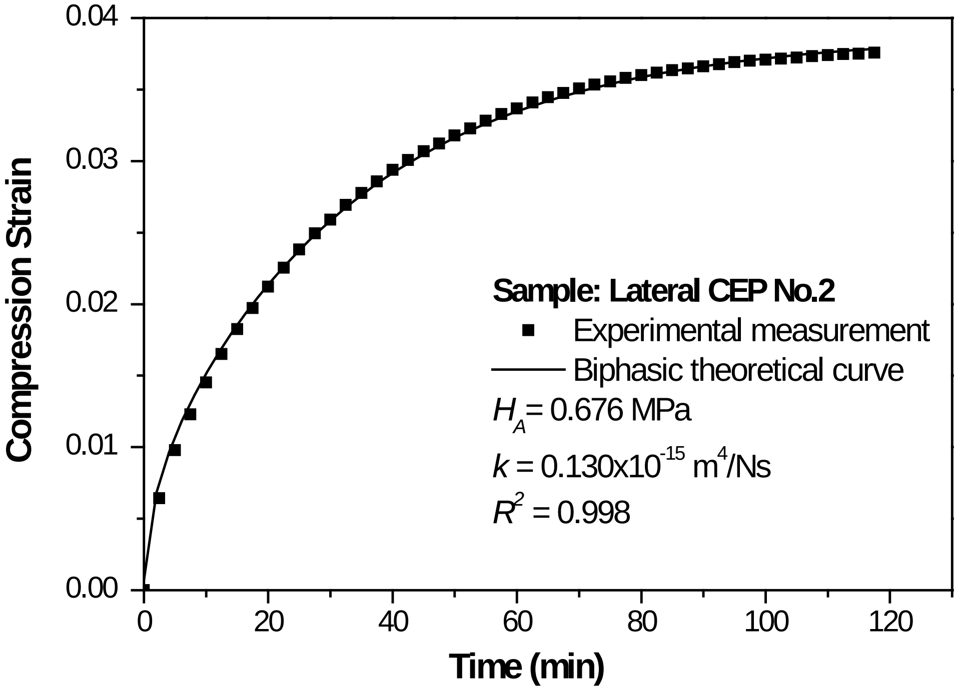

Figure 5.3 Typical biphasic creep behavior of a bovine CEP. A good agreement is shown between the theoretical prediction and the experimental result.

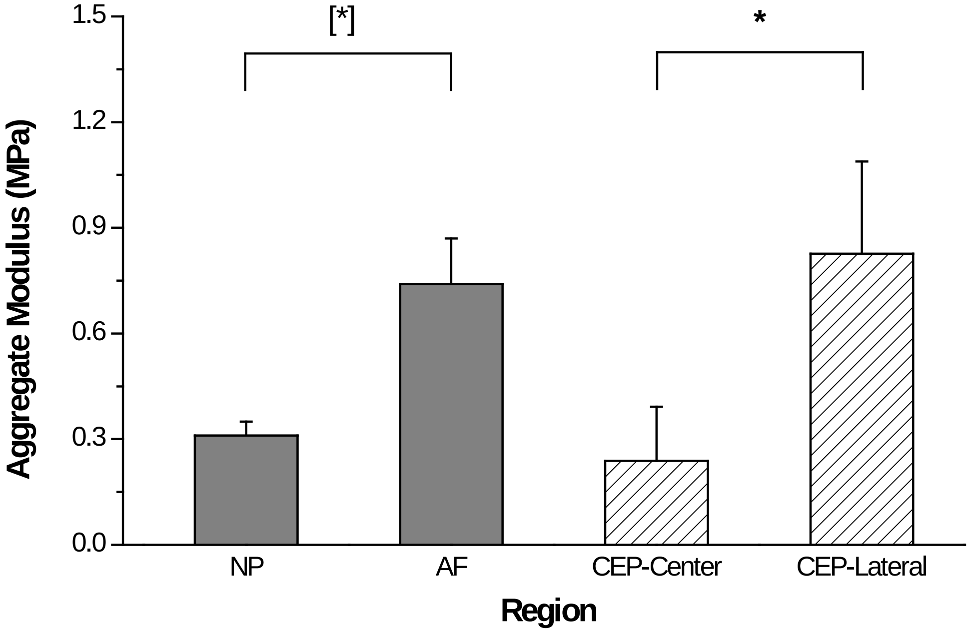

[*]
*
1.5
1.2
0.9
0.6
0.3
0.0
Aggregate Modulus (MPa)
NP
AF
CEP-Center
CEP-Lateral
Region

(a)

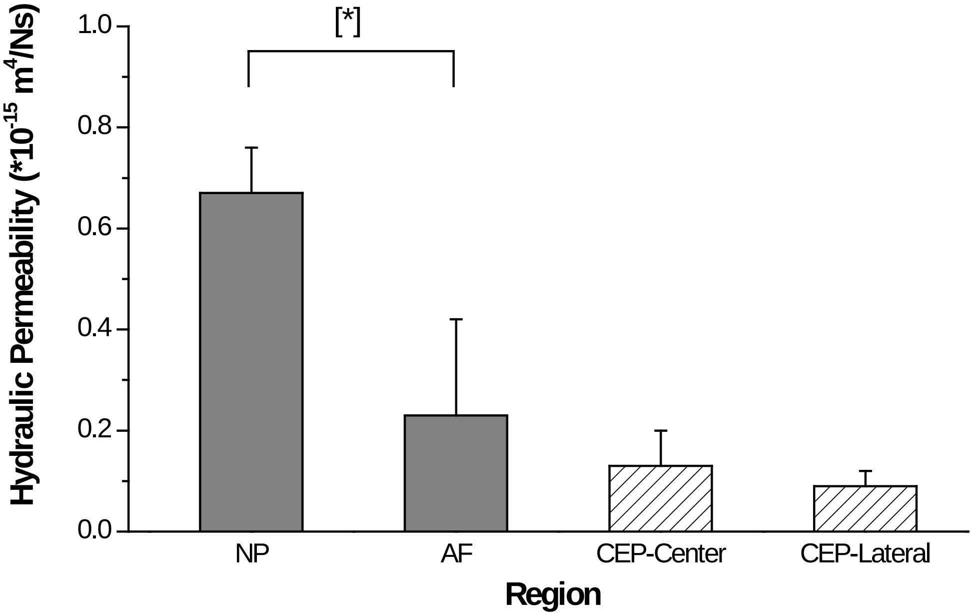

(b)

Figure 5.4 Comparison of (a) aggregate modulus H_A (b) permeability k of bovine CEP determined in this study (CEP-Center and CEP-Lateral) and bovine IVD tissue found in the literature (NP and AF) [231]. For the aggregate modulus, a significant regional variation was detected in the CEP between the center and lateral regions ($*p < 0.05$).The aggregate modulus of the CEP in the center and lateral regions were consistent with that of the NP and AF regions, respectively ($^{[*]}p < 0.05$ [231]). For hydraulic permeability, no significant regional variations were detected in the CEP between the center and lateral regions. Compared with that in the NP and AF [231], the permeability in the CEP is found to be much smaller.

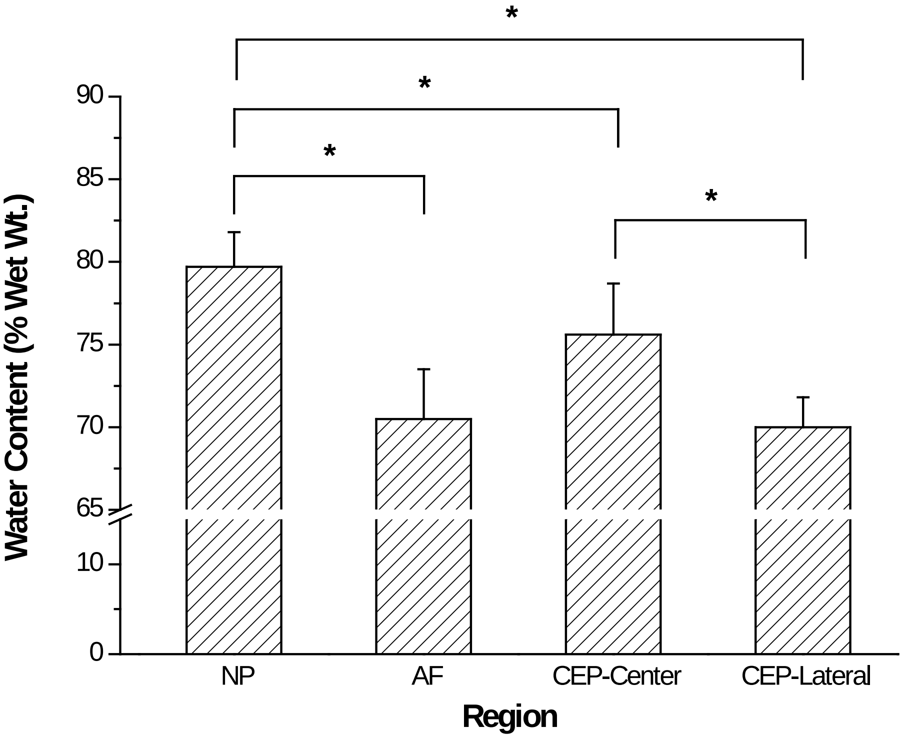
*
*
*
*
90
85
80
75
70
65
10
0
Water Content (% Wet Wt.)
NP
AF
CEP-Center
CEP-Lateral
Region

(a)

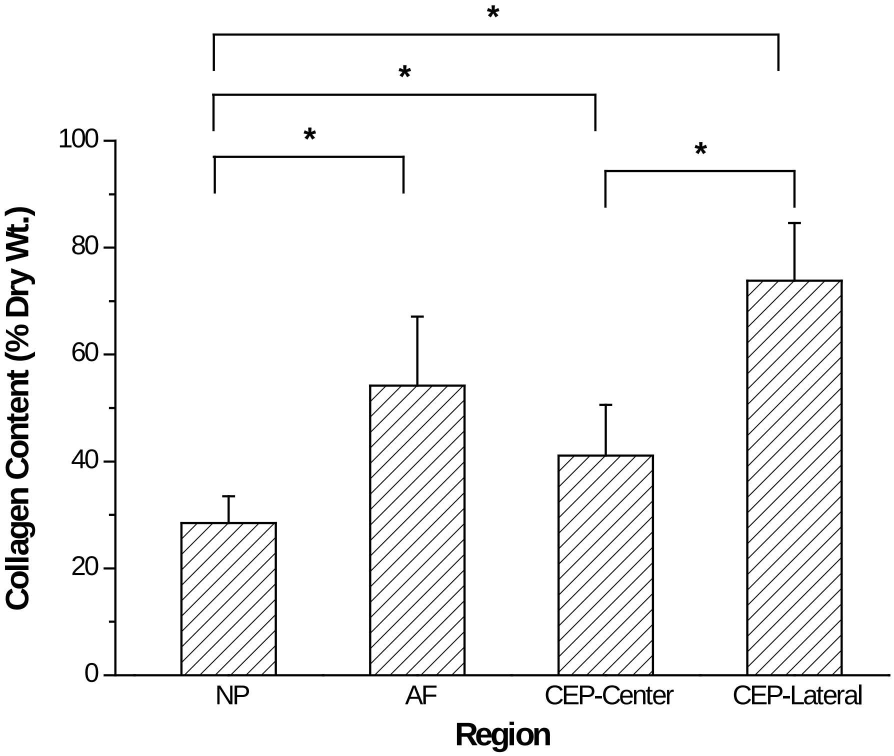
*
*
*
*
100
80
60
40
20
0
Collagen Content (% Dry Wt.)
NP
AF
CEP-Center
CEP-Lateral
Region

(b)

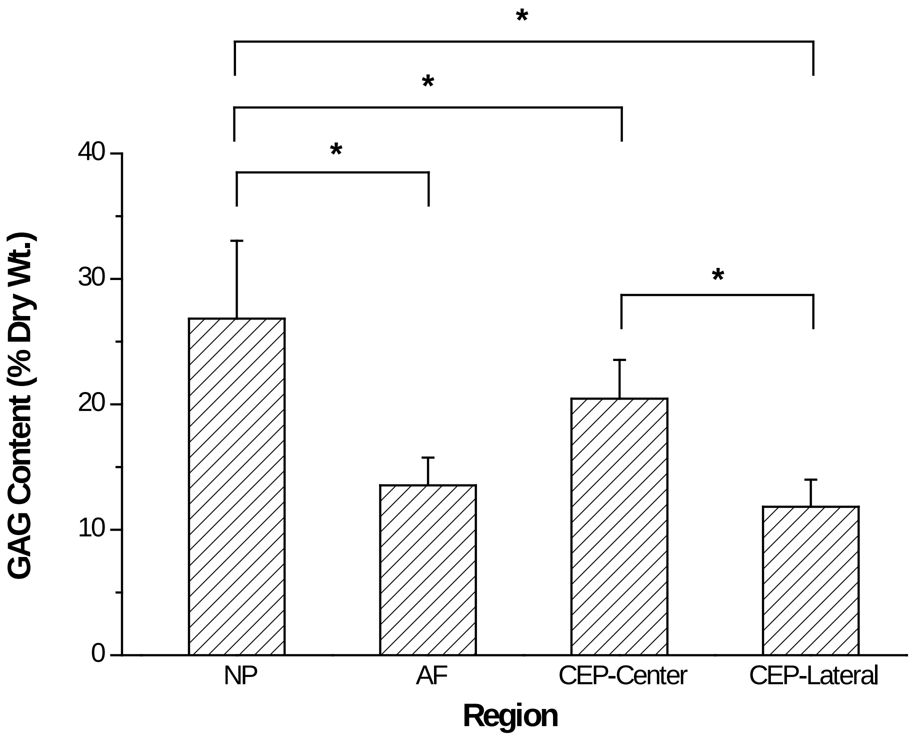

(c)

Figure 5.5 Results (mean ± SD) of biochemical assays measuring (a) water, (b) total collagen, and (c) total GAG content for each region of bovine IVD. Significant regional differences were detected for water, collagen, and GAG contents between the NP, AF, and CEP. Regional differences were also found for water, collagen, and GAG contents in the CEP between the center and lateral regions (*$p < 0.05$).

5.4 Discussion

The objective of this study was to investigate the viscoelastic properties of bovine cartilaginous endplate. The linear biphasic model (Mow, 1980) was used to curve fit the confined compression results with an average R^2 value of 0.989. It indicates that this method is reliable to characterize the viscoelastic properties of bovine cartilaginous endplate. In this study, the biphasic mechanical properties of bovine CEP in the center and lateral regions were in the same range of that in bovine NP and bovine, canine, and human AF, respectively (Figure 5.4a) [232-235]. A regional variation was found for the aggregate modulus between the center and lateral regions in the CEP, indicating that the lateral region of the bovine endplate is much stiffer and might share a greater portion of the load. The average hydraulic permeability of bovine CEP in this study is substantially different from the properties observed in the NP and AF (Figure 5.4b). No significant regional variation was found for the hydraulic permeability of bovine CEP. The average hydraulic permeability of bovine CEP is 0.13×10^{-15} m^4/Ns, which is 1/5 of that in bovine NP, 1/2 of that in bovine and human AF, and 1/5 of that in bovine articular cartilage [235, 236]. It indicates that, due to the small hydraulic permeability, the cartilaginous endplate blocks rapid solute convection and allows pressurization of the interstitial fluid in response to loading, which plays a significant role in the loading support and nutrient transport within the IVD.

The center region of bovine CEP had a lower aggregate modulus and swelling pressure than that in the lateral region, which may be due to the higher water content and lower collagen content in the center region of the CEP. This trend was in contrast to the

GAG content of the samples. These results are consistent with the inverse relationship with the water content and GAG content found in the literature [231]. Therefore, this observation supported the hypothesis that water content and collagen content are generally a stronger determinant of material properties than the GAG content. In this study, no significant correlation between hydraulic permeability and its biochemical composition was determined, which is in contrast with reported values in bovine NP and AF, and porcine AF [231, 237, 238]. Compared with that in the NP and AF regions, a smaller hydraulic permeability was also found in bovine CEP, which may be due to its unique collagenous networks and high collagen content as shown in our histological and biochemical studies (Figure 5.2 & 5.5b).

The average water, GAG, and collagen contents of bovine NP and AF measured in this study were consistent with that in the literature [224, 231]. The biochemical composition of bovine discs was found to be similar to the human disc [51, 83]. In the literature, it is also reported that the biphasic mechanical properties of bovine AF were in the same range of that in the human AF [233-235]. Therefore, the bovine disk could be considered as a good animal model for the study of biphasic mechanical properties of the cartilage endplate [224]. We used a 0.01 N contact force to make sure the loading probe was fully touching the testing sample, which was also justified by measuring the initial thickness of the CEP with a custom-designed current sensing digital micrometer (the initial thickness of CEP: ~0.60 mm under the micrometer, 0.60±0.08 in DMA). In this study, the confined swelling condition, instead of the free swelling condition, was chosen to represent the physiological water content in the CEP. The low strain rate and 3-4%

creep deformation were used to decrease the nonlinear response of the tissue and satisfy the linear biphasic theory.

The surface of the confined ring in the chamber for the confined compression test was designed to be smooth to reduce friction between the sample and the chamber. During the sample preparation, we found that the CEP may swell dramatically once immersed in the PBS or even thawed in the air under room temperature. Therefore, attention needed to be paid while we moved the sample into the confined chamber once the preparation of the sample was done under the microtome. There may have also been a small amount of GAG leakage from the tissue into PBS solution after the confined compression test. This may have introduced some error to the measured mechanical parameters, however this effect was expected to be small [231]. In our histological study, the thickness of the CEP was found to be close to 0.60 mm, which is consistent with that in the literature (the human CEP: 0.62±0.29 mm and thickness of baboon CEP: 0.81±0.26 mm) [57, 223]. Therefore, attention was taken while we prepared the CEP samples for mechanical and biochemical testing to maintain the initial thickness of the sample as close to 0.6 mm. This thickness also approached the lower limit of the sample thickness for the confined compression testing under the DMA.

5.5 Summary

In summary, the regional biomechanical and biochemical characterization of the bovine CEP was conducted to address the lack of data on bovine CEP tissue currently available in the literature. First, our gross observation, histological, biochemical, and mechanical characterizations confirmed that a layered structure of hyaline cartilage exists on top and bottom of the bovine disc. Second, due to the higher aggregate modulus and swelling pressure found in the lateral region of the CEP, the lateral bovine endplate was much stiffer than the central endplate and might share a greater portion of the load. This characteristic of the lateral CEP may be due to the lower water content and GAG content as well as the higher collagen content determined. This observation confirmed a previous hypothesis that the water content and collagen content are generally a stronger determinant of tissue material properties than GAG content [231]. Third, compared with the NP and AF, a smaller hydraulic permeability was found in the CEP, which could be due to its higher collagen content and unique collagenous network. In conclusion, our results indicated that the CEP could block rapid solute convection and allowed pressurization of the interstitial fluid in response to loading. The CEP also played a significant role in nutrient transport within the IVD. Calcification of the CEP with aging or degeneration could affect the nutrient supply to the disc cells and further alter disc homeostasis which may lead to disc degeneration.

CHAPTER 6 ENERGY METABOLISM OF HUMAN IVD CELLS

6.1 Introduction

As previously discussed in Chapters 4 and 5, the nutrients that disc cells require for maintaining disc health are supplied by blood vessels at the margins of the disc. There are two possible pathways for nutrient transport into the IVD, one route is through the CEP and the other is through the periannular [12]. While nutrients diffuse through the tissue, cells utilize these solutes for energy metabolism and matrix synthesis, and produce waste products that must be removed. The balance between the rate of nutrient transport through the matrix and the rate of energy metabolism by the disc cells determines the local nutrient environment, which needs to be maintained in a healthy IVD. As shown in the results of our numerical simulation in Chapter 4, IVD cells deep within the tissue are subjected to a low nutrient, high pH environment. Calcification of the cartilage endplate and injection of NP cells in cell based regeneration therapies would significantly impede the nutrient pathway resulting in development of a steeper solute gradient in the IVD under physiological loading conditions.

Glucose is an essential nutrient for energy production and serves as a building block for cellular growth. Lactate is a waste product of energy metabolism during glycolysis. Oxygen is also regarded as an important factor directly affecting cell biological activity [239]. Previous studies have found that matrix turnover and cell viability can be significantly affected by lack of oxygen and glucose [96]. In bovine and porcine IVD cells, the energy metabolism has also been found to be closely correlated with the local ECM environment. The rates at which disc cells metabolize glucose, consume oxygen, and produce ATP depend on the local acidity and concentration of nutrients [16, 24]. For porcine and bovine IVD cells, they obtain their energy primarily through glycolysis, even in the presence of oxygen. Nevertheless, IVD cells, as well as chondrocytes, require oxygen to function [16-18]. The pathways of oxygen utilization by chondrocytes and IVD cells remain obscure. Moreover, in some studies, low oxygen has been observed to diminish the rate of glycolysis, which is known as a negative Pasteur Effect. However, the opposite phenomena has been found in other studies. The rise of glycolysis rates during low oxygen is known as a positive Pasteur Effect [95, 96]. The reasons for these differences are also still unclear. Note that, it is also found that an acidic pH level significantly reduces the rate of glycolysis and the rate of oxygen uptake, and hence the production of ATP [95, 97]. Other factors such as growth factors, changes in the stresses in the surrounding matrix, and the osmotic environment have also been observed to influence the energy production rates [98].

To our knowledge, although there are some studies on articular cartilage chondrocytes and IVD cells in animal models [15-18], there is no study examining human disc cell energy metabolism until now. In this chapter, we will: a) characterize the OCR of human IVD cells at various glucose levels; and b) study rates of glucose consumption and lactate production of human IVD cells at various oxygen levels for each disc region. The measured kinetics of oxygen and glucose consumption in this study will provide fundamental understanding of the mechanisms underlying human IVD cell energy metabolism. Furthermore, it could provide realistic biological parameters for the multiphasic finite element model of the human IVD which was described in Chapters 2 and 3. In order to obtain a realistic prediction of the *in vivo* nutrient distribution inside the human IVD, energy metabolic rates of disc cells were taken into account in our theoretical model. Therefore measuring the energy metabolic rates of disc cells is crucial for precise theoretical analyses of nutrient transport in the human IVD under both physiological and pathological conditions.

6.2 Materials and Methods

6.2.1 Specimen Preparation

Human lumbar IVD tissues were obtained as to-be-discarded surgical waste from patients undergoing surgery for degenerative disc disease (total n=10 patients, aged 43–62 years old, degeneration Grade 3 or 4). Disc tissues were well rinsed and grossly separated into AF, NP, and CEP according to anatomic appearance. Samples were washed 3 times in 1% antibiotic/mycotic PBS, resuspended in 0.25% Trypsin-1mM EDTA for an hour, and then digested overnight at 37°C in an enzyme solution in high glucose (25 mmol/L) Dulbecco's Modified Eagle Medium (DMEM; Invitrogen Corp., Carlsbad, CA) supplemented with 10% fetal bovine serum (FBS; Invitrogen Corp.). For the AF tissue, the enzyme solution contained 1 mg/mL of collagenase (Worthington Biochemical Corp., Lakewood, NJ) and 0.6 mg/mL of protease (Sigma Chemical, St. Louis, MO). For NP tissues, it contained 0.5 mg/mL of collagenase and 0.3 mg/mL of protease. Digestions were strained through a 70um filter, washed, and re-suspended in DMEM supplemented with 10% FBS (HyClone Laboratories, Inc), 1% penicillin/streptomycin (Gibco Brl) and 25 ug/ mL ascorbic acid. Cells released from the three regions were then cultured in high glucose (25 mM) DMEM with 10% FBS. Cells for all experiments were obtained after two passages.

6.2.2 Oxygen Consumption Rate

Before the OCR measurements, cells from each region of the IVD were separated into 3 groups that were incubated in DMEM with glucose concentrations of 1, 5, and 25 mM for another 24 hours (media contained no FBS, pH 7.4 with NaOH). The oxygen consumption rates of the IVD cells were then measured in a stirred, water-jacketed chamber maintained at 37°C (Instech Laboratories, Plymouth Meeting, PA) (Figure 6.1a,b). First, cell suspensions (1 million cells per mL) were placed into the metabolism chambers. After the chamber was sealed, real time dissolved oxygen concentration in the medium was then recorded every 30 seconds by a fiber optic oxygen sensor (Ocean Optics, Dunedin, FL). O_2 tension is measured with a fiber optic needle probe coated with a captured fluorescent dye. A reading is generated from the intensity spectrum by calculating the area under the curve (centered around 600nm). Note that, at the end of the experiments, the glucose concentration and pH of the culture medium were measured. The decrease in glucose concentration and the change in pH were found to be minimal.

Experiments were stopped when oxygen concentrations fell below 0.1% (0.95 μmol/L). The equation defining the functional relationship between the oxygen consumption rate R and the oxygen concentration C is given by:

$$\frac{dC}{dt} = -Q = \frac{V_{max}}{K_m + C}\rho_{cell} \qquad (6.1)$$

Where Q is the rate of nutrient consumption (unit: nmoles/hr), ρ_{cell} is the cell density in the chamber (unit: million cell/ml). Integrating Equation 6.1, we can determine the oxygen concentration in the chamber over time:

$$t = \frac{K_m}{V_{max}\rho_{cell}} ln(\frac{C_0}{C}) + \frac{C_0 - C}{V_{max}\rho_{cell}} \qquad (6.2)$$

Where C_0 is the initial (t=0) oxygen concentration in the chamber. By fitting the recorded oxygen concentration data to Equation 6.2, the Michaelis-Menten kinetic coefficients V_{max} and K_m were obtained to establish the functional relationship between the oxygen consumption rate R and the oxygen concentration C.

Note that, the chamber for measuring oxygen concentration consists of two titanium 500 μL chambers with an acrylic sealing plug that creates a seal via the fluid column and hydrostatic pressure. The medium used in the metabolism chamber had been preheated to 37°C and stirred in air for 10 minutes to establish a constant initial dissolved oxygen concentration. Micro stir bars were set to a low speed setting to prevent stagnant fluid layer development and evenly distribute solutes in the chamber. Chambers were calibrated before experiments with a 0% O_2 standard solution (Oakton Instruments, IL) and fully oxygenated media. The concentration of dissolved oxygen in the culture medium at 37°C and atmospheric pressure was 200 μmol/L (or 6.4 mg/L).

6.2.3 Rates of Glucose Consumption and Lactate Production

Before the GCR and LPR experiments, cell suspensions in DMEM with a glucose concentration of 5 mM from each region of the IVD were placed into 24-well plates. They were then separated into 3 groups and incubated in the micro-incubators which had been preset at 1.5, 5, and 21% O_2 prior to plating of the IVD cell suspensions. Glucose and lactate concentrations were then measured using the YSI 2700 Select Biochemistry Analyzer after 4 and 18 hours. Glucose consumption and lactate production rates were calculated from the resulting concentration difference, cell densities, and time. At the end of the experiments, the explant pieces were fully digested and the cell viability was examined via trypan blue exclusion (greater than 90% viability).

Note that, glucose and lactate concentrations were measured with the YSI 2700 Select Biochemistry Analyzer (YSI Inc., OH). The instrument works by removing 15μL of the downstream solution and mixing it with a buffer solution in a test chamber. A probe on either side holds a membrane with immobilized oxidase enzymes specific to the substrate of interest which reacts with the solution in the chamber. The substrate diffuses through membrane, reacts with the enzymes and produces hydrogen peroxide. The hydrogen peroxide is oxidized at a platinum electrode to produce electrons which is measured as current. The electron flow is proportional to the hydrogen peroxide concentration and the initial substrate concentration. The instrument is capable of measuring glucose and lactate within the ranges of 0-9g/L and 0-2.67g/L.

6.2.4 Statistical Analysis

Regional differences between the rates of oxygen, glucose consumption, and lactate production of NP, AF, and CEP cells at different nutrient environments were examined using SPSS statistic software. Student’s t-test and One-way ANOVA (Tukey’s post hoc tests) were performed to determine if significant regional differences existed in

IVD cell energy metabolism due to a glucose effect on OCR and an oxygen effect on GCR. Statistical differences were reported at p-values < 0.05.

6.3 Results

6.3.1 Cell Morphology

Cells from the three regions can be morphologically distinguished under a transmission light microscope using both phase contrast and DIC techniques (Figure 6.2). The cells from the AF region are fibrochondrocyte-like cells, while the cells from CEP region are chondrocyte-like cells. The cells from NP region are uniformly circular and grow slower than cells from the CEP and AF.

6.3.2 Oxygen Consumption Rate

A typical curve-fit of the recorded oxygen concentration data with equation 6.2 is shown in Figure 6.1c. Good agreement was found between the experimental data and theoretical curve-fitting with $R^2=0.992\pm0.005$ (n=54), indicating that the relationship between the oxygen consumption rate and oxygen concentration can be well expressed using the Michaelis-Menten equation with the two parameters V_{max} and K_m. The V_{max} is the maximum oxygen consumption rate at high oxygen tension, and the K_m is the oxygen tension at which the oxygen consumption rate decreases to 50% of the V_{max} . V_{max} and K_m determined for NP, AF, and CEP cells are shown in Table 6.1. The averaged OCR of NP cells was higher than those of AF and CEP cells (Figure 6.5). However, no regional significant differences in K_m was found (Figure 6.4). No significant glucose effect was found in K_m, while significant effects due to the glucose level were found for $Vmax$ in all three regions (Figure 6.4). Furthermore, the cells cultured in the highest glucose medium (25 mM) exhibited an average 46.9% percent smaller *Vmax* than those cultured in the lowest glucose medium (1 mM), Table 6.1.

The relationship between the oxygen consumption rate and oxygen concentration in the three disc regions are plotted in Figure 6.5 using the Michaelis-Menten equation with averaged V_{max} and K_m. The oxygen consumption rate was relatively constant and fairly independent of oxygen tension until the oxygen tension fell below 5%. Below 5% oxygen, the rate fell in a highly concentration-dependent manner. Based on the Michaelis-Menten equation, the sensitivity of the oxygen consumption rate to the oxygen tension is solely controlled by the parameter K_m. The average K_m in all three regions are relatively small, 65.1 μmol/L in the AF, 69.9 μmol/L in the NP, and 61.7 μmol/L in the CEP. Note that, relative to the saturation oxygen condition (21% oxygen tension), 1% oxygen is equal to 9.5 μmol/L.

6.3.3 Rates of Glucose Consumption and Lactate Production

Glucose concentrations were measured at 4 and 18 hour time points and glucose consumption rates (GCR) were determined from the resulting concentration difference, cell densities, and time. The results showed the trend of increasing GCR with decreasing oxygen. Specifically, a significant oxygen effect on GCR was found when oxygen concentration decreased from 21% to 5%, as the average GCR was 106.7 nmol/million cells/hour for 21% oxygen level, 252.7 nmol/million cells/hour for 5% oxygen level in NP cells, and 74.0 nmol/million cells/hour for 21% oxygen level, 134.0 for 5% oxygen level in AF cells. It is also found that the average GCR of NP cells is 1.3 times higher than that of AF cells (Table 6.2).

Lactate production rates (LPR) were measured in a similar manner as the GCR. The results showed the trend of increasing LPR with decreasing oxygen. Specifically, a significant oxygen effect on LPR was found when the oxygen concentration decreased from 21% to 5%, as the average LPR was 69.0 nmol/million cells/hour for 21% oxygen level, 229.0 nmol/million cells/hour for 5% oxygen level in NP cells, and 1.2 nmol/million cells/hour for 21% oxygen level, 73.6 for 5% oxygen level in AF cells. It is also found that the average LPR of NP cells is 1.9 times higher than that of AF cells (Figure 6.7). The average ratio of lactate production to glucose consumption increased with a decrease of oxygen tension (Figure 6.7). It is also found that the average ratio of LPR and GCR of NP cells is 1.8 times higher than that of AF cells (Table 6.2).

Table 6.1 Vmax and Km of Human IVD Cells.

$C_{Glucose}$	AF		NP		CEP	
	V_{max}	K_m	V_{max}	K_m	V_{max}	K_m
mmol/L	nmol/10^6 cells/h	μmol/L	nmol/10^6 cells/h	μmol/L	nmol/10^6 cells/h	μmol/L
1	102.9±25.0	14.6±11.0	95.3±11.0	8.2±9.2	83.1±14.5	9.6±9.5
5	52.1±18.6	12.6±9.5	62.2±6.6	12.6±8.1	47.6±6.2	16.2±6.9
25	40.2±5.7	8.9±8.3	52.1±19.6	10.5±6.6	54.5±10.8	11.2±7.5
Average	65.1±16.4	12.0±9.6	69.9±12.4	10.4±8.0	61.7±10.5	12.3±8.0

* $C_{Glucose}$: glucose concentration in the medium.

Table 6.2 GCR and LPR of human NP and AF cells under different oxygen levels.

C_{oxygen}	NP			AF		
	GCR	LPR	Ratio	GCR	LPR	Ratio
mmol/L	nmol/10^6 cells/h	nmol/10^6 cells/h		nmol/10^6 cells/h	nmol/10^6 cells/h	
21	106.7±12.6	69.0±5.0	0.7	74.0±8.5	1.2±0.6	0.02
5	252.7±73.6	229.0±17.9	0.9	134.0±25.5	73.6±15.3	0.6
1.5	73.8±9.5	124.7±17.2	1.7	122.5±9.5	153.5±17.1	1.3
Average	144.4±31.9	140.9±13.4	1.1	110.2±14.5	76.1±11.0	0.6

* C_{Oxygen}: oxygen concentration in the medium. Ratio: LPR/GCR.

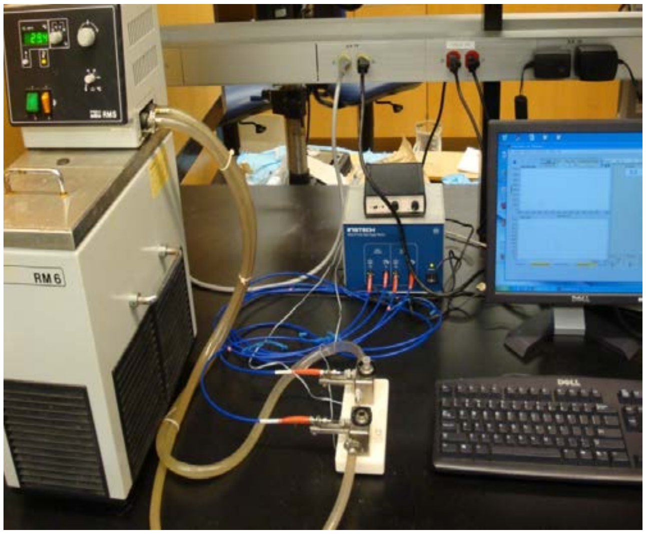

(a)

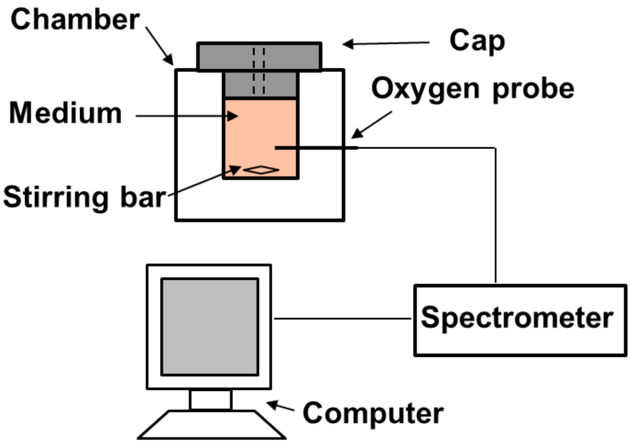
Chamber
Cap
Medium
Oxygen probe
Stirring bar
Spectrometer
Computer

(b)

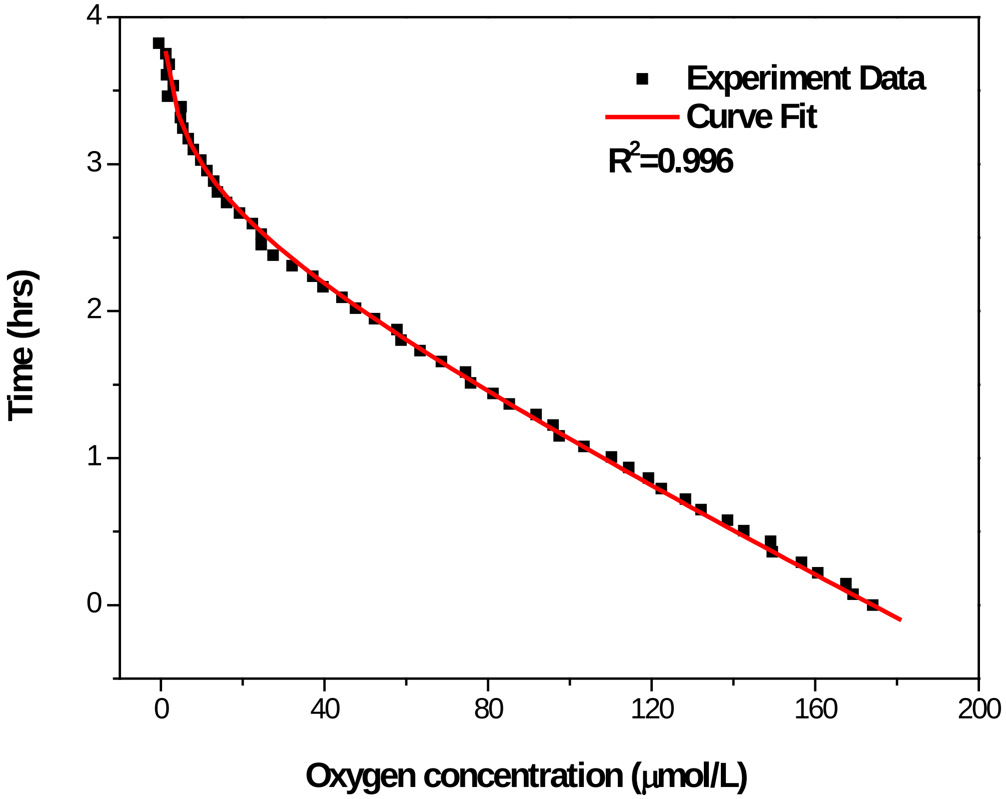

(c)

Figure 6.1 (a) OCR measurement system (water circulate system, plastic chamber, and fiber optic oxygen monitor). (b) Configuration for OCR chamber. (c) Typical OCR curve fitted to Michaelis-Menten model.

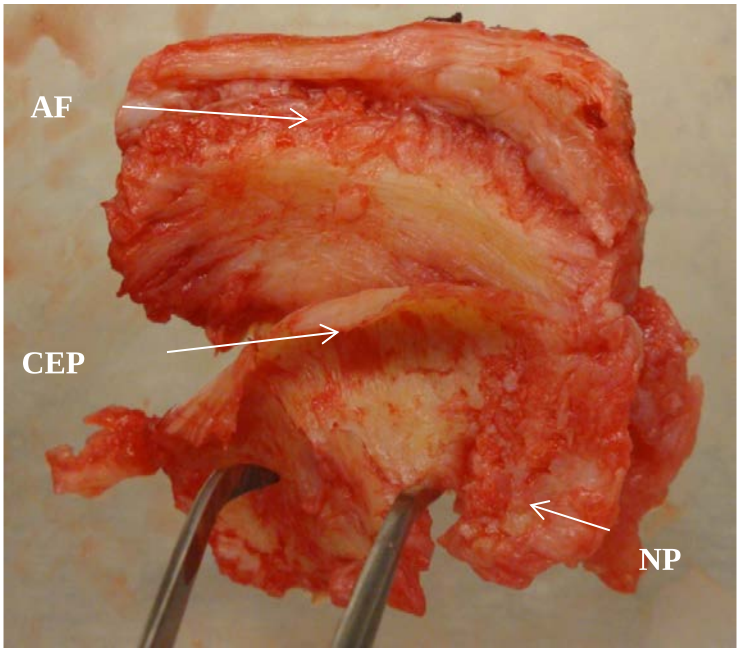

Figure 6.2 Top view of degenerated human IVD from lumbar spine. The disc tissue from the transition zone between AF and NP regions was discarded. The thin layer of CEP on the surface of the disc was carefully separated from the NP and AF according to anatomic appearance.

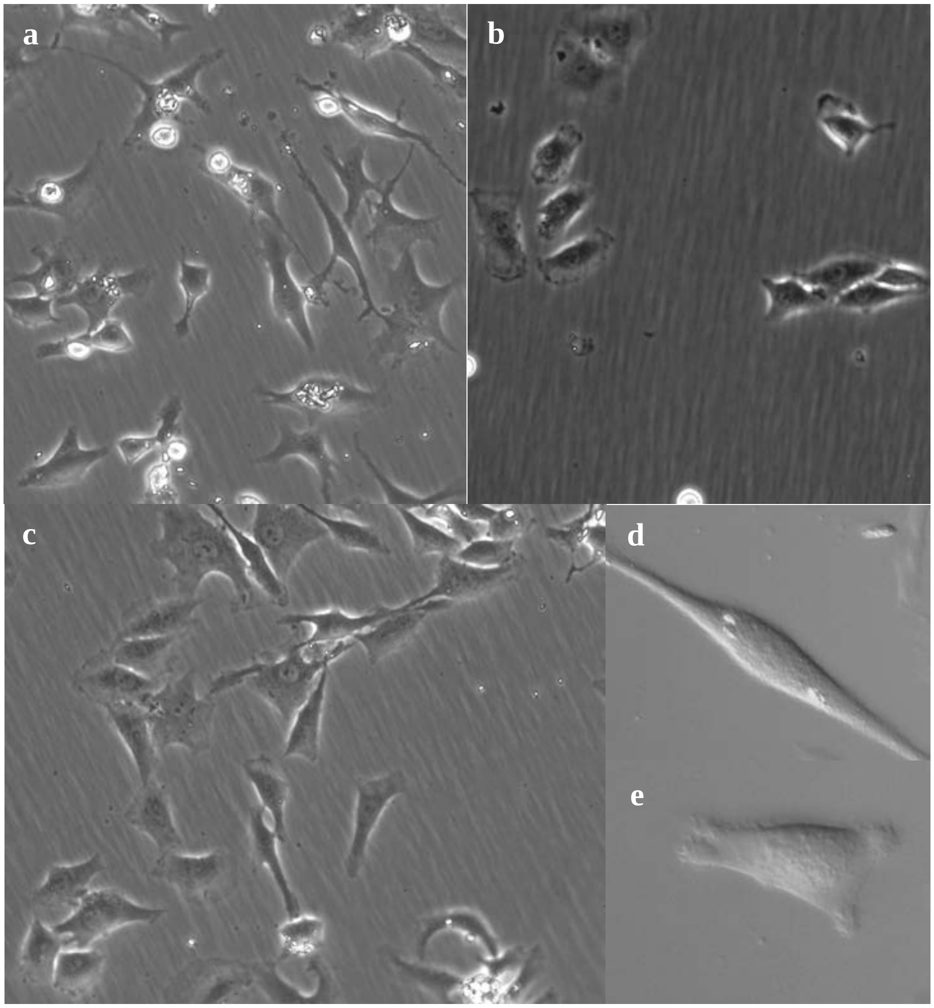

Figure 6.3 Light microscopic images of cultured human IVD cells from (a) AF, (b) NP, and (c) CEP regions. The cells from the AF region are fibrochondrocyte-like cells (d), while the cells from CEP region are chondrocyte-like cells (e). The cells from NP region are uniformly circular and grow slower than cells from the CEP and AF.

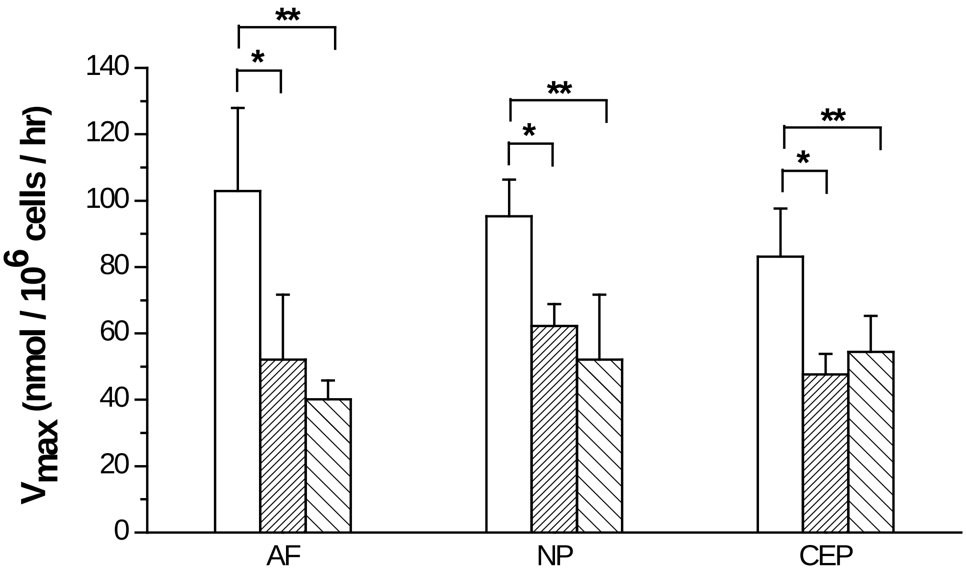

(a)

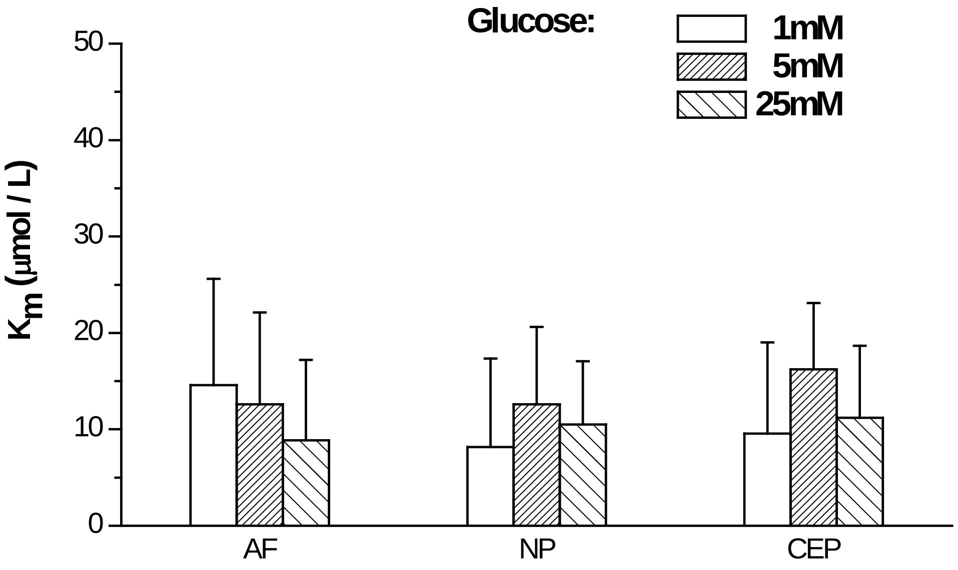

(b)

Figure 6.4 Comparison of (a) Vmax and (b) Km among AF, NP, and CEP cells cultured in the media with different glucose concentrations (n=6 for each group). Significant effects due to the glucose level were found for Vmax in all three regions while no significant differences were found in Km.

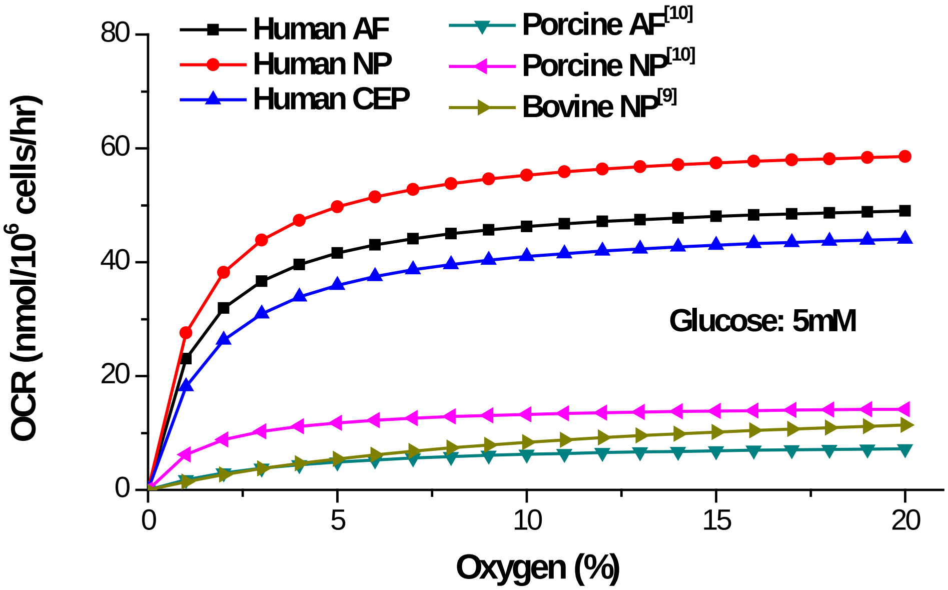

Figure 6.5 Comparison of OCR over the range of 0% to 20% oxygen tension determined in this study (human) and those found in the literature (animal). The averaged OCR of NP cells was significantly higher than those of AF and CEP cells. The OCR of human IVD cells measured in this study are about 5-6 times higher than porcine and bovine IVD cells.

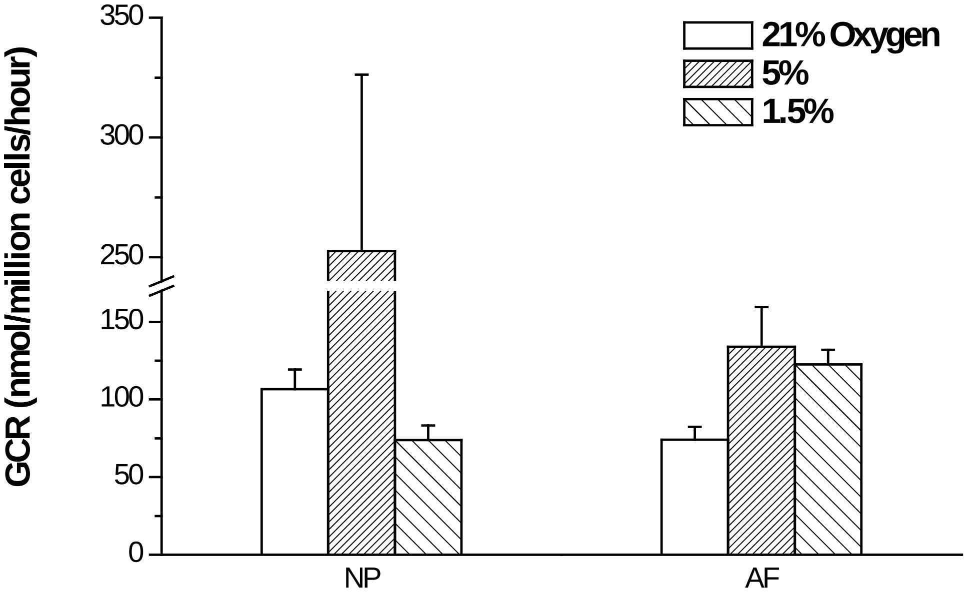
GCR (nmol/million cells/hour)
350
300
250
150
100
50
0
21% Oxygen
5%
1.5%
NP
AF

(a)

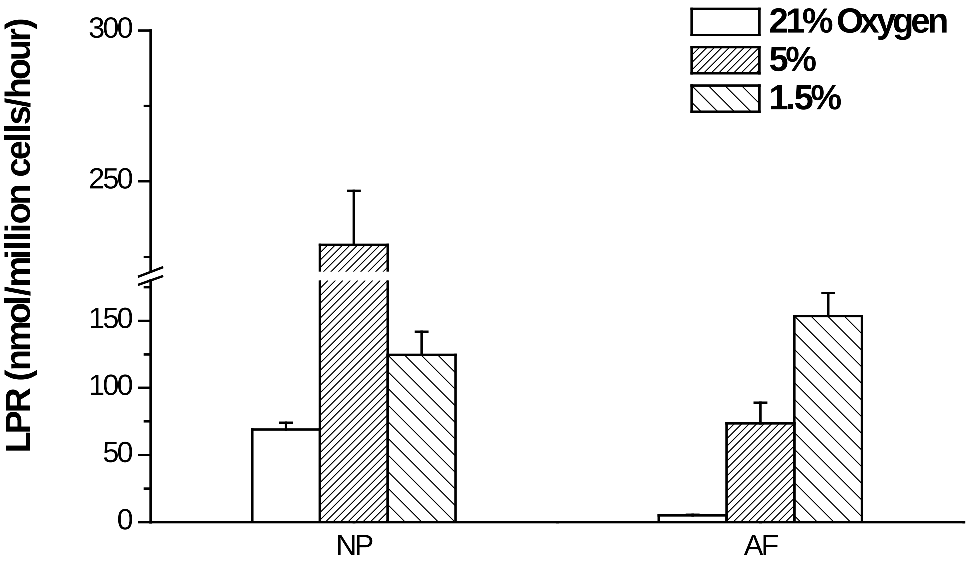

(b)

Figure 6.6 Effects of extracellular oxygen level on cell energy metabolism rates. (a) GCR varied by oxygen level from 21% to 1.5%. (b) LPR varied by oxygen level from 21% to 1.5%.

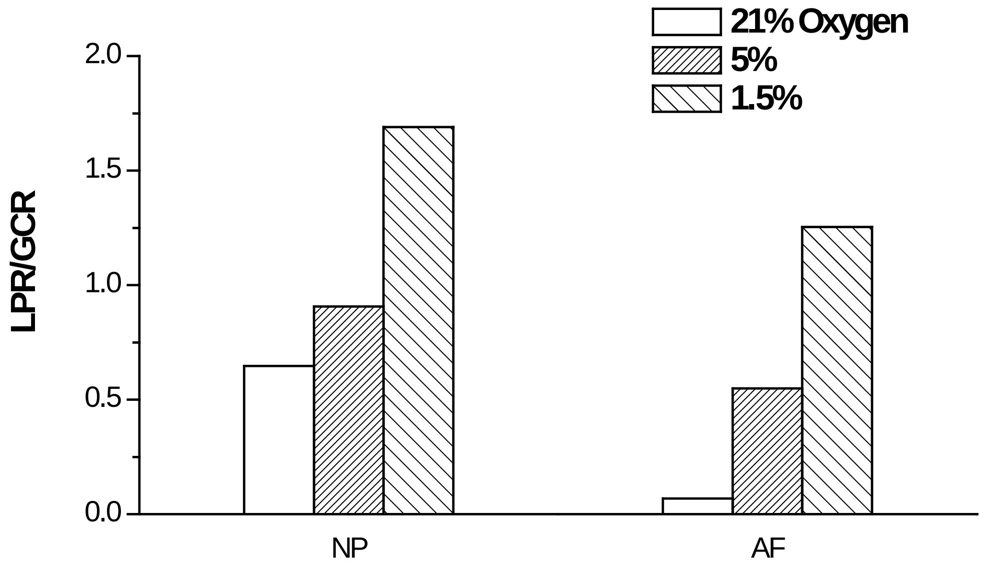

Figure 6.7 The ratio of glucose consumption to lactate production rates. It is found that the average ratio of lactate production rate to glucose consumption increased with a decrease of oxygen tension. During glycolysis, 1 glucose molecule results in the production of 2 lactate molecules produced. In this study, the ratio is closed to 2 at the 1.5% oxygen level.

6.4 Discussion

6.4.1 Oxygen Metabolism

In human IVD cells, it is found that the consumption of oxygen depends on the local oxygen tension. It is consistent with previous studies on articular chondrocytes [240, 241] and IVD cells [242, 243]. It was also determined that the nucleus pulposus (NP) cells have a higher oxygen consumption rate than the annulus fibrosus (AF) cells and cartilage endplate (CEP) cells. This is also consistent with previous studies on porcine and bovine IVDs [96, 243, 244]. The regional difference may due to the different cell types in the different regions as shown in our cell morphology studies. Generally, chondrocytes exhibit a higher rate of glycolysis in high glucose culture medium. Inhibition of cellular respiration due to the high rate of glycolysis, described as the Crabtree Effect, has been demonstrated in porcine AF cells, but not in porcine NP cells [2]. Low glucose did not stimulate oxygen consumption for either bovine AF or NP cells [1,3]. In this study, it is found that the Crabtree Effect existed in human IVD cells from all three regions.

The oxygen consumption rate (OCR) of the human IVD cells was measured in a sealed metabolism chamber. This approach has been used to investigate the effect of oxygen tension on the oxygen consumption rate of isolated articular chondrocytes [240] and porcine IVD cells [243]. Those studies have shown that the relationship between the oxygen consumption rate and oxygen tension can be modeled by the Michaelis-Menten equation with the two parameters V_{max} and K_m. Our results revealed that the kinetics of the oxygen consumption rate of human IVD cells can also be well expressed by this equation. Due to a small K_m, the oxygen consumption rate of the TMJ disc was relatively constant until the oxygen tension fell below 5%. Below 5% oxygen, the rate fell in a concentration-dependent manner. This finding is similar to the association between the oxygen consumption rate and oxygen concentration for articular chondrocytes [240, 241] and animal IVD cells [243].

Compared with vascularized tissues, such as the liver or kidney, the oxygen consumption rate of human IVD cells are ~5-10 times lower [245]. Previous studies showed that articular chondrocytes [239, 246] and animal IVD cells [247] obtain their energy primarily through the Embden-Meyerhof-Parnas (EMP) pathway (i.e., glycolysis), even in the presence of high oxygen tension [239, 246, 247]. Therefore, our study further supports that the oxygen consumption rate of human IVD cells is low due to its energy metabolism type.

Compared with porcine and bovine IVD cells, the OCR of human IVD cells measured in this study are about 5-6 times higher. The differences between human and animal IVD cells might be attributed to intrinsic differences between species, as well as degenerated samples and monolayer culture techniques adopted in this study. Recent studies have shown that the oxygen consumption of isolated articular chondrocytes increases with *in vitro* culture duration [248]. Oxygen consumption increased exponentially in that previous study within the first week and had doubled within the first 24 hours. The increase in oxygen consumption capacity could not be negated by culturing the cells under reduced oxygen atmospheres (2% and 5% O_2), thought to fall within the physiological range of oxygen tensions[249].

6.4.2 Glucose and Lactate Metabolism

In this study, it is found that the glucose consumption rate (GCR) in AF cells decreased when the oxygen level increased, which indicates a positive Pasteur Effect. The lactate production rate (LPR) also decreased at a higher oxygen level. It is found that the LPR/GCR ratio increased when the oxygen level decreased. During glycolysis, 1 glucose molecule results in the production of 2 lactate molecules. In this study, the ratio approaches 2 at the 1.5% oxygen level (Figure 6.7). Coupled with the results of a higher OCR at a higher oxygen level it suggests that human IVD cells utilize glycolytic pathways for energy needs at low oxygen and glucose levels and may switch towards oxidative phosphorylation at higher oxygen and glucose levels.

In this study, human NP cells showed a larger prevalence toward glycolytic pathways compared to human AF cells. Coupled with the higher OCR found in NP cells, it indicates that NP cells could be more active and ATP dependent under high oxygen and glucose conditions. As discussed in Chapter 2, different cell phenotypes were found in the NP and AF regions (NP cells: chondrocyte-like cells; AF cells: fibrochondrocyte-like cell), which may explain the difference in cellular energy metabolism found in this study. Compared with other cartilaginous tissues and animal IVD cells, the oxygen consumption rate, glucose consumption rate, and lactate production rate data suggest that the human cells have a higher metabolic rate. The significant difference in energy metabolism between cartilage types may be due to different cell phenotypes, degenerated samples, and monolayer culture techniques.

Due to the difficulty of measuring nutrient concentrations *in vivo*, mathematical models have been used to evaluate them in cartilaginous tissues. The results of these numerical calculations indicate that there is a steep gradient of glucose, lactate, and oxygen in normal cartilage and the concentration can be as low as 1% [240]. The normal adult human IVD is a large avascular structure [250-252], although some research has shown the presence of vasculature in young animals [253] and human discs [254], as well as degenerated human discs [255]. Considering the high cell density and long diffusion distance, a steep nutrient gradient could also be indicated in the human IVD. Such a steep nutrient gradient would make this tissue uniquely vulnerable to any pathological event which impedes nutrient supply, such as the calcification of the endplate. The rates of glucose/oxygen consumption and lactate production of human IVD cells in different extracellular nutrient conditions provided essential data for the mathematical model to precisely predict the nutrient environment inside the human IVD.

6.5 Summary

The positive Pasteur Effect and Crabtree Effect found in this study indicated that human IVD cells prefer a more prevalent glycolytic pathway for energy needs at harsh nutrient environmental conditions and may switch towards oxidative phosphorylation once the glucose and oxygen levels increase. Human NP cells showed a more prevalent glycolytic pathway and active energy metabolism under high oxygen and glucose conditions. Compared with other cartilaginous tissues and animal IVD cells, the metabolic activity of human IVD cells were also found to be more active due to the different cell phenotypes, degenerated samples, and monolayer culture techniques. Our studies also showed that human IVD cells are highly adaptable based on the nutrient concentrations supplied. In summary, this study outlined the energy metabolism properties of human IVD cells in different nutrient environments and provided more evidence to further analyze the driving nutrient metabolic mechanism in the human IVD. The results of this study also provided valuable data for theoretically predicting the nutrient transport and distribution inside the human IVD.

CHAPTER 7 A NOVEL MULTIPHASIC SINGLE CELL MODEL FOR CELL HOMEOSTASIS

7.1 Introduction

Previously, Boyle-van't Hoff and Kedem & Katchalsky equations [39] were used to simulate passive trans-membrane water and ion transport under various osmotic conditions. However, mechanical effects such as the cell membrane tension force or physicochemical factors such as the solute partition effect could not be considered. A more general mixture theory approach [40] was developed to incorporate these factors. Fundamental governing relationships for mechano-electrochemical transduction effects such as streaming potential, streaming current, diffusion (membrane) potential, and electro-osmosis could be deduced using this mixture theory. Specifically, stress, strain, and fluid velocity fields through a membrane during a one-dimensional steady diffusion process was simulated using this theory. Exchange of Na^+ and Ca^{2+} through the membrane were also analyzed [14]. Recently, several types of cell models were used to simulate passive cell volume response of articular chondrocytes and IVD cells by defining the cell as fluid-filled membrane or hydrogel/perfect osmometer like cytoplasm plus fluid filled membrane using the mixture theory [41, 42]. The cytoplasm and cell membrane were defined as a multiphasic mixture of solid phase (cytoskeleton), fluid phase (interstitial fluid), and sometimes a solute phase (ions).

Passive volumetric response of an isolated chondron under osmotic loading in a simple salt solution at equilibrium was also simulated by defining the chondrocytes as an ideal osmometer with triphasic PCM [42]. The chondron boundary is assumed to be permeable to both water and ions, while the chondrocyte membrane is selectively permeable to only water. For the case of a neo-Hookean PCM constitutive law, the model is used to conduct a parametric analysis of the cell and chondron deformation under hyper- and hypo-osmotic loading. In combination with osmotic loading experiments on isolated chondrons, model predictions will aid in determination of pericellular fixed charge density and its relative contribution to PCM mechanical properties [42]. Passive response of cells to osmotic loading with neutrally charged solutes was also simulated by defining chondrocytes as fluid filled membrane. The volume response to osmotic loading is found to be very sensitive to the magnitude of cell membrane tension and the partition coefficient of the solute in the cytoplasm, which controls the magnitude of cell volume recovery [41]. The theoretical predictions of this model are comparable with experimental results available in the literature [110, 155, 156]. This cell model could aid in determination of cell water content, hydraulic permeability, solute permeability and partition coefficient by well experiment design [37]. However, until now, there is no single cell model for trans-membrane ion transport coupled with water transport and membrane tension under cell homeostasis.

In this chapter, we developed a single cell model based on mixture theory. The IVD cell was defined as a fluid-filled membrane, while the membrane was considered as a multiphasic mixture which includes a solid phase (cytoskeleton), a fluid phase (interstitial fluid), and sometimes a solute phase (ions). Active ion transport processes, which impart momentum to solutes or solvent, were also incorporated in a novel supply term which appears in the conservation of linear momentum. In the mixture theory, which models the interactions of any number of fluid and solid constituents, a supply term appears in the conservation of linear momentum to describe momentum exchanges among the constituents. In past applications, this momentum supply was used to model frictional interactions only, thereby describing passive transport processes. However active transport processes which impart momentum to solutes or solvent, could also be expressed by this unique term. By projecting the equation of conservation of linear momentum along the normal to the membrane, a jump condition is formulated for the mechano-electrochemical potential of fluid constituents which is generally applicable to non-equilibrium processes involving active transport [157]. Therefore, this single cell model was capable of simulating the interactions of solid, fluid, and solutes (ions and neutral solutes) constituents in the cell membrane during the cell homeostasis. These models could help to track the behavior of the cells over time, allowing a better understanding of IVD cell behaviors as a result of various loading and environmental changes. These predictions may help researchers to understand IVD cell etiology related with human IVD degeneration and further develop possible therapeutic and regenerative treatments.

7.2 A Multiphasic Single Cell Model for Cell Homeostasis

In this section, the single cell model described is developed based on the multiphasic theory in chapter 3. The specific forms of the single cell model are deduced from the mass conservation, linear momentum conservation, the constitutive relationship based on thermo-dynamic laws. The cell was modeled as a fluid-filled multiphasic membrane. The multiphase of the cell membrane consists of incompressible and neutrally charged solid phase, interstitial water phase, ion phase with two monovalent species (e.g., Na$^+$ and Cl$^-$), and uncharged nutrient solute phase.

7.2.1 Passive Volume Response

For passive cell volume response, the governing equation for interaction between solid phase, water phase, ion phase and uncharged solute phase could be derived as follows.

7.2.1.1 Momentum Conservation

Solvent/Solutes: $-\rho^{\alpha}\nabla\mu^{\alpha} + \sum_{\beta} f_{\alpha\beta}\left(\mathbf{v}^{\beta} - \mathbf{v}^{\alpha}\right) = 0$, (7.1)

Water:

$$-\rho^{\mathbf{w}}\nabla\mu^{\mathbf{w}} + f_{ws}\left(\mathbf{v}^{\mathbf{s}} - \mathbf{v}^{\mathbf{w}}\right) + f_{w+}\left(\mathbf{v}^{+} - \mathbf{v}^{\mathbf{w}}\right) + f_{w-}\left(\mathbf{v}^{-} - \mathbf{v}^{\mathbf{w}}\right) + f_{wn}\left(\mathbf{v}^{\mathbf{n}} - \mathbf{v}^{\mathbf{w}}\right) = 0, \tag{7.1a}$$

Cation:

$$-\rho^{+}\nabla\tilde{\mu}^{+} + f_{+s}\left(\mathbf{v}^{\mathbf{s}} - \mathbf{v}^{+}\right) + f_{+w}\left(\mathbf{v}^{\mathbf{w}} - \mathbf{v}^{+}\right) + f_{+-}\left(\mathbf{v}^{-} - \mathbf{v}^{+}\right) + f_{+n}\left(\mathbf{v}^{\mathbf{n}} - \mathbf{v}^{+}\right) = 0, \tag{7.1b}$$

Anion:

$$-\rho^{-}\nabla\tilde{\mu}^{-} + f_{-s}\left(\mathbf{v}^{\mathbf{s}} - \mathbf{v}^{-}\right) + f_{-w}\left(\mathbf{v}^{\mathbf{w}} - \mathbf{v}^{-}\right) + f_{-+}\left(\mathbf{v}^{+} - \mathbf{v}^{-}\right) + f_{-n}\left(\mathbf{v}^{\mathbf{n}} - \mathbf{v}^{-}\right) = 0, \tag{7.1c}$$

Uncharged Solute:

$$-\rho^n \nabla \mu^n + f_{ns}\left(\mathbf{v}^{\mathbf{s}} - \mathbf{v}^{\mathbf{n}}\right) + f_{nw}\left(\mathbf{v}^{\mathbf{w}} - \mathbf{v}^{\mathbf{n}}\right) + f_{n+}\left(\mathbf{v}^{+} - \mathbf{v}^{\mathbf{n}}\right) + f_{n-}\left(\mathbf{v}^{-} - \mathbf{v}^{\mathbf{n}}\right) = 0, \tag{7.1d}$$

where μ^w and μ^n are the chemical potentials of water and uncharged nutrient solutes per unit mass, respectively; $\tilde{\mu}^+$ and $\tilde{\mu}^-$ are the electrochemical potentials of cation and anion per unit mass, respectively; $f_{\alpha\beta}$ is the friction coefficient per unit tissue volume between the inter-diffusing α and β components. Here the friction coefficients in each unit of the tissue are assumed to be symmetric, i.e. $f_{\alpha\beta} = f_{\beta\alpha}$.

The momentum equation 7.1 could also be written as:

$$\sum_{\beta}\left[f_{\alpha\beta} - d_{\alpha}\delta_{\alpha\beta}\right]\left(\mathbf{v}^{\beta} - \mathbf{v}^{\mathbf{s}}\right) = \rho^{\alpha}\nabla\mu^{\alpha} \tag{7.2}$$

where $\delta_{\alpha\beta}$ is the Kronecker delta and $d_{\alpha} = \sum_{\beta} f_{\alpha\beta}$. This equation could also be cast in matrix notation:

$$\left\{\rho^{\alpha}\nabla\mu^{\alpha}\right\} = [A]\left\{\mathbf{v}^{\alpha} - \mathbf{v}^{\mathbf{s}}\right\} \tag{7.3}$$

where [A] is 4*4 matrix, with components, $A_{\alpha\beta} = f_{\alpha\beta} - d_{\alpha}\delta_{\alpha\beta}$. $\left\{\rho^{\alpha}\nabla\mu^{\alpha}\right\}$ and $\left\{\mathbf{v}^{\alpha} - \mathbf{v}^{\mathbf{s}}\right\}$ are 4 column vectors. Solving for $\left\{\mathbf{v}^{\alpha} - \mathbf{v}^{\mathbf{s}}\right\}$ from equation 7.3, we can deduce the $[A]^{-1}$ as follows,

$$\left\{\mathbf{v}^{\alpha}-\mathbf{v}^{\mathbf{s}}\right\}=[A]^{-1}\left\{\rho^{\alpha}\nabla\mu^{\alpha}\right\}=[B]\left\{\rho^{\alpha}\nabla\mu^{\alpha}\right\}=\left\{\sum_{\beta}B_{\alpha\beta}\,\rho^{\beta}\nabla\,\mu^{\beta}\right\} \tag{7.4}$$

Water:

$$\begin{aligned}\mathbf{J}^{\mathbf{w}}&=\phi^{\mathbf{w}}\left(\mathbf{v}^{\mathbf{w}}-\mathbf{v}^{\mathbf{s}}\right)\\&=-\phi^{w}\left(\mathrm{B}_{11}\rho^{w}\nabla\mu^{w}+\mathrm{B}_{12}\rho^{+}\nabla\tilde{\mu}^{+}+\mathrm{B}_{13}\rho^{-}\nabla\tilde{\mu}^{-}+\mathrm{B}_{14}\rho^{n}\nabla\mu^{n}\right)\,,\end{aligned} \tag{7.4a}$$

Cation:

$$\begin{aligned}\mathbf{J}^{+}&=c^{+}\,\phi^{w}\left(\mathbf{v}^{+}-\mathbf{v}^{\mathbf{s}}\right)\\&=\mathrm{B}_{21}\,c^{+}\,\mathbf{J}^{\mathbf{w}}-c^{+}\,\phi^{w}(\,\mathrm{B}_{22}\rho^{+}\nabla\tilde{\mu}^{+}+\mathrm{B}_{23}\rho^{-}\nabla\tilde{\mu}^{-}+\mathrm{B}_{24}\rho^{n}\nabla\mu^{n}\,)\,,\end{aligned} \tag{7.4b}$$

Anion:

$$\begin{aligned}\mathbf{J}^{-}&=c^{-}\,\phi^{w}\left(\mathbf{v}^{-}-\mathbf{v}^{\mathbf{s}}\right)\\&=\mathrm{B}_{31}\,c^{-}\,\mathbf{J}^{\mathbf{w}}-c^{-}\,\phi^{w}(\,\mathrm{B}_{32}\rho^{+}\nabla\tilde{\mu}^{+}+\mathrm{B}_{33}\rho^{-}\nabla\tilde{\mu}^{-}+\mathrm{B}_{34}\rho^{n}\nabla\mu^{n}\,)\,,\end{aligned} \tag{7.4c}$$

Uncharged Solute:

$$\begin{aligned}\mathbf{J}^{\mathbf{n}}&=c^{n}\,\phi^{w}\left(\mathbf{v}^{\mathbf{n}}-\mathbf{v}^{\mathbf{s}}\right)\\&=\mathrm{B}_{41}\,c^{n}\,\mathbf{J}^{\mathbf{w}}-c^{n}\,\phi^{w}(\,\mathrm{B}_{42}\rho^{+}\nabla\tilde{\mu}^{+}+\mathrm{B}_{43}\rho^{-}\nabla\tilde{\mu}^{-}+\mathrm{B}_{44}\rho^{n}\nabla\mu^{n}\,)\,,\end{aligned} \tag{7.4d}$$

where B_{ij}'s are the material coefficients that are functions of the frictional coefficients $f_{\alpha\beta}$ between α and β constituents. The detailed expressions of B_{ij} are shown in Appendix D.

7.2.1.2 Constitutive Relation

Water: $\mu^w = \mu_0^w + \left[p - RT\phi(c^+ + c^- + c^o) + B_w \mathrm{tr}(\mathbf{E})\right] / \rho_T^w$, (7.5)

Cation: $\tilde{\mu}^+ = \mu_0^+ + \left(RT/M_+\right) ln\left(\frac{\gamma_+ c^+}{k_+ \, c_0^+}\right) + F_c \psi / M_+$, (7.6)

Anion: $\tilde{\mu}^- = \mu_0^- + \left(RT/M_-\right) ln\left(\frac{\gamma_- c^-}{k_- c_0^-}\right) - F_c \psi / M_-$, (7.7)

Uncharged solute: $\mu^n = \mu_0^n + \left(RT/M_n\right) ln\left(\frac{\gamma_n c^n}{k_n c_0^n}\right)$, (7.8)

Substitute equations (7.5-7.8) into equations (7.4),

$$\begin{aligned} \mathbf{J}^w &= -k\nabla p - kB_w \nabla tr(\mathbf{E}) \\ &\quad - RTk\left[(e^+ - \phi)\nabla c^+ + (e^- - \phi)\nabla c^- + (e^o - \phi)\nabla c^0\right] \\ &\quad - F_c k(e^+ c^+ - e^- c^-)\nabla \psi \ , \end{aligned} \tag{7.9}$$

$$\mathbf{J}^+ = H^+ c^+ \mathbf{J}^w - \phi^w D^+ \nabla c^+ - F_c \phi^w \omega^+ c^+ \nabla \psi \, , \tag{7.10}$$

$$\mathbf{J}^- = H^- c^- \mathbf{J}^w - \phi^w D^- \nabla c^- + F_c \phi^w \omega^- c^- \nabla \psi \, , \tag{7.11}$$

$$\mathbf{J}^\mathbf{n} = H^n c^n \, \mathbf{J}^\mathbf{w} - \phi^\mathbf{w} \, D^n \, \nabla c^n \, , \tag{7.12}$$

where k, e^{α}, H^{α}, D^{α}, and ω^{β} ($\alpha = +, -, n$; $\beta = +, -$) have the same physical meanings as shown in chapter 3. Their detailed expressions are shown in Appendix 4.

7.2.1.3 Boundary Conditions for Thin Cell Membrane

Based on the continuity of contraction, water, ion and uncharged solute chemical potentials in the interfaces (membrane-external solution; membrane-cytoplasm), boundary conditions could be expressed as follows,

1º Interface (Membrane-Cytoplasm)

Contraction Continuity: $-P^T + \sigma_{rr}^T = -P_i$ (7.13)

Interface Permeable to Water: $P^T - RT \sum_{\alpha \neq s,w} \phi c_T^{\alpha} = P_i - RT \sum_{\beta \neq s,w} \phi c_i^{\beta}$ (7.14)

Interface Permeable to ion: $\left(\frac{RT}{M^+}\right) ln \frac{\gamma_+ c_T^+}{k_+ c_0^+} + \frac{Z_+ F_c \Psi^T}{M^+} = \left(\frac{RT}{M^+}\right) ln \frac{\gamma_+ c_i^+}{k_i^+ c_0^+} + \frac{Z_+ F_c \Psi_i}{M^+}$ (7.15)

$$\left(\frac{RT}{M^-}\right) ln \frac{\gamma_- c_T^-}{k_- c_0^-} + \frac{Z_- F_c \Psi^T}{M^-} = \left(\frac{RT}{M^-}\right) ln \frac{\gamma_- c_i^-}{k_i^- c_0^-} + \frac{Z_- F_c \Psi_i}{M^-} \quad (7.16)$$

Interface Permeable to Uncharged Solutes: $\frac{c_T^n}{k^n} = \frac{c_i^n}{k_i^n}$ (7.17)

2^o Interface (Membrane-Extracellular)

Contraction Continuity: $-P^B + \sigma_{rr}^B = -P_e$ (7.18)

Interface Permeable to Water: $P^B - RT \sum_{\alpha \neq s,w} \phi c_B^\alpha = P_e - RT \sum_{\beta \neq s,w} \phi c_e^\beta$ (7.19)

Interface Permeable to ion: $\left(\frac{RT}{M^+}\right) ln \frac{\gamma_+ c_B^+}{k_+ c_0^+} + \frac{Z_+ F_c \Psi^B}{M^+} = \left(\frac{RT}{M^+}\right) ln \frac{\gamma_+ c_e^+}{k_e^+ c_0^+} + \frac{Z_+ F_c \Psi_e}{M^+}$ (7.20)

$$\left(\frac{RT}{M^-}\right) ln \frac{\gamma_- c_B^-}{k_- c_0^-} + \frac{Z_- F_c \Psi^B}{M^-} = \left(\frac{RT}{M^-}\right) ln \frac{\gamma_- c_e^-}{k_e^- c_0^-} + \frac{Z_- F_c \Psi_e}{M^-} \quad (7.21)$$

Interface Permeable to Uncharged Solutes: $\frac{c_B^n}{k^n} = \frac{c_e^n}{k_e^n}$ (7.22)

where p_i, p_e, p^T and p^B are the fluid pressure in the cell cytoplasm, external solution and inner and outer side of the cell membrane, respectively; c_i^α, c_e^α, c_T^α and c_B^α are the concentration in the cell cytoplasm, external solution and inner and outer side of the cell membrane, respectively; k_i^α, k_e^α and k^α are the partition coefficient of the solute in the cell cytoplasm, external solution and cell membrane, respectively.

Based on the conservation of linear momentum for the whole mixture of cell membrane,

$$-\nabla p + div\,\sigma^e + \mathbf{F_T} = 0 \quad (7.23)$$

where σ^e is the stress tensor in the membrane; F_T represents tension force in cell membrane.

For thin cell membrane with thickness of h, the pressure and concentration gradients during the trans-membrane transport process could be expressed by scalar form along the normal direction of membrane ($\nabla p \cdot \mathbf{n} \approx -\Delta p/h; \nabla c^{\alpha} \cdot \mathbf{n} \approx -\Delta c^{\alpha}/h$), therefore equation 7.23 could also be written as,

$$\Delta p - \sigma^{e}_{rr} - \frac{2T}{a} = 0 \tag{7.24}$$

where σ^{e}_{rr} is the normal effective stress in the radius direction; T is the surface tension in the membrane, a is the radius of cell sphere.

Thus from the boundary conditions, equation 7.13-7.22,

$$\Delta p = p^{T} - p^{B} = p_i - p_e + RT \sum_{\alpha \neq s,w} \phi \Delta c^{\alpha} - RT \sum_{\alpha \neq s,w} (c^{\alpha}_{i} - c^{\alpha}_{e}) \tag{7.25}$$

$$p_i - p_e = p^{T} - p^{B} - (\sigma^{T}_{rr} - \sigma^{B}_{rr}) = \Delta p - \Delta \sigma^{e}_{rr} = \frac{2T}{a} \tag{7.26}$$

$$\Delta c^{+} = c^{+}(ln\frac{\gamma_{+} c^{+}_{T}}{k_{+}\, c^{+}_{0}} - ln\frac{\gamma_{+} c^{+}_{B}}{k_{+}\, c^{+}_{0}}) = (ln\frac{\gamma_{+} c^{+}_{i}}{k^{+}_{i}\, c^{+}_{0}} - ln\frac{\gamma_{+} c^{+}_{e}}{k^{+}_{e}\, c^{+}_{0}} + \frac{Z_{+} F_{c}}{RT}(\Psi_{i} - \Psi_{e}) - \frac{Z_{+} F_{c}}{RT} \nabla \Psi) c^{+} \tag{7.27}$$

$$\Delta c^{-} = c^{-}(ln\frac{\gamma_{-} c^{-}_{T}}{k_{-}\, c^{-}_{0}} - ln\frac{\gamma_{-} c^{-}_{B}}{k_{-}\, c^{-}_{0}}) = (ln\frac{\gamma_{-} c^{-}_{i}}{k^{-}_{i}\, c^{-}_{0}} - ln\frac{\gamma_{-} c^{-}_{e}}{k^{-}_{e}\, c^{-}_{0}} + \frac{Z_{-} F_{c}}{RT}(\Psi_{i} - \Psi_{e}) - \frac{Z_{-} F_{c}}{RT} \nabla \Psi) c^{-} \tag{7.28}$$

$$\varDelta c^n = c_T^n - c_B^n = k^n\left(\frac{c_i^n}{k_i^n} - \frac{c_e^n}{k_e^n}\right) \tag{7.29}$$

7.2.1.4 Governing Equations

Substitute equation (7.25-7.29) in to the momentum equations (7.9-7.12) under thin membrane conditions,

$$J^w = \frac{k}{h}\left[\frac{2T}{a} - RT\sum_{\alpha\neq s,w}(c_i^\alpha - c_e^\alpha)\right] + RT\frac{k}{h}\sum_{\alpha\neq s,w,n}\left[e^\alpha \bar{c}^\alpha\left(ln\frac{c_i^\alpha}{k_i^\alpha} - c_e^\alpha\right) + \frac{e^\alpha Z_\alpha F_c}{M_\alpha}(\varPsi_i - \varPsi_e)\right]$$

$$+\frac{RTk\, e^n k^n}{h}\left(\frac{c_i^n}{k_i^n} - c_e^n\right) \tag{7.30}$$

$$J^+ = H^+ \bar{c}^+ J^w + \frac{\phi^w D^+ \bar{c}^+}{h}\left[ln\frac{c_i^+}{k_i^+} - ln\, c_e^+ + \frac{Z_+ F_c}{RT}(\varPsi_i - \varPsi_e)\right], \tag{7.31}$$

$$J^- = H^- \bar{c}^- J^w + \frac{\phi^w D^- \bar{c}^-}{h}\left[ln\frac{c_i^-}{k_i^-} - ln\, c_e^- + \frac{Z_- F_c}{RT}(\varPsi_i - \varPsi_e)\right], \tag{7.32}$$

$$J^n = H^n c^n J^w + \frac{\phi^w D^n k^n}{h}\left(\frac{c_i^n}{k_i^n} - c_e^n\right), \tag{7.33}$$

As for the whole cell, by integrating the continuity of mass equation of mixture and solutes, the governing equation for cell volume change and solute transport yields,

$$\frac{dv}{dt} = -AJ^{w} = -AL_{p}\left\{\left[\frac{2T}{a} - RT\sum_{\alpha\neq s,w}(c_i^{\alpha} - c_e^{\alpha})\right]\right.$$

$$\left. + RT\sum_{\alpha\neq s,w,n}\left[e^{\alpha}\overline{c}^{\alpha}(ln\frac{c_i^{\alpha}}{k_i^{\alpha}} - c_e^{\alpha}) + \frac{e^{\alpha}Z_{\alpha}F_{c}}{M_{\alpha}}(\Psi_i - \Psi_e)\right] + AL_{p}RT\,e^{n}k^{n}(\frac{c_i^{n}}{k_i^{n}} - c_e^{n})\right\} \qquad (7.34)$$

$$\frac{d\,n_i^{+}}{dt} = -AJ^{+} = -A\left\{H^{+}\overline{c}^{+}J^{w} + p^{+}\overline{c}^{+}\left[ln\frac{c_i^{+}}{k_i^{+}} - ln\,c_e^{+} + \frac{Z_{+}F_{c}}{RT}(\Psi_i - \Psi_e)\right]\right\}, \qquad (7.35)$$

$$\frac{d\,n_i^{-}}{dt} = -AJ^{-} = -A\left\{H^{-}\overline{c}^{-}J^{w} + p^{-}\overline{c}^{-}\left[ln\frac{c_i^{-}}{k_i^{-}} - ln\,c_e^{-} + \frac{Z_{-}F_{c}}{RT}(\Psi_i - \Psi_e)\right]\right\}, \qquad (7.36)$$

$$\frac{d\,n_i^{n}}{dt} = -AJ^{n} = -A\left[H^{n}\overline{c}^{n}J^{w} + p^{n}(\frac{c_i^{n}}{k_i^{n}} - c_e^{n})\right], \qquad (7.37)$$

where $L_p = \frac{k}{h}$; $p^{\alpha} = \frac{\phi^{w}D^{\alpha}k^{\alpha}}{h}$; $\overline{c}^{\alpha} = \frac{1}{2}(\frac{c_i^{\alpha}}{k_i^{\alpha}} + c_e^{\alpha})$; $c_i^{\alpha} = \frac{n_i^{\alpha}}{\varphi_i^{w}v}$; v is the volume of the cell; A is the area of the cell; L_p is the membrane hydraulic conductivity; n_i^{α} is the number of the moles of solute inside the cell; p^{α} is the solute membrane permeability; $\overline{c}^{\alpha}$ is the average concentration between cytoplasm and external solutions (α = cation, anion and uncharged solute).

7.2.1.5 Convergence Validation

For non-permeable solute only, governing equation of cell volume change (equation 7.34) could be written as equation 7.38 which is the form of classical Boy-van't

Hoff equation [39]. Note that surface tension in the cell membrane T was assumed as zero.

$$\frac{dv}{dt} = -AJ^{w} = -AL_{p}RT \sum_{\alpha \neq s,w} (c_{i}^{\alpha} - c_{e}^{\alpha}) \tag{7.38}$$

As for permeable solute, governing equation of cell volume change (equation 7.34) could also be written as equation 7.39 which is the form of classical Kedem & Katchalsky equations [39]. Note that $H^{n} = 1 - \sigma^{p}$ and $k_{i}^{n} = 1$ were assumed and σ^{p} is the Staverman's reflection coefficient.

$$\frac{dv}{dt} = -AJ^{w} = -AL_{p}RT \sum_{\alpha \neq s,w} (c_{i}^{\alpha} - c_{e}^{\alpha}) \tag{7.39}$$

$$\frac{d\,n_{i}^{n}}{dt} = -AJ^{n} = -A\left[\frac{1}{2}(1-\sigma^{p})(c_{i}^{n} + c_{e}^{n})J^{w} + p^{n}(c_{i}^{n} - c_{e}^{n})\right] \tag{7.40}$$

7.2.2 Active Volume Regulation

The governing equations described in previous sections were for passive trans-membrane water, ion and solute transport. However, in biological membranes, there are also two types of active transport. Primary active transport is mediated by the ion pumps in the membrane which are driven by a supply of energy generated from the hydrolysis of adenosine triphosphate (ATP). Secondary active transport is mediated by the trans-membrane carriers driven by the free energy from electrochemical gradient of solutes. In previous classical field of non-equilibrium thermodynamics, active transport process through ion pumps, exchangers or transporters were incorporated into the force-flux pairs by adding an additional driving force in the flux [48, 256]. In contrast, the driving force for the ATP-driven active transport is considered as the affinity of the phosphorylation reaction [47, 257]. In this section, we will provide a novel approach by using the framework of the mixture theory as shown in chapter 3. A novel supply term was incorporated in conservation equations of linear momentum developed based on the mixture theory. In past applications, this momentum supply was used to model frictional interactions only, thereby describing passive transport processes. However, active transport processes which impart momentum to solutes or solvent could also be expressed by this unique term.

7.2.2.1 Momentum Conservation

Solvent/Solutes: $-\rho^{\alpha}\nabla\mu^{\alpha}+\sum_{\beta} f_{\alpha\beta}\left(\mathbf{v}^{\beta}-\mathbf{v}^{\alpha}\right)+\mathbf{p}_{\mathbf{a}}^{\boldsymbol{\alpha}}=0$ (7.41)

Water:

$$-\rho^{\mathbf{w}}\nabla\mu^{\mathbf{w}}+f_{ws}\left(\mathbf{v}^{\mathbf{s}}-\mathbf{v}^{\mathbf{w}}\right)+f_{w+}\left(\mathbf{v}^{+}-\mathbf{v}^{\mathbf{w}}\right)+f_{w-}\left(\mathbf{v}^{-}-\mathbf{v}^{\mathbf{w}}\right)+f_{wn}\left(\mathbf{v}^{\mathbf{n}}-\mathbf{v}^{\mathbf{w}}\right)+\mathbf{p}_{\mathbf{a}}^{\mathbf{w}}=0, \quad (7.41a)$$

Cation:

$$-\rho^{+}\nabla\tilde{\mu}^{+}+f_{+s}\left(\mathbf{v}^{\mathbf{s}}-\mathbf{v}^{+}\right)+f_{+w}\left(\mathbf{v}^{\mathbf{w}}-\mathbf{v}^{+}\right)+f_{+-}\left(\mathbf{v}^{-}-\mathbf{v}^{+}\right)+f_{+n}\left(\mathbf{v}^{\mathbf{n}}-\mathbf{v}^{+}\right)+\mathbf{p}_{\mathbf{a}}^{+}=0, \quad (7.41b)$$

Anion:

$$-\rho^{-}\nabla\tilde{\mu}^{-} + f_{-s}\left(\mathbf{v}^{\mathbf{s}} - \mathbf{v}^{-}\right) + f_{-w}\left(\mathbf{v}^{\mathbf{w}} - \mathbf{v}^{-}\right) + f_{-+}\left(\mathbf{v}^{+} - \mathbf{v}^{-}\right) + f_{-n}\left(\mathbf{v}^{\mathbf{n}} - \mathbf{v}^{-}\right) + \mathbf{p}_{\mathbf{a}}^{-} = 0\,, \qquad (7.41c)$$

Uncharged Solute:

$$-\rho^{n}\,\nabla\,\mu^{n} + f_{ns}\left(\mathbf{v}^{\mathbf{s}} - \mathbf{v}^{\mathbf{n}}\right) + f_{nw}\left(\mathbf{v}^{\mathbf{w}} - \mathbf{v}^{\mathbf{n}}\right) + f_{n+}\left(\mathbf{v}^{+} - \mathbf{v}^{\mathbf{n}}\right) + f_{n-}\left(\mathbf{v}^{-} - \mathbf{v}^{\mathbf{n}}\right) + \mathbf{p}_{\mathbf{a}}^{\mathbf{n}} = 0\,, \qquad (7.41d)$$

where p_a^{α} (α: water, cation, anion and uncharged solute) represents active transport term. Therefore, based on equations 7.4 and constitutive relation (equation 7.5-7.8), the trans-membrane flux are shown as follows,

$$\begin{aligned} \mathbf{J}^{\mathbf{w}} &= -k\nabla\, p - kB_w\,\nabla\, tr(E) \\ &\quad - RTk\left[(e^{+}-\varphi)\nabla\, c^{+} + (e^{-}-\varphi)\nabla\, c^{-} + (e^{o}-\varphi)\nabla\, c^{0} + \sum_{\alpha} S^{\alpha}\right] \\ &\quad - F_c k(e^{+}c^{+} - e^{-}c^{-})\nabla\,\psi + \hat{W}\,, \end{aligned} \qquad (7.42)$$

$$\mathbf{J}^{+} = H^{+}c^{+}\,\mathbf{J}^{\mathbf{w}} - \varphi^{w}D^{+}(\nabla\, c^{+} + S^{+}) - F_c\varphi^{w}\omega^{+}c^{+}\,\nabla\,\psi\,, \qquad (7.43)$$

$$\mathbf{J}^{-} = H^{-}c^{-}\,\mathbf{J}^{\mathbf{w}} - \varphi^{w}D^{-}(\nabla\, c^{-} + S^{-}) + F_c\varphi^{w}\omega^{-}c^{-}\,\nabla\,\psi\,, \qquad (7.44)$$

$$\mathbf{J}^{\mathbf{n}} = H^{n}c^{n}\,\mathbf{J}^{\mathbf{w}} - \phi^{\mathbf{w}}\,D^{n}\,\nabla\, c^{n}\,, \qquad (7.45)$$

where $\hat{W} = \frac{\rho_T^{w}}{\rho^{w}}\,p_a^{w}$; $S^{\alpha} = \frac{1}{RT}\frac{M^{\alpha}}{\rho^{\alpha}}\,p_a^{\alpha}$. Based on boundary conditions between the interfaces (equation 7.13-7.22), the governing equations are shown as,

$$J^w = \frac{k}{h}\left[\frac{2T}{a} - RT\sum_{\alpha\neq s,w}(c_i^\alpha - c_e^\alpha)\right] + RT\frac{k}{h}\sum_{\alpha\neq s,w,n}\left[e^\alpha \bar{c}^\alpha\left(ln\frac{c_i^\alpha}{k_i^\alpha} - c_e^\alpha + S^\alpha\right) + \frac{e^\alpha Z_\alpha F_c}{M_\alpha}(\Psi_i - \Psi_e)\right]$$

$$+\frac{RTk\,e^n k^n}{h}\left(\frac{c_i^n}{k_i^n} - c_e^n\right) + \frac{k}{h}\hat{W} \tag{7.46}$$

$$J^+ = H^+ \bar{c}^+ J^w + \frac{\varphi^w D^+ \bar{c}^+}{h}\left[ln\frac{c_i^+}{k_i^+} - ln\, c_e^+ + S^+ + \frac{Z_+ F_c}{RT}(\Psi_i - \Psi_e)\right], \tag{7.47}$$

$$J^- = H^- \bar{c}^- J^w + \frac{\varphi^w D^- \bar{c}^-}{h}\left[ln\frac{c_i^-}{k_i^-} - ln\, c_e^- + S^- + \frac{Z_- F_c}{RT}(\Psi_i - \Psi_e)\right], \tag{7.48}$$

$$J^n = H^n c^n J^w + \frac{\varphi^w D^n k^n}{h}\left(\frac{c_i^n}{k_i^n} - c_e^n\right), \tag{7.49}$$

7.2.2.2 Governing Equation

As for the whole cell, assuming Na$^+$, K$^+$ and Cl$^-$ pass through the cell membrane due to passive and active transport mechanism, the governing equations for cell volume change and solute transport yields,

Cell Volume:

$$\frac{dv}{dt} = -AJ^w = -AL_p\left\{\left[\frac{2T}{a} - RT\sum_{\alpha\neq s,w}(c_i^\alpha - c_e^\alpha) + S^\alpha\right]\right.$$

$$\left. + RT\sum_{\alpha\neq s,w,n}\left[e^\alpha \bar{c}^\alpha\left(ln\frac{c_i^\alpha}{k_i^\alpha} - c_e^\alpha\right) + \frac{e^\alpha Z_\alpha F_c}{M_\alpha}(\Psi_i - \Psi_e)\right] + RT\,e^n k^n\left(\frac{c_i^n}{k_i^n} - c_e^n\right) + \hat{W}\right\} \tag{7.50}$$

Na$^+$ Flux:

$$\frac{d\,n_i^{Na^+}}{dt} = -AJ^{Na^+} = -A\left\{H^{Na^+}\,\bar{c}^{Na^+}\,J^w + \tilde{p}^{Na^+}\left[ln\frac{c_i^{Na^+}}{k_i^{Na^+}} - ln\,c_e^{Na^+} + S^{Na^+} + \frac{Z_{Na^+}F_c}{RT}(\Psi_i - \Psi_e)\right]\right\}$$

, (7.51)

K$^+$ Flux:

$$\frac{d\,n_i^{k^+}}{dt} = -A\,J^{k^+} = -A\left\{H^{k^+}\,\bar{c}^{k^+}\,J^w + \tilde{p}^{K^+}\left[ln\frac{c_i^{k^+}}{k_i^{k^+}} - ln\,c_e^{k^+} + S^{k^+} + \frac{Z_{k^+}F_c}{RT}(\Psi_i - \Psi_e)\right]\right\},$$

(7.52)

Cl$^-$ Flux:

$$\frac{d\,n_i^{cl^-}}{dt} = -A\,J^{cl^-} = -A\left\{H^{cl^-}\,\bar{c}^{cl^-}\,J^w + \tilde{p}^{cl^-}\left[ln\frac{c_i^{cl^-}}{k_i^{cl^-}} - ln\,c_e^{cl^-} + S^{cl^-} + \frac{Z_{cl^-}F_c}{RT}(\Psi_i - \Psi_e)\right]\right\}$$

(7.53)

Uncharged Solute:

$$\frac{d\,n_i^n}{dt} = -A\,J^n = -A\left[H^n\,\bar{c}^n\,J^w + p^n\left(\frac{c_i^n}{k_i^n} - c_e^n\right)\right], \qquad (7.54)$$

where $\tilde{p}^{\alpha} = p^{\alpha}\,\bar{C}^{\alpha}$; $\hat{W}$ represents measure of the momentum supply of solvent from trans-membrane transport with the unit of force / area or energy / volume. $\hat{W}$ represents measure of the momentum supply of solute from trans-membrane transport with dimensionless quantity [46].

7.3 Summary

IVD cells were defined as a fluid-filled membrane using mixture theory [41, 42]. Ion transport through the membrane was incorporated in the model by adding the (electro)chemical potential for ions. The active ion transport process, which imparts momentum to solutes or solvent, was also incorporated in a supply term as appears in the conservation of linear momentum. The interactions between solid, fluid and solute constituents (ions and neutral solutes) in cell membranes could be simulated during homeostasis. The trans-membrane transport parameters (i.e hydraulic permeability and ion conductance) could be measured from the single cell experiments in Chapter 8. This novel single cell model could help to further illuminate the mechanisms underline IVD cell homeostasis. In addition, effects of fixed negative charge (impermeable intracellular macromolecular anions) and active transport on IVD cell homeostasis could be further analyzed.

CHAPTER 8 QUANTITATIVE CHARACTERIZATION OF WATER AND ION TRANSPORT DURING IVD CELL HOMEOSTASIS

8.1 Introduction

Changes in both the extracellular osmotic and nutrient environment may affect cell homeostasis (volume regulation) [29-31]. In turn, the triggering of cell homeostasis mechanisms due to environmental perturbations also serves as a signal for cell behaviors such as cell proliferation and matrix synthesis [28]. In previous studies, passive cell volume response under osmotic loading was measured in articular chondrocytes (AC) at room temperature while the phenomenon of active cell volume regulation was detected in AC at body temperature [28, 32-36]. Furthermore, extracellular matrix (ECM), cartilage degeneration, cell culture conditions, and osmotic loading types were all found to have a significant effect on AC volume response under osmotic loading [28, 33, 101, 106].

Previous studies also showed that interactions between the cytoskeleton, water and ion flux through cell membrane could be the key mechanism by which cells regulate homeostasis and adapt to their rigorous environment. Different mechanisms including Ca^{2+} dependent Na^{+}-K^{+}-Cl^{-} cotransporter (NKCC), actin in the cell cytoskeleton, and Na^{+}-H^{+} exchanger have been proposed for regulating AC and IVD cell homeostasis [34-36, 38, 137], however, until now, the mechanism for cell homeostasis has remained unclear. Moreover, compared to AC, different cell volume response phenomena have been observed in porcine IVD cells which may indicate different cell volume regulation mechanisms [35, 38].

In order to further illuminate the mechanism of IVD cell homeostasis, a cell model which quantitatively simulates the interactions between different phases in the cell environment (cytoskeleton, water and ions) during homeostasis was developed in Chapter 7. In order to determine the parameters for this numerical model, quantitative characterization of the water and ion transport properties during cell homeostasis was needed. Recently, the cell membrane properties of hydraulic permeability and the diffusivity of neutral solutes at room temperature were quantitatively calculated by curve fitting real time cell volume data using Boyle-van't Hoff and Kedem & Katchalsky equations in bovine articular chondrocytes [37]. To our knowledge, until now, there exists no quantitative data for these water and ion transport properties (hydraulic permeability and ion conductance) in IVD cells.

In this chapter, we will quantitatively characterize the water and ion transport through the porcine IVD cell membrane during cell homeostasis (steady state) at room temperature. The hydraulic permeability and ion conductance of porcine IVD cells will be determined from passive cell volume response experiments and whole cell patch clamp experiments. Furthermore, the Resting Membrane Potential (RMP) of porcine AC and IVD cells will be measured. As a hallmark of membrane ion transport, RMP is the potential at which a cell's membrane must be held to produce no net ion flow across the membrane. The RMP of a cell is a manifestation of the differential intra and extracellular ionic concentrations as well as the individual ionic conductances (Goldman equation).

8.2 Materials and Methods

8.2.1 Cell Culture and Sample Preparation

IVD cells were obtained from lumbar spine of acute (3 month old) male pigs weighing ~35-45 kg. During the dissection, annulus fibrosis (AF) and nucleus pulposus (NP) regions in IVDs were carefully separated, minced, and washed 3 times with phosphate buffered saline (PBS) containing 1% antibiotic (A/A). The tissue was then incubated in 0.25% trypsin for 1 hour and then digested by enzyme solutions (AF: 1.0 mg collagenase type II and 0.6 mg protease type I; NP: 0.1 mg collagenase type II) in the high glucose (25 mmol/L) Dulbecco's modified Eagle's medium (DMEM) supplemented with 10% fetal bovine serum (FBS) and 1% antibiotic-antimycotic (A/A) for 20 hours at 37^{o}C. The cells were then filtered using a 70 μm cell strainer and washed 3 times with PBS and plated at a concentration of $3x10^{5}$/mL in culture flasks containing full media composed of DMEM, 10% FBS, 1% PBS, 1% nonessential amino acids, 25 μg/mL ascorbic acid, 1% HEPES and pH 7.4 with NaOH. All the primary cells were used for experiments in one week. No significant phenotype change was found during this period based on studies in literature [37].

8.2.2 Cell Volume Response

Before the cell volume response experiment, cells were suspended and cultured in perfusion chambers (RC 22, Warner Instruments, CT) for 30-60 minutes with isotonic solution (140 NaCl, 5 KCl, 1 $MgCl_2$, 2 $CaCl_2$, 10 HEPES; unit: mM; pH 7.4 with NaOH; ~295 mOsm). In order to reduce the effect of fluid flow on cell attachment and cell volume response, one thin layer of gauze micro-grid was fixed on the bottom of the chamber by a rhombic metal ring. The hypertonic solution (isotonic solution + 300 mM sucrose; ~605 mOsm) was then perfused through the chamber with the speed of 1 mL/min by two syringe pumps (Genie Touch, Kent Scientific, CT). Note that the capacity of the chamber was 200 µL. It took ~10 s to exchange all the solution and reach osmotic equilibrium within the chamber based on our preliminary fluid perfusion tests of the chamber. The osmolality of the solutions was measured using a vapor pressure osmometer (model 5520, Wescor Inc., Utah). All the volume response experiments were conducted at room temperature. The volume response was imaged using a differential interference contrast (DIC) objective lens (40x, 0.75 NA) with an inverted microscope (Axio Observer A1, Carl Zeiss Inc., NY) and recorded using a Zeiss MRm camera with Axiosuite time lapse software (Zeiss). The time lapse data was analyzed by fitting the volume time rate of change to the modified van't Hoff equation to extract the membrane hydraulic permeability and intracellular fraction of osmotically active water, see equation 8.1-8.3 [37].

$$\frac{dv}{dt} = A L_p RT \sum_{\alpha} (c_i^{\alpha} - c_e^{\alpha}) \tag{8.1}$$

$$c_i^{\alpha} = \frac{n_i^{\alpha}}{\phi_i^{w} v} \tag{8.2}$$

$$\phi_i^{w} = 1 - (1 - \phi_{\mathrm{i}r}^{w}) \frac{v_r}{v} \tag{8.3}$$

where ν is the cell volume; A is the volume dependent cell surface area (A=3ν/a where a represents cell radius); L_p is the membrane hydraulic permeability; R and T are universal gas constant and absolute temperature, respectively. c_i^r and c_e^r are the internal and extracellular osmolyte concentrations; n_i^α is the number of moles of the internal osmolytes; ϕ_i^w and ϕ_{ir}^w are the real time and initial volume fraction of osmotically active water in the cytoplasm, respectively.

A Matlab program was developed to dynamically detect the cell edge and calculate the cell volume (Figure 8b) from the acquired time lapse DIC images. During the cell edge detection process, following general steps were used: we extracted an annular region of interest around the cell boundary in the source image; enhanced the edge and detected it with a custom-written radial edge detection algorithm which mapped an annular region from the radial direction into a two dimension matrix of pixel intensity and detected the cell edge using dynamic programming which calculated the location of the maximum of the second derivative of the best fit sigmoid curve of the pixel intensity as the edge. We then calculated the radius, area and volume of the cell (see figure 8.2) [112]. Furthermore, Calcein-AM was used to stain for cell viability. Additionally, confocal microscopy was used to capture real time fluorescent cell images in different focal planes under hypotonic and hypertonic conditions. The 3D image reconstruction technique within Amira (commercial software) was also used to build real time 3D cell images and calculate the cell volume change. These results were used to validate our assumption of spherical cell shape for circular cells and the resulting of 2D cell volume approximation method which is much faster and more convenient than other methods.

8.2.3 Membrane Current and Resting Membrane Potential Recordings

Before the patch clamp experiments, the cells were rinsed and plated onto coverslips at a density of $3x10^4$ cells/mL and incubated for an additional 12 hours prior to measurement. Under voltage clamp, trans-membrane current was measured in the whole cell configuration of the patch-clamp technique using an Axopatch 200B amplifier (Molecular Devices, Sunnyvale, CA) and data were acquired through the Digidata 1440A digital board (Axon Instruments) with a digital current sampling frequency of 10 kHz. Patch electrodes were fabricated from borosilicate capillary glass with filament (1B150F-4, World Precision Instruments) and pulled using a Brown Flaming type pipette puller (model P-97, Sutter Company) to a tip resistance of 5-12 MΩ when filled with the internal solution composed of (mM): 115 K-aspartate, 25 KCl, 1 $MgCl_2$, 1 $CaCl_2$, 10 EGTA, 10 HEPES and titrated to pH 7.2 with KOH (290 mOsm). The standard external solution was composed of (mM): 140 NaCl, 5 KCl, 1 $MgCl_2$, 2 $CaCl_{2,}$ 10 HEPES and titrated to pH 7.4 with NaOH (295 mOsm). Ag-Cl ground and inner pipette electrodes were used and seal resistance before patch rupture ranged from 5 to 10 GΩ.

The generation of voltage-clamp protocols and data acquisition was controlled by pCLAMP software (version 10.2; Axon Instruments, Inc., Foster City, CA). The protocol of stimulation consisted of 200ms square voltage pulses of -120 to + 70 mV in steps of 10 from a holding potential of -60 mV (Figure 8.3). By using this protocol with step function, trans-membrane currents were recorded for 200 ms during each voltage steps.

Resting membrane potential (RMP) was calculated from the current and voltage curve for each cell. Furthermore, a voltage ramp protocol from -120 to + 70 mV in 250 ms was used to stimulate the cell and measure the current and voltage relation and RMP in a separate manner. By using current mode, the RMP was also estimated as the voltage at which zero current flows, in order to validate the RMP measurements from step and ramp protocols under voltage clamp mode.

8.2.4 Capacitance Measurements

After establishing a whole cell patch, membrane capacitance was measured from a +10 mV test pulse from a holding potential of -60mV by the CLAMPEX module of the pCLAMP software. The membrane capacitance was calculated on-line by fitting a time constant to the decaying phase of the capacitive current. The time constant was divided by the membrane resistance, which was subsequently calculated from the difference between the steady state current and the basal current (before the onset of the pulse) divided by the pulse amplitude. The holding currents were not digitally subtracted by the P/N method as to avoid the introduction of artifacts into the measurement of the resting membrane potential.

8.2.5 Statistical Analysis

Regional differences between the capacitance, RMP and conductance of AC, AF and NP cells were examined using SPSS statistic software. Student's t-test and One-way ANOVA (Tukey's post hoc tests) were performed to determine if significant difference between AC and IVD cells and regional differences in IVD cells existed in trans-membrane transport properties. Statistical differences were reported at p-values < 0.05.

8.3 Results

No active volume response was found in porcine AF cells under hypertonic loading conditions at room temperature as shown in Figure 8.4b. Therefore based on the modified Boyle-van't Hoff equation, a typical curve-fit of the recorded cell volume response during hypertonic condition was shown (Figure 8.1b). Good agreement was found between the experimental data and theoretical curve-fitting with $R^2=0.910\pm0.007$, indicating that the relationship between the cell volume change and the osmotic environment can be well expressed using the Boyle-van't Hoff equation with the two parameters L_p and ϕ_{ir}^w, where L_p is the membrane hydraulic permeability and ϕ_{ir}^w represents the initial fraction of osmotically active water in the cell cytoplasm. As shown in the figure 8.4c, the hydraulic permeability L_p for porcine AF cells is $1.37\pm0.42*10^{-14}$ $m^3/N.s$ and ϕ_{ir}^w is 0.42±0.09.

In our patch clamp experiments, it was found that the cell membrane capacitances for primary cultured AC, AF, and NP cells were 10.2±0.9 pF, 11.6±0.8 pF and 19.1±2.6 pF, respectively (Figure 8.5), with a significant difference existing between three cell types. NP cell showed the largest capacitance compared to AF cells and AC. Our results also indicated that the resting membrane potential for AC, AF, and NP cells were -38.1± 1.9, -39.1±1.6 and -26.1±3.9 mV, respectively (Figure 8.6). The RMP in NP was found to be significantly smaller than that in AC and AF. The current voltage relationship for

AC, AF and NP cells in Figure 8.7, all demonstrated outwardly rectifying currents activated when the clamp voltages through the cell membrane were larger than RMPs in all three cell types. Furthermore, significant difference in the magnitudes of these outward currents were observed between AC, AF and NP cells with the NP cells possessing the smallest and the AF cells the largest with the AC in between the two. In contrast, small currents were found when the clamp voltages through the cell membrane were lower than the relative RMPs (Figure 8.7). In addition, both inward and outward currents possessed a linear region of conductance as shown in Figure 8.7. Therefore by fitting the linear [258], the conductances (L_1 and L_2) were estimated for all three cell types as shown in Table 8.1. We found that the conductances for AF, NP and AC cells were very close when the clamp voltages through the membrane were lower than the RMPs. In contrast, when the clamp voltages were larger than the RMPs, significant higher conductance was found in AF (672.6±161.0 pS/pF) compared to that in NP (63.7±19.5 pS/pF) and AC (390.4±71.2 pS/pF).

Table 8.1 RMPs, capacitances and conductances of AC, AF, and NP cells. Statistical differences were found for the RMPs, capacitances, and conductances (Lp2 and Lp2-Lp1) between the AC, AF, and NP cells, while no statistical difference was found for conductance (Lp1) for these three cell types. Note that Lp1 represented the ion conductance when the voltage applied on the cell was lower than the relative RMP, while Lp2 represented the ion conductance when the voltage applied on the cell was higher than the RMP.

	RMP	Capacitance	Lp1	Lp2	Lp2-Lp1
Unit	*mV*	*pF*	*pS/pF*	*pS/pF*	*pS/pF*
AC	-38.1±1.9	10.2±0.8	56.3±10.2	390.4±71.2	330.6±51.6
AF	-39.1±1.6	11.6±0.8	50.2±9.7	672.6±161.0	618.9±116.4
NP	-26.1±3.9	19.1±2.6	52.1±10.1	63.7±19.5	12.7±9.5

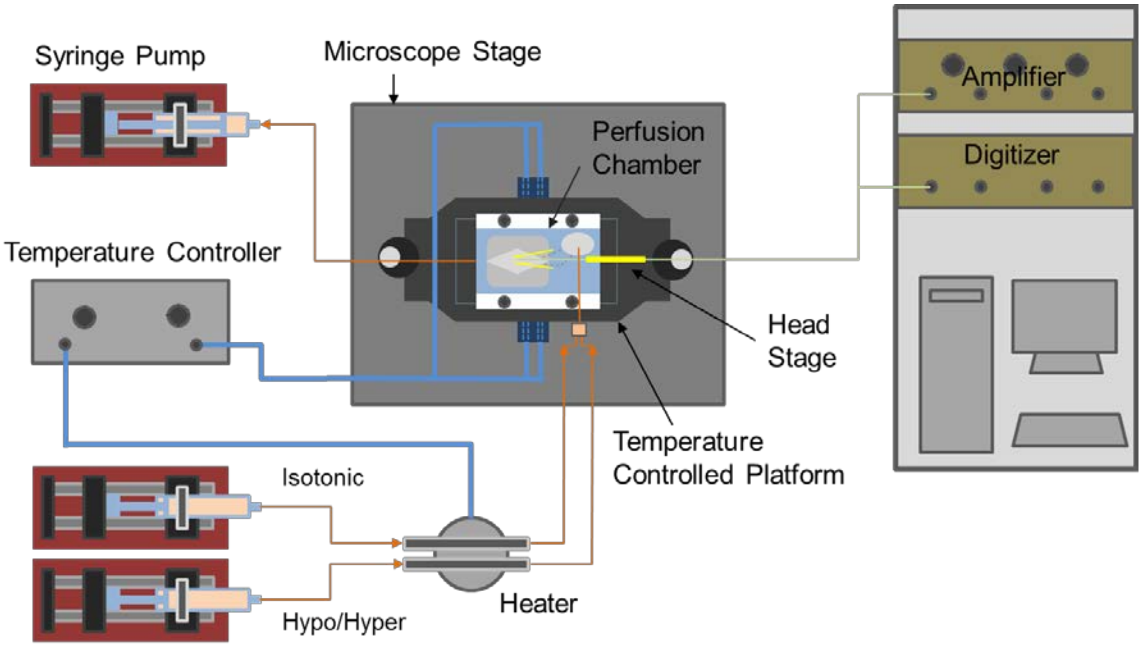

Figure 8.1 Schematic for perfusion and patch clamp system. The isotonic and hypertonic solutions were perfused through the chamber mounted in the microscope stage with the speed of 1 mL/min by syringe pumps. A temperature control system was added to the perfusion system which was capable of well control the temperature of the solution in the chamber as well as that of the infusion solutions. Meanwhile, a patch clamp system (pipette electrodes, head stage, amplifier, and digitizer et al.) was developed to measure the current / voltage through the cell membrane.

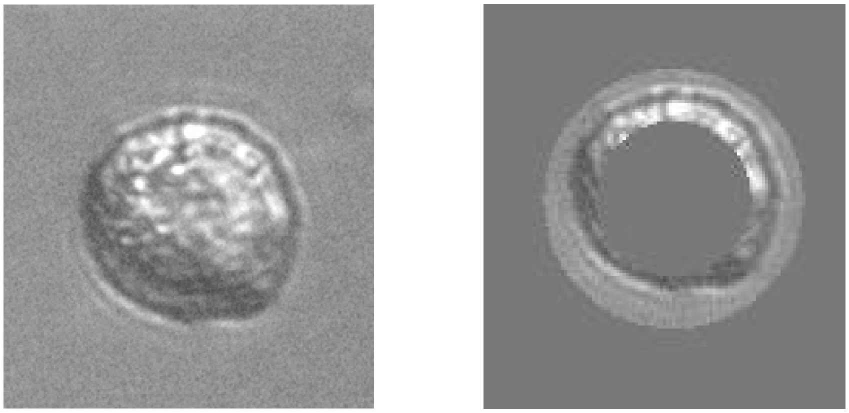

(a)

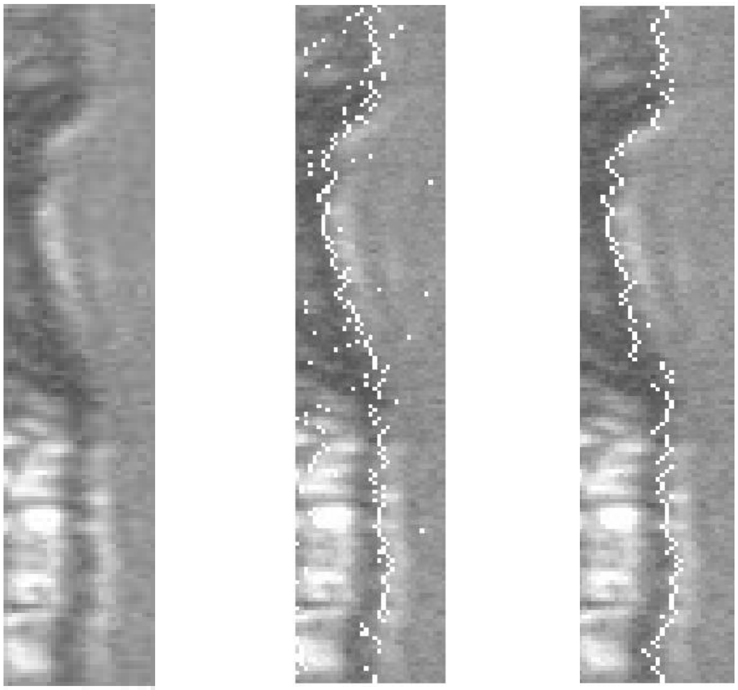

(b)

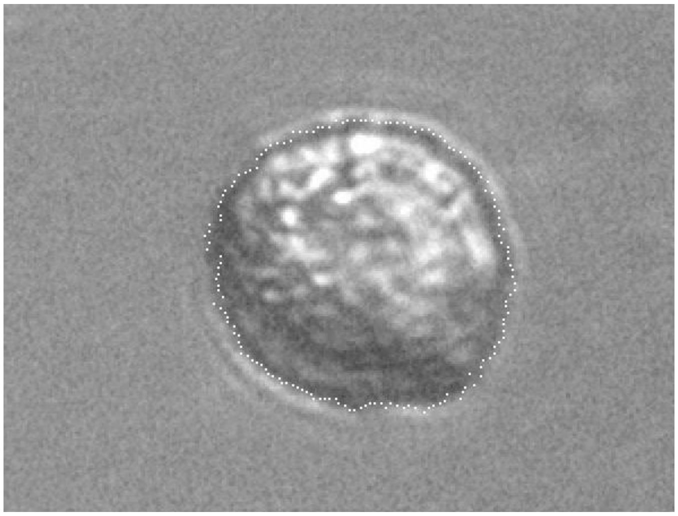

(c)

Figure 8.2 Schematic of cell edge detection from DIC image. (a) The wide annular region that was created encloses the cell boundary. Two points were manually picked from the top and bottom of the cell boundary to briefly calculate the radius of the cell (r^*_{cell}). The radius for the internal and external circles were set as 0.85 r^*_{cell} and 1.15 r^*_{cell}, respectively. (b) The pixels of the annular region which were mapped into a two dimension matrix. By using dynamic mapping technique [112], more accurate results of cell edge detection were achieved as shown in the rectangular region in the right. (c) Results of dynamic mapping for cell edge detection and superimposition on the original image.

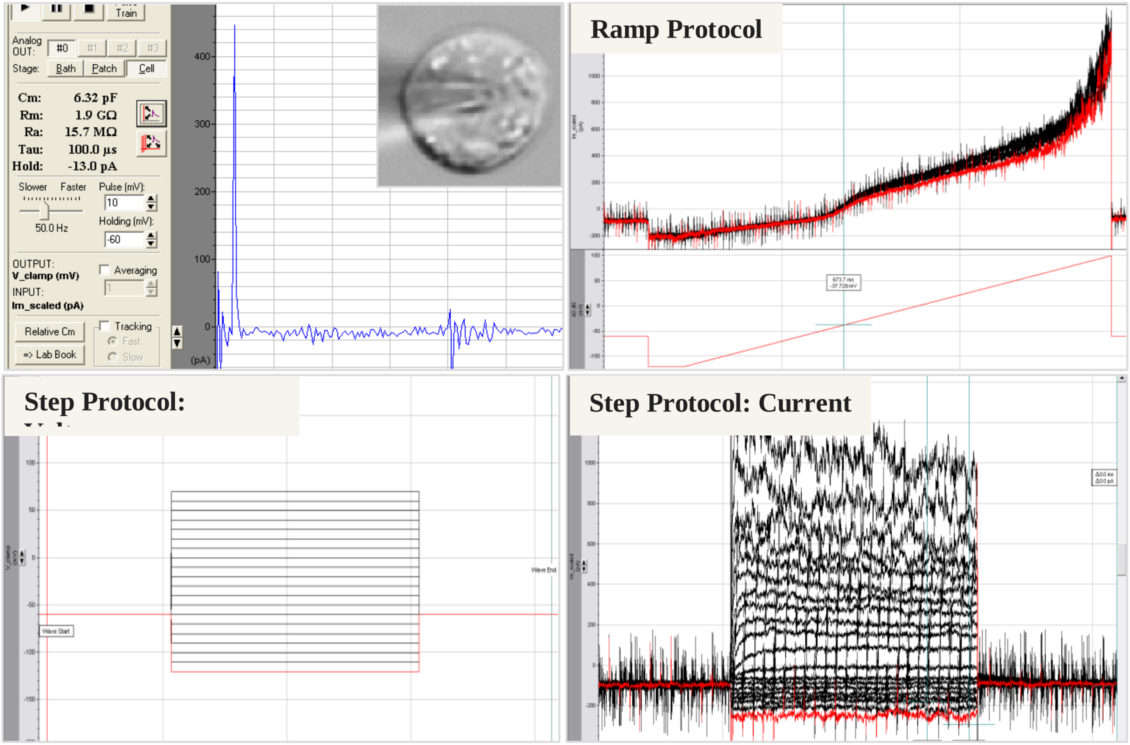

Cm: 6.32 pF
Rm: 1.9 GΩ
Ra: 15.7 MΩ
Tau: 100.0 µs
Hold: -13.0 pA

50.0 Hz

Pulse (mV): 10

Holding (mV): -60

OUTPUT: V_clamp (mV)

INPUT: Im_scaled (pA)

☐ Averaging 1

Figure 8.3 Protocols (ramp and step) for patch clamp experiments. The ramp protocol of stimulation consisted of voltage pulses of -120 to + 70 mV in 250 ms while the trans-membrane current was recorded simultaneously. By using the step protocol, the voltage pulses were increased from -120 to + 70 mV while trans-membrane currents were recorded for 200 ms during each voltage steps. Resting membrane potential (RMP) was calculated from the current and voltage curve for each cell.

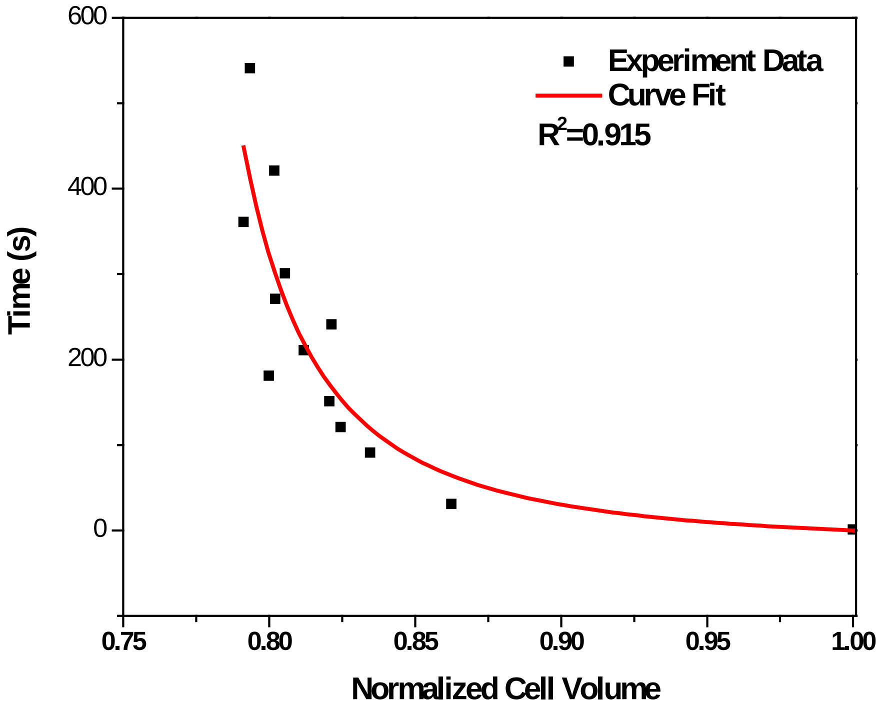
Experiment Data
Curve Fit
R²=0.915
Time (s)
600
400
200
0
0.75
0.80
0.85
0.90
0.95
1.00
Normalized Cell Volume

(a)

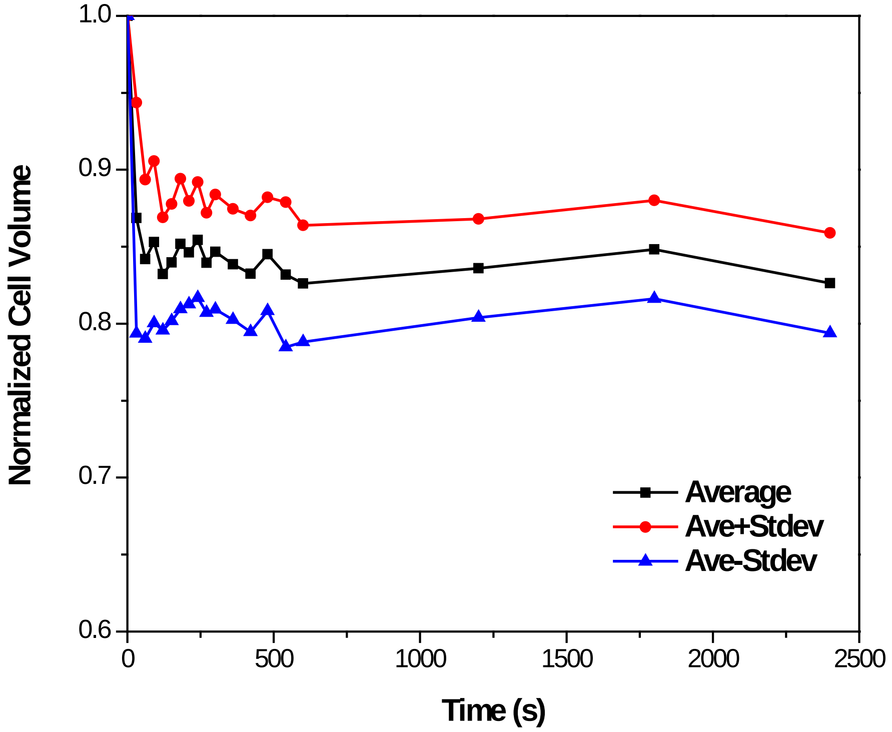
1.0
0.9
0.8
0.7
0.6
Normalized Cell Volume
Average
Ave+Stdev
Ave-Stdev
0
500
1000
1500
2000
2500
Time (s)

(b)

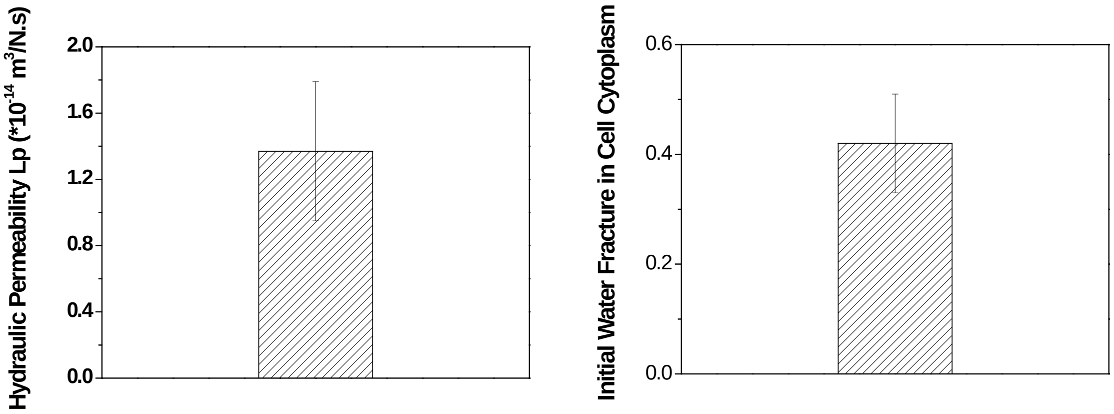

(c)

Figure 8.4 Hydraulic permeability and initial water content in porcine AF cells. (a) Typical passive cell volume response of a porcine AF cell under hypertonic condition. A good agreement is shown between the theoretical prediction and the experimental result. (b) Mean and standard deviation of passive cell volume response of porcine AF cells under hypertonic condition. (c) Results of curve fitting (hydraulic permeability and initial water content of AF cells) from the passive cell volume response curve, by using modified van’t Hoff equations.

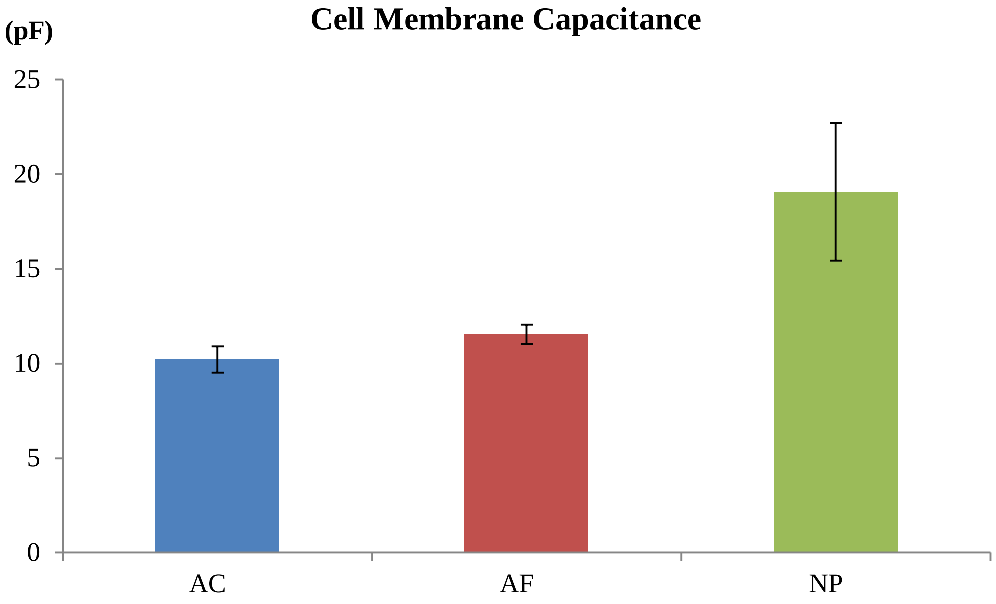

Figure 8.5 Cell membrane capacitance of porcine AC, AF, and NP cells. Significant difference was found between three cell types, while NP cell showed the largest capacitance compared to AF cells and AC (*$p < 0.05$).

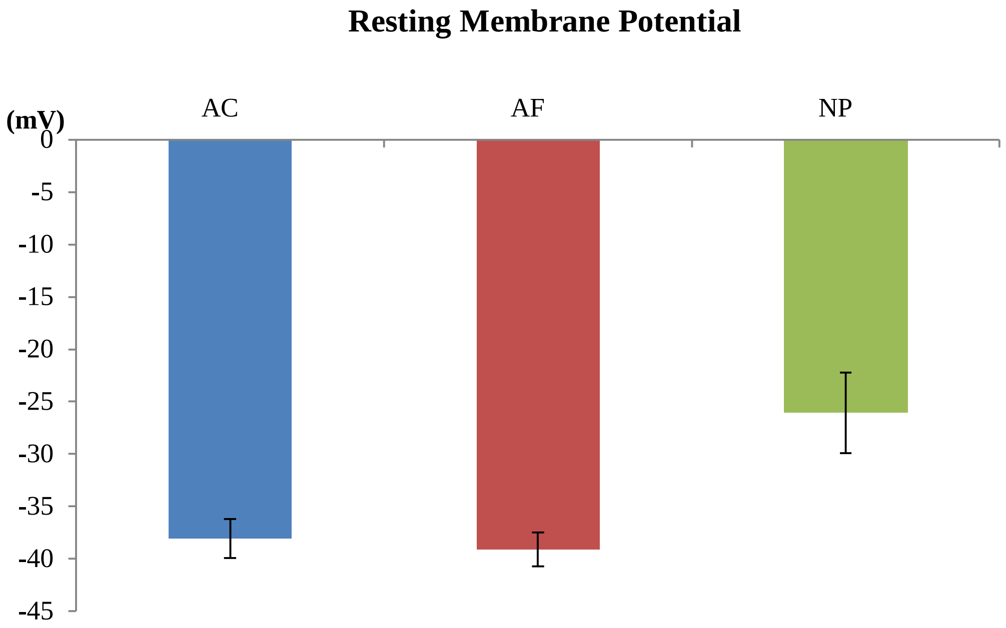

Figure 8.6 Cell resting membrane potential of porcine AC, AF, and NP cells. Significant difference was found between NP cell, AF and NP cells, while NP cell showed the smallest resting membrane potential compared to AF cells and AC (*$p < 0.05$).

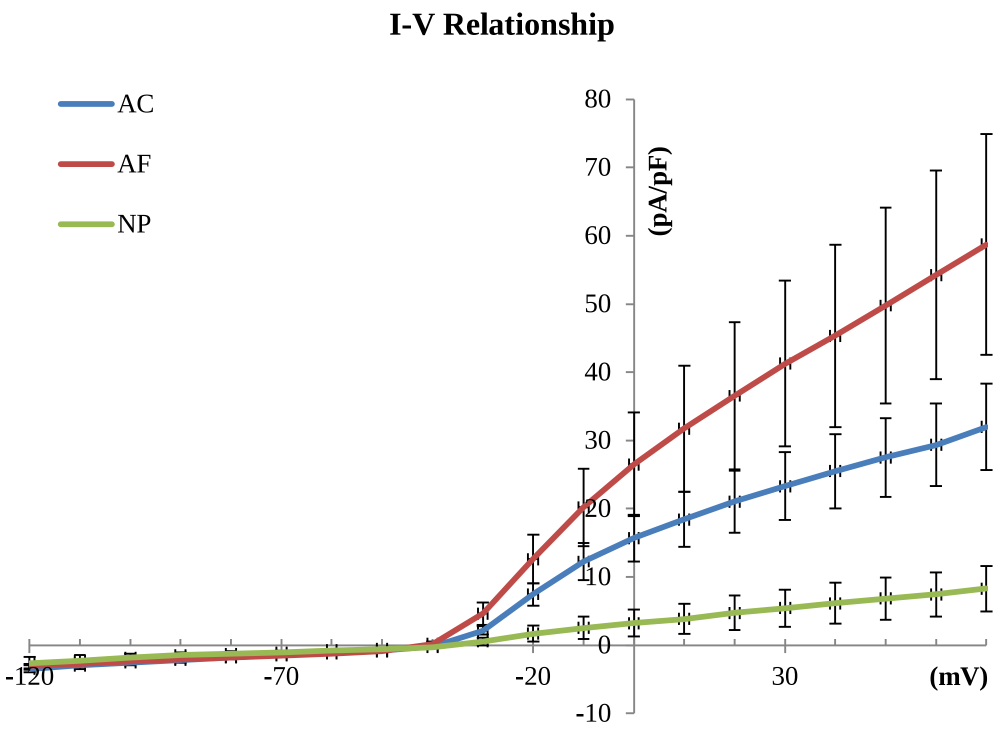

Figure 8.7 The current-voltage relationship of porcine AC, AF, and NP cells measured by step voltage protocol. Outwardly rectifying currents were found to be activated when the clamp voltages through the cell membrane are bigger than RMP in all three cell types. NP cells possessed the smallest current while the AF cells possessed the largest with the AC in between the two. In contrast, smaller currents were found when the clamp voltage through the cell membrane was lower than the relative RMP.

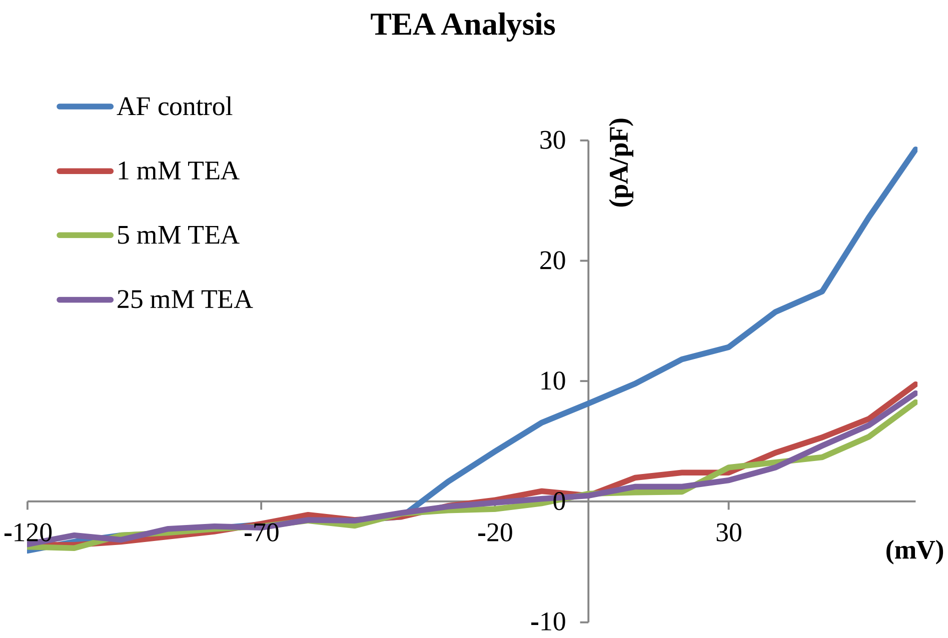

Figure 8.8 Effect of potassium channel blocker (TEA) on voltage activated current in porcine AF cells. The reversible manner was also found (the similar magnitude of voltage activated current can be seen after replacing the TEA solution with normal external solution).

8.4 Discussion

In this study, the assumption of spherical cell shape was used in the cell volume calculation which was consistent with previous studies in the literature and further validated by our confocal fluorescent imaging. It was also found that that during the hypertonic loading, only passive cell volume response exists in porcine AF cells at room temperature. The active cell volume regulation component was insignificant which was consistent with the concept that ion pumps or transporters for active ion transport through the cell membrane are inactive at room temperature which is significantly lower than body temperature as reported for AC cells in the literature. This is consistent with the observation that under osmotic loading conditions, no significant active cell volume regulation phenomena could be observed at room temperature [33, 101].

Our studies showed that the hydraulic permeability of porcine AF cell was ~0.4-0.7 times smaller than that of bovine AC cells. However, the initial active water content in the cytoplasm of porcine AF cell was ~0.2-0.35 smaller than that in bovine articular chondrocyte. This indicated that the IVD cell may have quantitatively different transport characteristics and homeostasis phenomena from AC due to its unique phenotype as discussed in Chapter 2 and Chapter 6.

In our patch clamp experiments for characterization of trans-membrane ion transport properties, the RMP of AC was consistent with that found in previous studies in other animal models (rabbit: -41.4 mV; canine: -38.1 mV; mouse: -46.0 mV) [259-261]. Significant different RMPs and capacitances were found between AC, AF and NP cells.

It may indicate different ion transport properties in the cell membrane from articular cartilage, AF and NP cells.

In this study, significantly larger voltage dependent currents found in both AC and AF cells indicated that there existed voltage active ion channels in these two cell types. By using tetraethylammonium (TEA, K^+ channel blocker), we found that voltage active ion channels in AC and AF cells are blocked in a dose dependent and reversible manner (Figure 8.8). It indicated that these voltage activated channels were K^+ channels. This finding is consistent with the voltage dependent K^+ channel found in the canine AC in the literature [260]. In addition, it was found that Cl^- channel in AC was calcium dependent [262]. In this study, the calcium concentration in both intracellular and external solutions is too low to activate the Cl^- channels. It further validated our conclusion that the voltage activated channels in this study were mainly K^+ channels. Therefore the value of L_1-L_2 in table 8.1 represented the conductances of voltage activated K^+ channel in both AC and AF cells. In contrast, the value of L_1 represented the combined conductance of Na^+ and Cl^- channels.

Moreover, significant difference was found in voltage activated K^+ conductances between AC, AF and NP cells. Based on Goldman equation developed by Hodgkins and Katz, significantly larger voltage activated K^+ conductance found in AF and AC could result in a more negative RMP which was consistent with our finding in RMPs (Figure 8.6). In addition, in NP cells, the K^+ channel was found to be less voltage dependent. Different capacitance and RMP were also found in NP cells compared to AC and AF cells. It indicated that NP and AF cells may have quantitatively different trans-membrane transport properties and different cell homeostasis phenomena.

Note that, all the measurements in this chapter were under room temperature. Based on previous studies, AC behaved as perfect osmometer and followed van't Hoff relation under room temperature. It indicated that hydraulic permeability of AC kept constant during passive cell volume response. Our study further validated this assumption in IVD cells. Therefore, the hydraulic permeability of IVD cells could be used for the cell model of homeostasis under steady state (isotonic condition), as well as passive volume response process. As for ion conductances, previous studies showed several swelling or stretch activated ion channels found in AC [124, 263]. Volume sensitive ion conductance could be expected during non-steady state of cell homeostasis. Therefore, the ion conductances measured in this study were only appropriate for the cell model of homeostasis under steady state. In order to further analyze the mechanism of IVD cell homeostasis, water and ion transport under body temperature needs to be characterized in the future. Ion pumps and cotransporters involved in the active volume regulation of the IVD cells also need to be further characterized. By changing nutrient levels in the culture environment for both normal and degenerated IVD cells, effects of nutrition on cell homeostasis could be quantitatively analyzed to help further understand IVD degeneration in the future.

8.5 Summary

In summary, this study quantitatively characterized the water and ion transport through the cell membrane in porcine IVD cells. Compared to AC cells, significantly different hydraulic permeability and ion conductance were found, as well as RMP and cell capacitance. In addition, voltage activated K^+ channel was found in AF cells while there was no significant sign in NP cells. It indicated that IVD cells may have different cell homeostasis phenomena and mechanisms compared with AC cells. The region difference between AF and NP cells also needs to be further analyzed in the future. In addition, the quantitative parameters measured in this study could be used in the multiphasic single cell model in Chapter 7 to quantitatively simulate the cell homeostasis and further analyze its mechanism in the future.

CHAPTER 9 OVERALL CONCLUSIONS AND FUTURE DIRECTIONS

9.1 Conclusions

The major impact of this work was the development of a novel multi-scale analytical model by incorporating experimentally determined IVD tissue and cell properties. It helped to predict the ECM nutrient environment and further analyze its effect on cell energy metabolism and homeostasis. First, the biomechanical and nutrient transport properties of CEP were characterized. Second, energy metabolism properties (consumption/production rates) of human IVD cells were measured in this study. Third, during the homeostasis, water and ion transport properties in the cell membrane in IVD cell was quantitatively analyzed. Meanwhile, the multiphasic FEM models were developed in both tissue level and cellular level. These studies supported our general hypothesis that CEP regulates the ECM osmotic and nutrient environment which further regulate IVD cell energy metabolism and homeostasis. By bridging biomechanics with cell physiology, this study helped to better understand IVD nutrition and cell homeostasis. Furthermore, it helped to establish a solid foundation in understanding the mechanism of IVD degeneration and provided new insights into cell based IVD regeneration therapies for low back pain.

Chapter 3: In this study, a multiphasic mechano-electrochemical finite element model of IVD was developed based on triphasic theory. Detailed formulation of the specialized triphasic theory for charged IVD tissue was presented. The IVD tissue is modeled as a mixture with four phases: solid phase with fixed charges, interstitial water phase, ion phase with two monovalent species (e.g., Na^+ and Cl^-), and uncharged nutrient solute phase. In this chapter, fundamental governing equations for the mixture, such as electro-neutrality condition, continuity equations, linear momentum equations and constitutive equations are also given.

Chapter 4: In the study, the weak form formulations of mixture model developed in chapter 2 were used for finite element analysis of physical signals and nutrient solute transport inside human IVD. The numerical results of this study showed that calcification of the cartilage endplate could significantly reduce the nutrient levels in human IVD. It also shows that in cell based therapy for IVD regeneration, excessive numbers of injected cells may cause further deterioration of the nutrient environment in the degenerated disc.

Chapter 5: The biphasic mechanical properties of cartilage endplate were measured to characterize its mechanical and transport behaviors which were also correlated with its histological and biochemical properties. The results of this study showed that CEP could block rapid solute convection and allow pressurization of the interstitial fluid in response to loading. The CEP also plays a significant role in nutrient transport within the IVD. Calcification of the CEP with aging or degeneration could affect the nutrient supply to the disc cells and further alter disc homeostasis which may lead to disc degeneration.

Chapter 6: The oxygen consumption rates of human IVD cells were measured in different glucose environmental conditions. Meanwhile, glucose consumption rates and lactate production rates of human IVD cells were measured under different oxygen conditions. These studies showed that consumption rates were significant and dependent on the nutrient environment. This study outlined energy metabolism properties of human

IVD cells at different nutrient environments and provided more evidence to further analyze the nutrient metabolism mechanism in the human IVD. The results of this study also provide valuable data for theoretically predicting the nutrient transport and distribution inside human IVD.

Chapter 7: A multiphasic single cell model was developed to simulate trans-membrane water and ion transport based on multiphasic theory. The IVD cells were modeled as a water-filled membrane with solid phase, water phase, ion phase and neutral solute phase. This is the first single cell model for cell homeostasis which is capable of simulating the interaction of mechanical tension force and ion transport. Furthermore, active ion transport during cell homeostasis was also incorporated in the model by adding a unique source term in the momentum equations.

Chapter 8: Trans-membrane water and ion transport during cell homeostasis were quantitatively characterized by cell volume response and patch clamp experiments. Hydraulic permeability and initial water content for IVD cells were quantitatively measured. Furthermore, by using articular chondrocytes as a reference, the capacitance, RMPs, and ion conductances of AF and NP cells were also measured under voltage or current clamp in the whole cell patch clamp mode. The results of this study indicated that trans-membrane transport properties in IVD cells are different from articular chondrocytes due to its unique cell phenotype. In addition, this study also provided valuable data for numerically analyzing the effect of change in extracellular environment on cell homeostasis.

9.2 Challenges

Chapter 3&4: In our multiphasic model, by choosing (electro)chemical potential as the primary degree of freedom, the jump conditions between elements and across the interface boundary are satisfied automatically. This feature allows this model to deal easily with the discontinuous material properties of the inhomogeneous and anisotropic human IVD tissue. However, due to lack of anisotropic material properties, the human IVD was considered as isotropic material in this study. In the future, it is necessary to use the anisotropic constitutive relationship in our theoretical model and simulation. In addition, due to lack of accurate shape of CEP, an approximate geometry of CEP was used in this simulation. Therefore, real image-based CEP needs to be used in our simulation in order to predict the ECM nutrient environment more accurately.

Chapter 5: Due to the high PG content in IVD tissue, the swelling pressure of CEP is relatively large while immersed in the PBS solution. This unique material property of the tissue caused a fatal error of the instrument in our preliminary characterization its dynamic viscoelastic properties under Perkin-Elmer 7e Dynamic Mechanical Analyzer (DMA). In the future, care should be taken while designing the mechanical testing protocols with an emphasis on new mechanical testing instrumentation.

Chapter 6: Due to the rarity of human IVD tissue and large amount of cell consumption in the energy metabolism experiments, second passaged degenerated human IVD cells cultured in high glucose DMEM were used. Effective passage and culture conditions needs to be further analyzed. Effect of degeneration of human IVD on its energy metabolism rate also needs to be studied once the normal human IVD tissue is available.

Chapter 7: We have successfully developed a novel single cell model to analyze the ion transport through the cell membrane based on multiphasic theory and classical non-equilibrium thermodynamics. However, until now, there is no constitutive relation for the new source term in the momentum governing equations. Further studies are needed to experimentally determine the source term for active ion transport in order to numerically analyze the effect of change in extracellular environment on the cell homeostasis.

Chapter 8: Porcine IVD cells were used in this study to establish the testing system and protocol as the primary animal model for characterization of trans-membrane water and ion transport. In the future, similar techniques could be applied to human IVD cells to validate the animal model. In addition, in order to further analyze the mechanism of cell homeostasis and IVD degeneration, the effects of changes in extracellular nutrient environment on cell homeostasis need to be addressed.

9.3 Future Goals

Low back pain is a major socio-economic concern in this country [1]. Although the exact cause for low back pain is unclear, the degenerative changes of the intervertebral disc (IVD) have been implicated as a possible primary etiologic factor [221, 264]. The broad, long-term objectives of this study are to (1) elucidate the etiology of disc degeneration, (2) develop strategies for restoring tissue function or preventing further disc degeneration, and (3) develop novel, less-invasive diagnostic tools for disc degeneration. The detailed future goals are as follows:

ECM Environment Prediction: We hope to further study the anisotropic mechanical and transport properties of the human CEP with emphasis on comparing porcine and human samples. Future work can be done to investigate the effect of age and gender on mechanical and transport properties. Histological studies to further correlate tissue structure and composition with material properties would also provide insight into human CEP function.

For cell energy metabolism of IVD cells, we only determined the rates of glucose consumption and lactate production of human IVD cells at 5% glucose level. Therefore, it is necessary to investigate the effect of glucose on the rates of glucose consumption and lactate production in a future study. It will also be valuable to study the coupling of oxygen consumption, glucose consumption, and lactate production to fully understand the energy metabolism in the human IVD cells. One method for testing this would be to block mitochondrial activity to limit energy metabolism entirely to glycolysis. By further characterizing the energy metabolism behavior of normal human IVD cells and comparing with the results in this study, effect of IVD degeneration on IVD cell energy metabolism could be analyzed and therefore help us to further understand the mechanism of IVD degeneration

By incorporating these experimentally determined anisotropic mechanical/transport and cell energy metabolism properties into our multiphasic finite element model, we could predict a more accurate ECM biomechanical and nutrient environment of the human IVD. The model will help us understand both physiological and pathological loading conditions that could elucidate the mechanisms of human IVD degeneration. Furthermore, additional magnetic resonance images (MRI) and motion tracking data of human IVD and spine could help to build a more accurate numerical model and serve as the patient specific diagnostic tool for IVD degeneration.

Cell Homeostasis: We hope to further study trans-membrane transport in IVD cells during homeostasis with emphasis on comparing porcine and human cells. By analyzing the effect of the change in extracellular nutrient environment on cell homeostasis as a result of IVD degeneration, we hope to reach insights into the key role of cell metabolism and homeostasis during tissue degeneration/regeneration process. Furthermore, the normal and degenerated human IVD cells could serve as unique tools for us to build and validate the new hypothesis for the mechanism of degeneration in cellular/molecular levels in the future. In addition, we hope to quantitatively analyze the active ion transport through the cell membrane and eventually establish quantitative constitutive relationships to describe it. By incorporating these experimental determined trans-membrane transport properties and constitutive relationships into our novel multiphasic single cell model, we could build a numerical tool to predict cell homeostasis and further analyze the mechanism. It will help to provided new insights into IVD degeneration mechanism and further guide cell based IVD regeneration in tissue engineering or clinical therapy.

APPENDIX

A Saturation Condition

$$\phi^{\mathbf{s}} + \phi^{\mathbf{w}} + \phi^{+} + \phi^{-} + \phi^{n} = 1, \tag{1}$$

Note that, the volume fraction is defined as the volume ratio of the component to the total tissue ($\phi^{\alpha} = dV^{\alpha} \big/ dV$, α: s, w, +, -, n). In Equation (1), ϕ^{s} and ϕ^{w} are the solidity and the porosity of the tissue respectively; ϕ^{+} and ϕ^{-} are ion volume fractions; ϕ^{n} is the volume fraction of nutrient solute. Under physiological conditions (ϕ^{+}, ϕ^{-} and ϕ^{n} are very small), Equation (1) could also be rewritten as $\phi^{s} + \phi^{w} = 1$.

B Apparent Mass Density Condition

$$\rho^{s} = \rho_{T}^{s} \phi^{s}, \tag{2}$$

$$\rho^{w} = \rho_{T}^{w} \phi^{w}, \tag{3}$$

$$\rho^{+} = \phi^{w} c^{+} M_{+} = \rho_{T}^{+} \phi^{+}, \tag{4}$$

$$\rho^{-} = \phi^{w} c^{-} M_{-} = \rho_{T}^{-} \phi^{-}, \tag{5}$$

$$\rho^{n} = \phi^{\mathbf{w}}\, c^{n} M_{n} = \rho_{T}^{n} \phi^{n}, \tag{6}$$

Note that, the apparent mass density ρ^{α} is defined as mass per unit mixture volume in this study, while the true mass density ρ_T^{α} is usually defined as mass in each unit volume of α-component. In Equation (4-6), c^+, c^- and c^n are defined as the molar concentrations of cation, anion and nutrient solute respectively, while M_+, M_- and M_n are defined as the corresponding molecular weight. In this study, molar concentration represents moles of the component in each unit water volume.

C Electro-neutrality Condition

$$c^+ = c^- + c^F, \tag{7}$$

In this study, the net charge in any infinitesimal volume of the mixture is assumed as zero. In equation 7, c^F represents the absolute value of negatively fixed charge density. Note that, the electroneutrality condition is a good assumption for the biological tissue except at the boundary [177]. In application of mixture theory under cellular level, the whole cell membrane could also be assumed as electro-neutral, while the net charge on cell surface may not be zero.

D Relationship between Friction Coefficient and Transport Parameters

The functional relationships between the material coefficients (B_{ij}) and the frictional coefficients ($f_{\alpha\beta}$) are given by Equation (8-24).

$$\mathrm{B}_{11} = \frac{1}{\mathrm{F}}(f_{+w} + f_{+s})(f_{-w} + f_{-s})(f_{nw} + f_{ns}), \tag{8}$$

$$\mathrm{B}_{12} = \frac{1}{\mathrm{F}} f_{+w}(f_{-w} + f_{-s})(f_{nw} + f_{ns}), \tag{9}$$

$$\mathrm{B}_{13} = \frac{1}{\mathrm{F}}(f_{+w} + f_{+s}) f_{-w}(f_{nw} + f_{ns}), \tag{10}$$

$$\mathrm{B}_{14} = \frac{1}{\mathrm{F}}(f_{+w} + f_{+s})(f_{-w} + f_{-s}) f_{nw}, \tag{11}$$

$$\mathrm{B}_{21} = \frac{f_{+w}}{f_{+w} + f_{+s}}, \tag{12}$$

$$\mathrm{B}_{22} = \frac{1}{f_{+w} + f_{+s}}, \tag{13}$$

$$\mathrm{B}_{23} = 0, \tag{14}$$

$$\mathrm{B}_{24} = 0, \tag{15}$$

$$\mathrm{B}_{31} = \frac{f_{-w}}{f_{-w} + f_{-s}}, \tag{16}$$

$$\mathrm{B}_{32} = \frac{1}{f_{-w} + f_{-s}}, \tag{17}$$

$$\mathrm{B}_{33} = 0, \tag{18}$$

$$\mathrm{B}_{34} = 0, \tag{19}$$

$$\mathrm{B}_{41} = \frac{f_{nw}}{f_{nw} + f_{ns}}, \tag{20}$$

$$\mathrm{B}_{42} = \frac{1}{f_{nw} + f_{ns}}, \tag{21}$$

$$\mathrm{B}_{43} = 0, \tag{22}$$

$$\mathrm{B}_{44} = 0, \tag{23}$$

$$\begin{aligned} \mathrm{F} = {} & (f_{ws} + f_{+w} + f_{-w} + f_{nw})(f_{+w} + f_{+s})(f_{-w} + f_{-s})(f_{nw} + f_{ns}) \\ & - (f_{+w})^2 (f_{-w} + f_{-s})(f_{nw} + f_{ns}) - (f_{+w} + f_{+s})(f_{-w})^2 (f_{nw} + f_{ns}) \\ & - (f_{+w} + f_{+s})(f_{-w} + f_{-s})(f_{nw})^2 \ . \end{aligned} \tag{24}$$

Note that, the frictional coefficients between nutrient solute and ions (f_{n+} and f_{n-}) and between cation and anion (f_{+-}) are assumed to be negligible.

The relations of the phenomenological transport parameters to the material coefficients (B_{ij}) are given by Equation (25-29).

$$k = (\phi^w)^2 \mathrm{B}_{11}, \tag{25}$$

$$e^{+} = \mathrm{B}_{12}/\mathrm{B}_{11}, \qquad e^{-} = \mathrm{B}_{13}/\mathrm{B}_{11}, \qquad e^{o} = \mathrm{B}_{14}/\mathrm{B}_{11}, \tag{26}$$

$$H^{+} = \mathrm{B}_{21}, \qquad D^{+} = RT\omega^{+} = RT\phi^{w}c^{+}\mathrm{B}_{22}, \tag{27}$$

$$H^{-} = \mathrm{B}_{31}, \qquad D^{-} = RT\omega^{-} = RT\phi^{w}c^{-}\mathrm{B}_{32}, \tag{28}$$

$$H^{n} = \mathrm{B}_{41}, \qquad D^{n} = RT\varphi^{w}c^{n}\,\mathrm{B}_{42}. \tag{29}$$

where k, e^{α}, H^{α}, D^{α}, and ω^{β} (α = +, –, n; β = +, –), represent the hydraulic permeability of the water, the transport factor of the solute, the hindrance factor of the solute for the convection, the diffusivity of the solute in the tissue, and the mobility of the solute [186, 188], respectively.

REFERENCES

1. Deyo RA & Weinstein JN. Low back pain. N Engl J Med 2001; 344(5):363-70.

2. Maniadakis N & Gray A. The economic burden of back pain in the UK. Pain 2000; 84(1):95-103.

3. van Tulder MW, Koes BW, & Bouter LM. A cost-of-illness study of back pain in The Netherlands. Pain 1995; 62(2):233-40.

4. Luoma K, Riihimaki H, Luukkonen R, Raininko R, Viikari-Juntura E, & Lamminen A. Low back pain in relation to lumbar disc degeneration. Spine (Phila Pa 1976) 2000; 25(4):487-92.

5. Boden SD, Davis DO, Dina TS, Patronas NJ, & Wiesel SW. Abnormal magnetic-resonance scans of the lumbar spine in asymptomatic subjects. A prospective investigation. J Bone Joint Surg Am 1990; 72(3):403-8.

6. Boos N, Weissbach S, Rohrbach H, Weiler C, Spratt KF, & Nerlich AG. Classification of age-related changes in lumbar intervertebral discs: 2002 Volvo Award in basic science. Spine (Phila Pa 1976) 2002; 27(23):2631-44.

7. Miller JA, Schmatz C, & Schultz AB. Lumbar disc degeneration: correlation with age, sex, and spine level in 600 autopsy specimens. Spine (Phila Pa 1976) 1988; 13(2):173-8.

8. Urban JP & Maroudas A. Swelling of the intervertebral disc in vitro. Connect Tissue Res 1981; 9(1):1-10.

9. Gu WY, Mao XG, Rawlins BA, Iatridis JC, Foster RJ, Sun DN, Weidenbaum M, & Mow VC. Streaming potential of human lumbar anulus fibrosus is anisotropic and affected by disc degeneration. Journal of biomechanics 1999; 32(11):1177-82.

10. Urban JP. The role of the physicochemical environment in determining disc cell behaviour. Biochem Soc Trans 2002; 30(Pt 6):858-64.

11. Bayliss MT, Urban JP, Johnstone B, & Holm S. In vitro method for measuring synthesis rates in the intervertebral disc. Journal of orthopaedic research : official publication of the Orthopaedic Research Society 1986; 4(1):10-17.

12. Nachemson A, Lewin T, Maroudas A, & Freeman MA. In vitro diffusion of dye through the end-plates and the annulus fibrosus of human lumbar inter-vertebral discs. Acta Orthop Scand 1970; 41(6):589-607.

13. Lai WM, Hou JS, & Mow VC. A triphasic theory for the swelling and deformation behaviors of articular cartilage. J Biomech Eng 1991; 113(3):245-58.

14. Gu WY, Lai WM, & Mow VC. A mixture theory for charged-hydrated soft tissues containing multi-electrolytes: passive transport and swelling behaviors. J Biomech Eng 1998; 120(2):169-80.

15. Bibby SR & Urban JP. Effect of nutrient deprivation on the viability of intervertebral disc cells. Eur Spine J 2004; 13(8):695-701.

16. Bibby SR, Jones DA, Ripley RM, & Urban JP. Metabolism of the intervertebral disc: effects of low levels of oxygen, glucose, and pH on rates of energy metabolism of bovine nucleus pulposus cells. Spine 2005; 30(5):487-96.

17. Huang CY, Yuan TY, Jackson AR, Hazbun L, Fraker C, & Gu WY. Effects of low glucose concentrations on oxygen consumption rates of intervertebral disc cells. Spine 2007; 32(19):2063-9.

18. Guehring T, Wilde G, Sumner M, Grunhagen T, Karney GB, Tirlapur UK, & Urban JP. Notochordal intervertebral disc cells: sensitivity to nutrient deprivation. Arthritis Rheum 2009; 60(4):1026-34.

19. Selard E, Shirazi-Adl A, & Urban JP. Finite element study of nutrient diffusion in the human intervertebral disc. Spine 2003; 28(17):1945-53.

20. Ferguson SJ, Ito K, & Nolte LP. Fluid flow and convective transport of solutes within the intervertebral disc. J Biomech 2004; 37(2):213-21.

21. Yao H & Gu WY. Physical signals and solute transport in cartilage under dynamic unconfined compression: finite element analysis. Ann Biomed Eng 2004; 32(3):380-90.

22. Yao H & Gu WY. Physical signals and solute transport in human intervertebral disc during compressive stress relaxation: 3D finite element analysis. Biorheology 2006; 43(3-4):323-35.

23. Yao H & Gu WY. Three-dimensional inhomogeneous triphasic finite-element analysis of physical signals and solute transport in human intervertebral disc under axial compression. J Biomech 2007; 40(9):2071-7.

24. Huang CY & Gu WY. Effects of mechanical compression on metabolism and distribution of oxygen and lactate in intervertebral disc. J Biomech 2008; 41(6):1184-96.

25. Sakai D, Mochida J, Iwashina T, Watanabe T, Nakai T, Ando K, & Hotta T. Differentiation of mesenchymal stem cells transplanted to a rabbit degenerative disc model: potential and limitations for stem cell therapy in disc regeneration. Spine (Phila Pa 1976) 2005; 30(21):2379-87.

26. Watanabe K, Mochida J, Nomura T, Okuma M, Sakabe K, & Seiki K. Effect of reinsertion of activated nucleus pulposus on disc degeneration: an experimental study on various types of collagen in degenerative discs. Connect Tissue Res 2003; 44(2):104-8.

27. Ganey T, Libera J, Moos V, Alasevic O, Fritsch KG, Meisel HJ, & Hutton WC. Disc chondrocyte transplantation in a canine model: a treatment for degenerated or damaged intervertebral disc. Spine (Phila Pa 1976) 2003; 28(23):2609-20.

28. Xu X, Urban JP, Tirlapur UK, & Cui Z. Osmolarity effects on bovine articular chondrocytes during three-dimensional culture in alginate beads. Osteoarthritis Cartilage 2010; 18(3):433-9.

29. Miley HE, Holden D, Grint R, Best L, & Brown PD. Regulatory volume increase in rat pancreatic beta-cells. Pflugers Arch 1998; 435(2):227-30.

30. Wehner F, Olsen H, Tinel H, Kinne-Saffran E, & Kinne RK. Cell volume regulation: osmolytes, osmolyte transport, and signal transduction. Rev Physiol Biochem Pharmacol 2003; 148:1-80.

31. Okada Y. Ion channels and transporters involved in cell volume regulation and sensor mechanisms. Cell Biochem Biophys 2004; 41(2):233-58.

32. Bush PG & Hall AC. Regulatory volume decrease (RVD) by isolated and in situ bovine articular chondrocytes. J Cell Physiol 2001; 187(3):304-14.

33. Bush PG & Hall AC. The osmotic sensitivity of isolated and in situ bovine articular chondrocytes. J Orthop Res 2001; 19(5):768-78.

34. Erickson GR, Alexopoulos LG, & Guilak F. Hyper-osmotic stress induces volume change and calcium transients in chondrocytes by transmembrane, phospholipid, and G-protein pathways. Journal of biomechanics 2001; 34(12):1527-35.

35. Pritchard S, Erickson GR, & Guilak F. Hyperosmotically induced volume change and calcium signaling in intervertebral disk cells: the role of the actin cytoskeleton. Biophys J 2002; 83(5):2502-10.

36. Erickson GR, Northrup DL, & Guilak F. Hypo-osmotic stress induces calcium-dependent actin reorganization in articular chondrocytes. Osteoarthritis Cartilage 2003; 11(3):187-97.

37. Albro MB, Petersen LE, Li R, Hung CT, & Ateshian GA. Influence of the partitioning of osmolytes by the cytoplasm on the passive response of cells to osmotic loading. Biophys J 2009; 97(11):2886-93.

38. Pritchard S & Guilak F. The role of F-actin in hypo-osmotically induced cell volume change and calcium signaling in anulus fibrosus cells. Ann Biomed Eng 2004; 32(1):103-11.

39. Kedem O & Katchalsky A. Thermodynamic analysis of the permeability of biological membranes to non-electrolytes. Biochim Biophys Acta 1958; 27(2):229-46.

40. Lai WM, Hou JS, & Mow VC. A triphasic theory for the swelling and deformation behaviors of articular cartilage. Journal of biomechanical engineering 1991; 113(3):245-58.

41. Ateshian GA, Likhitpanichkul M, & Hung CT. A mixture theory analysis for passive transport in osmotic loading of cells. J Biomech 2006; 39(3):464-75.

42. Haider MA, Schugart RC, Setton LA, & Guilak F. A mechano-chemical model for the passive swelling response of an isolated chondron under osmotic loading. Biomech Model Mechanobiol 2006; 5(2-3):160-71.

43. Moore RJ. The vertebral end-plate: what do we know? Eur Spine J 2000; 9(2):92-6.

44. Horner HA & Urban JP. 2001 Volvo Award Winner in Basic Science Studies: Effect of nutrient supply on the viability of cells from the nucleus pulposus of the intervertebral disc. Spine (Phila Pa 1976) 2001; 26(23):2543-9.

45. Bibby SR, Fairbank JC, Urban MR, & Urban JP. Cell viability in scoliotic discs in relation to disc deformity and nutrient levels. Spine (Phila Pa 1976) 2002; 27(20):2220-8.

46. Ateshian GA, Morrison B, 3rd, & Hung CT. Modeling of active transmembrane transport in a mixture theory framework. Ann Biomed Eng 2010; 38(5):1801-14.

47. Friedman MH (2008) Principles and Models of Biological Transport. (Springer, New York, NY).

48. Nelson PC, Radosavljevic M, & Bromberg S (2004) Biological Physics: Energy, Information, Life. (W.H. Freeman and Co., New York).

49. Marchand F & Ahmed AM. Investigation of the laminate structure of lumbar disc anulus fibrosus. Spine (Phila Pa 1976) 1990; 15(5):402-10.

50. Cassidy JJ, Hiltner A, & Baer E. Hierarchical structure of the intervertebral disc. Connect Tissue Res 1989; 23(1):75-88.

51. Urban JP & Roberts S. Degeneration of the intervertebral disc. Arthritis Res Ther 2003; 5(3):120-30.

52. Inoue H. Three-dimensional architecture of lumbar intervertebral discs. Spine (Phila Pa 1976) 1981; 6(2):139-46.

53. Yu J, Winlove PC, Roberts S, & Urban JP. Elastic fibre organization in the intervertebral discs of the bovine tail. J Anat 2002; 201(6):465-75.

54. Maroudas A, Stockwell RA, Nachemson A, & Urban J. Factors involved in the nutrition of the human lumbar intervertebral disc: cellularity and diffusion of glucose in vitro. J Anat 1975; 120(Pt 1):113-30.

55. Errington RJ, Puustjarvi K, White IR, Roberts S, & Urban JP. Characterisation of cytoplasm-filled processes in cells of the intervertebral disc. J Anat 1998; 192 (Pt 3):369-78.

56. Bruehlmann SB, Rattner JB, Matyas JR, & Duncan NA. Regional variations in the cellular matrix of the annulus fibrosus of the intervertebral disc. J Anat 2002; 201(2):159-71.

57. Roberts S, Menage J, & Urban JP. Biochemical and structural properties of the cartilage end-plate and its relation to the intervertebral disc. Spine 1989; 14(2):166-74.

58. Roberts S, Menage J, & Eisenstein SM. The cartilage end-plate and intervertebral disc in scoliosis: calcification and other sequelae. Journal of orthopaedic research : official publication of the Orthopaedic Research Society 1993; 11(5):747-57.

59. Antoniou J, Steffen T, Nelson F, Winterbottom N, Hollander AP, Poole RA, Aebi M, & Alini M. The human lumbar intervertebral disc: evidence for changes in the biosynthesis and denaturation of the extracellular matrix with growth, maturation, ageing, and degeneration. J Clin Invest 1996; 98(4):996-1003.

60. Nachemson A & Elfstrom G. Intravital dynamic pressure measurements in lumbar discs. A study of common movements, maneuvers and exercises. Scand J Rehabil Med Suppl 1970; 1:1-40.

61. Boos N, Wallin A, Gbedegbegnon T, Aebi M, & Boesch C. Quantitative MR imaging of lumbar intervertebral disks and vertebral bodies: influence of diurnal water content variations. Radiology 1993; 188(2):351-54.

62. Ledsome JR, Lessoway V, Susak LE, Gagnon FA, Gagnon R, & Wing PC. Diurnal changes in lumbar intervertebral distance, measured using ultrasound. Spine (Phila Pa 1976) 1996; 21(14):1671-5.

63. Adams MA, Dolan P, Hutton WC, & Porter RW. Diurnal changes in spinal mechanics and their clinical significance. J Bone Joint Surg Br 1990; 72(2):266-70.

64. Eyre DR, Matsui Y, & Wu JJ. Collagen polymorphisms of the intervertebral disc. Biochem Soc Trans 2002; 30(Pt 6):844-8.

65. Eyre DR & Muir H. Quantitative analysis of types I and II collagens in human intervertebral discs at various ages. Biochim Biophys Acta 1977; 492(1):29-42.

66. Urban JP & McMullin JF. Swelling pressure of the inervertebral disc: influence of proteoglycan and collagen contents. Biorheology 1985; 22(2):145-57.

67. Feng H, Danfelter M, Stromqvist B, & Heinegard D. Extracellular matrix in disc degeneration. J Bone Joint Surg Am 2006; 88 Suppl 2:25-9.

68. Lorenzo P, Bayliss MT, & Heinegard D. A novel cartilage protein (CILP) present in the mid-zone of human articular cartilage increases with age. J Biol Chem 1998; 273(36):23463-8.

69. Kizawa H, Kou I, Iida A, Sudo A, Miyamoto Y, Fukuda A, Mabuchi A, Kotani A, Kawakami A, Yamamoto S, *et al.* An aspartic acid repeat polymorphism in asporin inhibits chondrogenesis and increases susceptibility to osteoarthritis. Nat Genet 2005; 37(2):138-44.

70. Domowicz M, Li H, Hennig A, Henry J, Vertel BM, & Schwartz NB. The biochemically and immunologically distinct CSPG of notochord is a product of the aggrecan gene. Dev Biol 1995; 171(2):655-64.

71. Gotz W, Kasper M, Fischer G, & Herken R. Intermediate filament typing of the human embryonic and fetal notochord. Cell Tissue Res 1995; 280(2):455-62.

72. Kim KW, Lim TH, Kim JG, Jeong ST, Masuda K, & An HS. The origin of chondrocytes in the nucleus pulposus and histologic findings associated with the transition of a notochordal nucleus pulposus to a fibrocartilaginous nucleus pulposus in intact rabbit intervertebral discs. Spine (Phila Pa 1976) 2003; 28(10):982-90.

73. Peacock A. Observations on the prenatal development of the intervertebral disc in man. J Anat 1951; 85(3):260-74.

74. Johnson WE & Roberts S. Human intervertebral disc cell morphology and cytoskeletal composition: a preliminary study of regional variations in health and disease. J Anat 2003; 203(6):605-12.

75. Hunter CJ, Matyas JR, & Duncan NA. The three-dimensional architecture of the notochordal nucleus pulposus: novel observations on cell structures in the canine intervertebral disc. J Anat 2003; 202(Pt 3):279-91.

76. Poiraudeau S, Monteiro I, Anract P, Blanchard O, Revel M, & Corvol MT. Phenotypic characteristics of rabbit intervertebral disc cells. Comparison with cartilage cells from the same animals. Spine (Phila Pa 1976) 1999; 24(9):837-44.

77. Rufai A, Benjamin M, & Ralphs JR. The development of fibrocartilage in the rat intervertebral disc. Anat Embryol (Berl) 1995; 192(1):53-62.

78. Oegema TR, Jr. Biochemistry of the intervertebral disc. Clin Sports Med 1993; 12(3):419-39.

79. Higuchi M & Abe K. Postmortem changes in ultrastructures of the mouse intervertebral disc. Spine (Phila Pa 1976) 1987; 12(1):48-52.

80. Roberts S, Menage J, Duance V, Wotton S, & Ayad S. 1991 Volvo Award in basic sciences. Collagen types around the cells of the intervertebral disc and cartilage end plate: an immunolocalization study. Spine (Phila Pa 1976) 1991; 16(9):1030-8.

81. Setton LA & Chen J. Cell mechanics and mechanobiology in the intervertebral disc. Spine (Phila Pa 1976) 2004; 29(23):2710-23.

82. Baer AE, Laursen TA, Guilak F, & Setton LA. The micromechanical environment of intervertebral disc cells determined by a finite deformation, anisotropic, and biphasic finite element model. J Biomech Eng 2003; 125(1):1-11.

83. Urban JP & McMullin JF. Swelling pressure of the lumbar intervertebral discs: influence of age, spinal level, composition, and degeneration. Spine (Phila Pa 1976) 1988; 13(2):179-87.

84. Johnstone B & Bayliss MT. The large proteoglycans of the human intervertebral disc. Changes in their biosynthesis and structure with age, topography, and pathology. Spine (Phila Pa 1976) 1995; 20(6):674-84.

85. Inkinen RI, Lammi MJ, Lehmonen S, Puustjarvi K, Kaapa E, & Tammi MI. Relative increase of biglycan and decorin and altered chondroitin sulfate epitopes in the degenerating human intervertebral disc. J Rheumatol 1998; 25(3):506-14.

86. Duance VC, Crean JK, Sims TJ, Avery N, Smith S, Menage J, Eisenstein SM, & Roberts S. Changes in collagen cross-linking in degenerative disc disease and scoliosis. Spine (Phila Pa 1976) 1998; 23(23):2545-51.

87. Oegema TR, Jr., Johnson SL, Aguiar DJ, & Ogilvie JW. Fibronectin and its fragments increase with degeneration in the human intervertebral disc. Spine (Phila Pa 1976) 2000; 25(21):2742-7.

88. Johnson WE, Eisenstein SM, & Roberts S. Cell cluster formation in degenerate lumbar intervertebral discs is associated with increased disc cell proliferation. Connect Tissue Res 2001; 42(3):197-207.

89. Urban JP, Holm S, & Maroudas A. Diffusion of small solutes into the intervertebral disc: as in vivo study. Biorheology 1978; 15(3-4):203-21.

90. Kauppila LI. Prevalence of stenotic changes in arteries supplying the lumbar spine. A postmortem angiographic study on 140 subjects. Ann Rheum Dis 1997; 56(10):591-5.

91. Holm S & Nachemson A. Variations in the nutrition of the canine intervertebral disc induced by motion. Spine (Phila Pa 1976) 1983; 8(8):866-74.

92. Roberts S, Urban JP, Evans H, & Eisenstein SM. Transport properties of the human cartilage endplate in relation to its composition and calcification. Spine 1996; 21(4):415-20.

93. Crock HV GM, Yoshizawa H. Vascular anatomy related to the intervertebral disc. Biology of the intervertebral disc. ed P G. Boca Raton, FL: CLC Press; 1991; pp 109-33.

94. Windhaber RA, Wilkins RJ, & Meredith D. Functional characterisation of glucose transport in bovine articular chondrocytes. Pflugers Arch 2003; 446(5):572-7.

95. Bibby SR, Jones DA, Ripley RM, & Urban JP. Metabolism of the intervertebral disc: effects of low levels of oxygen, glucose, and pH on rates of energy metabolism of bovine nucleus pulposus cells. Spine (Phila Pa 1976) 2005; 30(5):487-96.

96. Ishihara H & Urban JP. Effects of low oxygen concentrations and metabolic inhibitors on proteoglycan and protein synthesis rates in the intervertebral disc. Journal of orthopaedic research : official publication of the Orthopaedic Research Society 1999; 17(6):829-35.

97. Ohshima H & Urban JP. The effect of lactate and pH on proteoglycan and protein synthesis rates in the intervertebral disc. Spine (Phila Pa 1976) 1992; 17(9):1079-82.

98. Lee RB, Wilkins RJ, Razaq S, & Urban JP. The effect of mechanical stress on cartilage energy metabolism. Biorheology 2002; 39(1-2):133-43.

99. Pfander D, Cramer T, Schipani E, & Johnson RS. HIF-1alpha controls extracellular matrix synthesis by epiphyseal chondrocytes. J Cell Sci 2003; 116(Pt 9):1819-26.

100. Lang F, Busch GL, Ritter M, Volkl H, Waldegger S, Gulbins E, & Haussinger D. Functional significance of cell volume regulatory mechanisms. Physiol Rev 1998; 78(1):247-306.

101. Bush PG & Hall AC. Passive osmotic properties of in situ human articular chondrocytes within non-degenerate and degenerate cartilage. J Cell Physiol 2005; 204(1):309-19.

102. Maroudas A & Venn M. Chemical composition and swelling of normal and osteoarthrotic femoral head cartilage. II. Swelling. Ann Rheum Dis 1977; 36(5):399-406.

103. Urban JP, Hall AC, & Gehl KA. Regulation of matrix synthesis rates by the ionic and osmotic environment of articular chondrocytes. J Cell Physiol 1993; 154(2):262-70.

104. Poole CA. Articular cartilage chondrons: form, function and failure. J Anat 1997; 191 (Pt 1):1-13.

105. Bush PG & Hall AC. The volume and morphology of chondrocytes within non-degenerate and degenerate human articular cartilage. Osteoarthritis Cartilage 2003; 11(4):242-51.

106. Chao PG, Tang Z, Angelini E, West AC, Costa KD, & Hung CT. Dynamic osmotic loading of chondrocytes using a novel microfluidic device. J Biomech 2005; 38(6):1273-81.

107. Maroudas A. Physical chemistry and the structure of cartilage. J Physiol 1972; 223(1):21P-22P.

108. Errington RJ, Fricker MD, Wood JL, Hall AC, & White NS. Four-dimensional imaging of living chondrocytes in cartilage using confocal microscopy: a pragmatic approach. Am J Physiol 1997; 272(3 Pt 1):C1040-51.

109. Siczkowski M & Watt FM. Subpopulations of chondrocytes from different zones of pig articular cartilage. Isolation, growth and proteoglycan synthesis in culture. J Cell Sci 1990; 97 (Pt 2):349-60.

110. Xu X, Cui Z, & Urban JP. Measurement of the chondrocyte membrane permeability to Me2SO, glycerol and 1,2-propanediol. Med Eng Phys 2003; 25(7):573-9.

111. Guilak F, Ratcliffe A, & Mow VC. Chondrocyte deformation and local tissue strain in articular cartilage: a confocal microscopy study. Journal of orthopaedic research : official publication of the Orthopaedic Research Society 1995; 13(3):410-21.

112. Alexopoulos LG, Erickson GR, & Guilak F. A method for quantifying cell size from differential interference contrast images: validation and application to osmotically stressed chondrocytes. J Microsc 2002; 205(Pt 2):125-35.

113. Kerrigan MJ, Hook CS, Qusous A, & Hall AC. Regulatory volume increase (RVI) by in situ and isolated bovine articular chondrocytes. J Cell Physiol 2006; 209(2):481-92.

114. Shaked NT, Finan JD, Guilak F, & Wax A. Quantitative phase microscopy of articular chondrocyte dynamics by wide-field digital interferometry. J Biomed Opt 2010; 15(1):010505.

115. Yellowley CE, Hancox JC, & Donahue HJ. Effects of cell swelling on intracellular calcium and membrane currents in bovine articular chondrocytes. J Cell Biochem 2002; 86(2):290-301.

116. Hall AC. Volume-sensitive taurine transport in bovine articular chondrocytes. J Physiol 1995; 484 (Pt 3):755-66.

117. Hall AC & Bush PG. The role of a swelling-activated taurine transport pathway in the regulation of articular chondrocyte volume. Pflugers Arch 2001; 442(5):771-81.

118. Hoffmann EK & Dunham PB. Membrane mechanisms and intracellular signalling in cell volume regulation. Int Rev Cytol 1995; 161:173-262.

119. Margalit A, Sofer Y, Grossman S, Reynaud D, Pace-Asciak CR, & Livne AA. Hepoxilin A3 is the endogenous lipid mediator opposing hypotonic swelling of intact human platelets. Proc Natl Acad Sci U S A 1993; 90(7):2589-92.

120. Sanchez JC, Danks TA, & Wilkins RJ. Mechanisms involved in the increase in intracellular calcium following hypotonic shock in bovine articular chondrocytes. Gen Physiol Biophys 2003; 22(4):487-500.

121. Pritchard S, Votta BJ, Kumar S, & Guilak F. Interleukin-1 inhibits osmotically induced calcium signaling and volume regulation in articular chondrocytes. Osteoarthritis Cartilage 2008; 16(12):1466-73.

122. Phan MN, Leddy HA, Votta BJ, Kumar S, Levy DS, Lipshutz DB, Lee SH, Liedtke W, & Guilak F. Functional characterization of TRPV4 as an osmotically sensitive ion channel in porcine articular chondrocytes. Arthritis Rheum 2009; 60(10):3028-37.

123. Kerrigan MJ & Hall AC. Stimulation of regulatory volume decrease (RVD) by isolated bovine articular chondrocytes following F-actin disruption using latrunculin B. Biorheology 2005; 42(4):283-93.

124. Isoya E, Toyoda F, Imai S, Okumura N, Kumagai K, Omatsu-Kanbe M, Kubo M, Matsuura H, & Matsusue Y. Swelling-activated Cl(-) current in isolated rabbit articular chondrocytes: inhibition by arachidonic Acid. J Pharmacol Sci 2009; 109(2):293-304.

125. Hall AC, Starks I, Shoults CL, & Rashidbigi S. Pathways for K+ transport across the bovine articular chondrocyte membrane and their sensitivity to cell volume. Am J Physiol 1996; 270(5 Pt 1):C1300-10.

126. Banderali U & Roy G. Anion channels for amino acids in MDCK cells. Am J Physiol 1992; 263(6 Pt 1):C1200-7.

127. Kirk K, Ellory JC, & Young JD. Transport of organic substrates via a volume-activated channel. J Biol Chem 1992; 267(33):23475-8.

128. Jackson PS & Strange K. Volume-sensitive anion channels mediate swelling-activated inositol and taurine efflux. Am J Physiol 1993; 265(6 Pt 1):C1489-500.

129. Jackson PS, Morrison R, & Strange K. The volume-sensitive organic osmolyte-anion channel VSOAC is regulated by nonhydrolytic ATP binding. Am J Physiol 1994; 267(5 Pt 1):C1203-9.

130. Kirk J & Kirk K. Inhibition of volume-activated I- and taurine efflux from HeLa cells by P-glycoprotein blockers correlates with calmodulin inhibition. J Biol Chem 1994; 269(47):29389-94.

131. Hoffmann EK & Simonsen LO. Membrane mechanisms in volume and pH regulation in vertebrate cells. Physiol Rev 1989; 69(2):315-82.

132. Wright MO, Stockwell RA, & Nuki G. Response of plasma membrane to applied hydrostatic pressure in chondrocytes and fibroblasts. Connect Tissue Res 1992; 28(1-2):49-70.

133. Grandolfo M, Martina M, Ruzzier F, & Vittur F. A potassium channel in cultured chondrocytes. Calcif Tissue Int 1990; 47(5):302-7.

134. Wilkins RJ & Hall AC. Measurement of intracellular pH in isolated bovine articular chondrocytes. Exp Physiol 1992; 77(3):521-4.

135. Ong SB, Shah D, Qusous A, Jarvis SM, & Kerrigan MJ. Stimulation of regulatory volume increase (RVI) in avian articular chondrocytes by gadolinium chloride. Biochem Cell Biol 2010; 88(3):505-12.

136. Flatman PW. Regulation of Na-K-2Cl cotransport by phosphorylation and protein-protein interactions. Biochim Biophys Acta 2002; 1566(1-2):140-51.

137. Yamazaki N, Browning JA, & Wilkins RJ. Modulation of Na(+) x H(+) exchange by osmotic shock in isolated bovinearticular chondrocytes. Acta Physiol Scand 2000; 169(3):221-8.

138. Lange K. Microvillar Ca++ signaling: a new view of an old problem. J Cell Physiol 1999; 180(1):19-34.

139. Ingber DE, Dike L, Hansen L, Karp S, Liley H, Maniotis A, McNamee H, Mooney D, Plopper G, Sims J, *et al*. Cellular tensegrity: exploring how mechanical changes in the cytoskeleton regulate cell growth, migration, and tissue pattern during morphogenesis. Int Rev Cytol 1994; 150:173-224.

140. Janmey PA. The cytoskeleton and cell signaling: component localization and mechanical coupling. Physiol Rev 1998; 78(3):763-81.

141. Guilak F, Ting-Beall HP, Baer AE, Trickey WR, Erickson GR, & Setton LA. Viscoelastic properties of intervertebral disc cells. Identification of two biomechanically distinct cell populations. Spine (Phila Pa 1976) 1999; 24(23):2475-83.

142. Baer AE & Setton LA. The micromechanical environment of intervertebral disc cells: effect of matrix anisotropy and cell geometry predicted by a linear model. Journal of biomechanical engineering 2000; 122(3):245-51.

143. Langille BL & Adamson SL. Relationship between blood flow direction and endothelial cell orientation at arterial branch sites in rabbits and mice. Circ Res 1981; 48(4):481-8.

144. Nerem RM, Levesque MJ, & Cornhill JF. Vascular endothelial morphology as an indicator of the pattern of blood flow. J Biomech Eng 1981; 103(3):172-6.

145. Dewey CF, Jr., Bussolari SR, Gimbrone MA, Jr., & Davies PF. The dynamic response of vascular endothelial cells to fluid shear stress. J Biomech Eng 1981; 103(3):177-85.

146. Smith RL, Donlon BS, Gupta MK, Mohtai M, Das P, Carter DR, Cooke J, Gibbons G, Hutchinson N, & Schurman DJ. Effects of fluid-induced shear on articular chondrocyte morphology and metabolism in vitro. J Orthop Res 1995; 13(6):824-31.

147. Cao L, Guilak F, & Setton LA. Pericellular Matrix Mechanics in the Anulus Fibrosus Predicted by a Three-Dimensional Finite Element Model and In Situ Morphology. Cell Mol Bioeng 2009; 2(3):306-19.

148. Cao L, Guilak F, & Setton LA. Three-dimensional finite element modeling of pericellular matrix and cell mechanics in the nucleus pulposus of the intervertebral disk based on in situ morphology. Biomech Model Mechanobiol 2011; 10(1):1-10.

149. Guilak F & Mow VC. The mechanical environment of the chondrocyte: a biphasic finite element model of cell-matrix interactions in articular cartilage. Journal of biomechanics 2000; 33(12):1663-73.

150. Kim E, Guilak F, & Haider MA. The dynamic mechanical environment of the chondrocyte: a biphasic finite element model of cell-matrix interactions under cyclic compressive loading. J Biomech Eng 2008; 130(6):061009.

151. Ateshian GA, Costa KD, & Hung CT. A theoretical analysis of water transport through chondrocytes. Biomech Model Mechanobiol 2007; 6(1-2):91-101.

152. Oswald ES, Chao PH, Bulinski JC, Ateshian GA, & Hung CT. Dependence of zonal chondrocyte water transport properties on osmotic environment. Cell Mol Bioeng 2008; 1(4):339-48.

153. Johannessen W & Elliott DM. Effects of degeneration on the biphasic material properties of human nucleus pulposus in confined compression. Spine (Phila Pa 1976) 2005; 30(24):E724-9.

154. Iatridis JC, Setton LA, Weidenbaum M, & Mow VC. Alterations in the mechanical behavior of the human lumbar nucleus pulposus with degeneration and aging. Journal of orthopaedic research : official publication of the Orthopaedic Research Society 1997; 15(2):318-22.

155. Curry MR, Kleinhans FW, & Watson PF. Measurement of the water permeability of the membranes of boar, ram, and rabbit spermatozoa using concentration-dependent self-quenching of an entrapped fluorophore. Cryobiology 2000; 41(2):167-73.

156. Lucio AD, Santos RA, & Mesquita ON. Measurements and modeling of water transport and osmoregulation in a single kidney cell using optical tweezers and videomicroscopy. Phys Rev E Stat Nonlin Soft Matter Phys 2003; 68(4 Pt 1):041906.

157. Ateshian GA, Morrison B, 3rd, & Hung CT. Modeling of active transmembrane transport in a mixture theory framework. Ann Biomed Eng 38(5):1801-14.

158. Eisenberg S & Grodzinsky AJ. Electrokinetic micromodel of extracellular matrix and other polyelectrolyte networks. Physicochem Hydrodynam 1988; 10:517-30.

159. Huyghe JM & Janssen JD. Quadriphasic mechanics of swelling incompressible porous media. International Journal of Engineering Science 1997; 35:793-802.

160. Mow VC, Kuei SC, Lai WM, & Armstrong CG. Biphasic creep and stress relaxation of articular cartilage in compression? Theory and experiments. J Biomech Eng 1980; 102(1):73-84.

161. Biot MA. General theory of three-dimensional consolidation. Journal of Applied Physics 1941; (12):155-64.

162. Bowen RM. Incompressible porous media models by use of the theory of mixtures. Int J Engng Sci 1980; 18:1129-48.

163. Mow VC, Kuei SC, Lai WM, & Armstrong CG. Biphasic creep and stress relaxation of articular cartilage in compression: Theory and experiments. Journal of biomechanical engineering 1980; 102(1):73-84.

164. Katchalsky A & Curran PF (1975) Nonequilibrium Thermodynamics in Biophysics. (Harvard University Press, Cambridge, MA).

165. Gu WY, Lai WM, & Mow VC. Transport of fluid and ions through a porous-permeable charged-hydrated tissue, and streaming potential data on normal bovine articular cartilage. Journal of biomechanics 1993; 26(6):709-23.

166. Gu WY, Lewis B, Lai WM, Ratcliffe A, & Mow VC. A technique for measuring volume and true density of the solid matrix of cartilaginous tissues. Advances in Bioengineering, ASME 1996; BED33:89-90.

167. Gu WY, Hung CT, Lai WM, & Mow VC. Analysis of transient swelling of isolated cells. Annals of Biomedical Engineering 1997; 25/S.1:S-80.

168. Gu WY, Lai WM, & Mow VC. A triphasic analysis of negative osmotic flows through charged hydrated soft tissues. Journal of biomechanics 1997; 30(1):71-78.

169. Gu WY, Lai WM, & Mow VC. Transport of multi-electrolytes in charged hydrated biological soft tissues. Transport in Porous Media 1999; 34:143-57.

170. Gu WY, Sun DN, Lai WM, & Mow VC. Analysis of the dynamic permeation experiment with implication to cartilaginous tissue engineering. Journal of biomechanical engineering 2004; 126(4):485-91.

171. Lai WM, Gu WY, & Mow VC. Flows of electrolytes through charged hydrated biologic tissue. Applied Mechanics Review 1994; 47 (part 2):277-81.

172. Lai WM, Gu WY, & Mow VC. On the conditional equivalence of chemical loading and mechanical loading on articular cartilage. JBiomech 1998; 31(12):1181-85.

173. Lai WM, Mow VC, Sun DD, & Ateshian GA. On the electric potentials inside a charged soft hydrated biological tissue: streaming potential versus diffusion potential. Journal of biomechanical engineering 2000; 122(4):336-46.

174. Lai WM, Sun DD, Ateshian GA, Guo XE, & Mow VC. Electrical signals for chondrocytes in cartilage. Biorheology 2002; 39(1,2):39-45.

175. Mow VC, Ateshian GA, Lai WM, & Gu WY. Effects of fixed charge density on the stress-relaxation behavior of hydrated soft tissues in a confined compression problem. International Journal of Solids and Structures 1998; 35:4945-62.

176. Sun DN, Gu WY, Guo XE, Lai WM, & Mow VC. A mixed finite element formulation of triphasic mechano-electrochemical theory for charged, hydrated biological soft tissues. International Journal for Numerical Methods in Engineering 1999; 45:1375-402.

177. Gu WY, Lai WM, & Mow VC. A mixture theory for charged-hydrated soft tissues containing multi- electrolytes: passive transport and swelling behaviors. Journal of biomechanical engineering 1998; 120(2):169-80.

178. Cowin SC. Bone poroelasticity. Journal of biomechanics 1999; 32(3):217-38.

179. Weinbaum S & Curry FE. Modelling the structural pathways for transcapillary exchange. SympSoc ExpBiol 1995; 49:323-45.

180. Zeng Y, Cowin SC, & Weinbaum S. A fiber matrix model for fluid flow and streaming potentials in the canaliculi of an osteon. AnnBiomedEng 1994; 22(3):280-92.

181. Buschmann MD & Grodzinsky AJ. A molecular model of proteoglycan-associated electrostatic forces in cartilage mechanics. Journal of biomechanical engineering 1995; 117(2):179-92.

182. Chammas P, Federspiel WJ, & Eisenberg SR. A microcontinuum model of electrokinetic coupling in the extracellular matrix: perturbation formulation and solution. Journal of Colloid and Interface Science 1994; 168:526-38.

183. Eisenberg SR & Grodzinsky AJ. Electrokinetic micromodel of extracellular-matrix and other poly-electrolyte networks. Physicochemical Hydrodynamics 1988; 10(4):517-39.

184. Huyghe JM & Janssen JD. Quadriphasic mechanics of swelling incompressible porous media. Int J Engng Sci 1997; 35(8):793-802.

185. Huyghe JM & Janssen JD. Thermo-chemo-electro-mechanical formulation of saturated charged porous solids. Transport in Porous Media 1999; 34:129-41.

186. Garcia AM, Frank EH, Grimshaw PE, & Grodzinsky AJ. Contributions of fluid convection and electrical migration to transport in cartilage: relevance to loading. ArchBiochemBiophys 1996; 333(2):317-25.

187. Meares P. The physical chemistry of transport and separation by membranes. Membrane separation processes. ed Meares P. Amsterdam: Elsevier; 1976; pp 1-38.

188. Deen WM. Hindered transport of large molecules in liquid-filled pores. AIChE Journal 1987; 33(9):1409-25.

189. Tikhomolova KP (1993) Electro-osmosis. (Ellis Horwood, London).

190. Buckwalter JA. Aging and degeneration of the human intervertebral disc. Spine (Phila Pa 1976) 1995; 20(11):1307-14.

191. Battie MC & Videman T. Lumbar disc degeneration: epidemiology and genetics. J Bone Joint Surg Am 2006; 88 Suppl 2:3-9.

192. Urban JP & Winlove CP. Pathophysiology of the intervertebral disc and the challenges for MRI. J Magn Reson Imaging 2007; 25(2):419-32.

193. Shirazi-Adl A, Taheri M, & Urban JP. Analysis of cell viability in intervertebral disc: Effect of endplate permeability on cell population. J Biomech 2010; 43(7):1330-6.

194. Ishihara H & Urban JP. Effects of low oxygen concentrations and metabolic inhibitors on proteoglycan and protein synthesis rates in the intervertebral disc. J Orthop Res 1999; 17(6):829-35.

195. Horner HA, Roberts S, Bielby RC, Menage J, Evans H, & Urban JP. Cells from different regions of the intervertebral disc: effect of culture system on matrix expression and cell phenotype. Spine 2002; 27(10):1018-28.

196. Urban JP, Smith S, & Fairbank JC. Nutrition of the intervertebral disc. Spine 2004; 29(23):2700-9.

197. Lundon K & Bolton K. Structure and function of the lumbar intervertebral disk in health, aging, and pathologic conditions. J Orthop Sports Phys Ther 2001; 31(6):291-303; discussion 04-6.

198. Ayotte DC, Ito K, & Tepic S. Direction-dependent resistance to flow in the endplate of the intervertebral disc: an ex vivo study. J Orthop Res 2001; 19(6):1073-7.

199. Ayotte DC, Ito K, Perren SM, & Tepic S. Direction-dependent constriction flow in a poroelastic solid: the intervertebral disc valve. Journal of biomechanical engineering 2000; 122(6):587-93.

200. Accadbled F, Laffosse JM, Ambard D, Gomez-Brouchet A, de Gauzy JS, & Swider P. Influence of location, fluid flow direction, and tissue maturity on the macroscopic permeability of vertebral end plates. Spine 2008; 33(6):612-9.

201. Roberts S, Menage J, & Eisenstein SM. The cartilage end-plate and intervertebral disc in scoliosis: calcification and other sequelae. J Orthop Res 1993; 11(5):747-57.

202. Urban MR, Fairbank JC, Etherington PJ, Loh FL, Winlove CP, & Urban JP. Electrochemical measurement of transport into scoliotic intervertebral discs in vivo using nitrous oxide as a tracer. Spine 2001; 26(8):984-90.

203. Soukane DM, Shirazi-Adl A, & Urban JP. Analysis of nonlinear coupled diffusion of oxygen and lactic acid in intervertebral discs. J Biomech Eng 2005; 127(7):1121-6.

204. Soukane DM, Shirazi-Adl A, & Urban JP. Computation of coupled diffusion of oxygen, glucose and lactic acid in an intervertebral disc. J Biomech 2007; 40(12):2645-54.

205. Jackson AR, Huang CY, Brown MD, & Gu WY. 3D finite element analysis of nutrient distributions and cell viability in the intervertebral disc: effects of deformation and degeneration. J Biomech Eng 2011; 133(9):091006.

206. Zhu Q, Jackson AR, & Gu WY. Cell viability in intervertebral disc under various nutritional and dynamic loading conditions: 3d Finite element analysis. J Biomech 2012;

207. Holm S, Maroudas A, Urban JP, Selstam G, & Nachemson A. Nutrition of the intervertebral disc: solute transport and metabolism. Connect Tissue Res 1981; 8(2):101-19.

208. Iatridis JC, Laible JP, & Krag MH. Influence of fixed charge density magnitude and distribution on the intervertebral disc: applications of a poroelastic and chemical electric (PEACE) model. J Biomech Eng 2003; 125(1):12-24.

209. Accadbled F, Laffosse JM, Ambard D, Gomez-Brouchet A, de Gauzy JS, & Swider P. Influence of location, fluid flow direction, and tissue maturity on the macroscopic permeability of vertebral end plates. Spine (Phila Pa 1976) 2008; 33(6):612-9.

210. Sun DN, Gu WY, Guo XE, Lai WM, & Mow VC. A mixed finite element formulation of triphasic mechano-electrochemical theory for charged, hydrated biological soft tissues. Int J Numer Meth Engng 1999; 45:1375-402.

211. Bartels EM, Fairbank JC, Winlove CP, & Urban JP. Oxygen and lactate concentrations measured in vivo in the intervertebral discs of patients with scoliosis and back pain. Spine (Phila Pa 1976) 1998; 23(1):1-7; discussion 8.

212. Jackson AR, Huang CY, & Gu WY. Effect of endplate calcification and mechanical deformation on the distribution of glucose in intervertebral disc: a 3D finite element study. Comput Methods Biomech Biomed Engin 2011; 14(2):195-204.

213. Mokhbi Soukane D, Shirazi-Adl A, & Urban JP. Investigation of solute concentrations in a 3D model of intervertebral disc. Eur Spine J 2009; 18(2):254-62.

214. Urban JP, Holm S, Maroudas A, & Nachemson A. Nutrition of the intervertebral disc: effect of fluid flow on solute transport. Clin Orthop Relat Res 1982; (170):296-302.

215. O'Hara BP, Urban JP, & Maroudas A. Influence of cyclic loading on the nutrition of articular cartilage. Ann Rheum Dis 1990; 49(7):536-39.

216. McMillan DW, Garbutt G, & Adams MA. Effect of sustained loading on the water content of intervertebral discs: implications for disc metabolism. Ann Rheum Dis 1996; 55(12):880-7.

217. Yao H & Gu WY. Convection and diffusion in charged hydrated soft tissues: a mixture theory approach. Biomech Model Mechanobiol 2007; 6(1-2):63-72.

218. Kandel R, Roberts S, & Urban JP. Tissue engineering and the intervertebral disc: the challenges. Eur Spine J 2008; 17 Suppl 4:480-91.

219. Travascio F & Gu WY. Anisotropic diffusive transport in annulus fibrosus: experimental determination of the diffusion tensor by FRAP technique. Ann Biomed Eng 2007; 35(10):1739-48.

220. Jackson AR, Yuan TY, Huang CY, Travascio F, & Yong Gu W. Effect of compression and anisotropy on the diffusion of glucose in annulus fibrosus. Spine (Phila Pa 1976) 2008; 33(1):1-7.

221. Eyre DR, Benya P, & Buckwalter J. Intervertebral disk: Basic science perspectives. New Perspectives on Low Back Pain. eds Frymoyer JW & Gordon SL. Park Ridge, IL: American Academy of Orthopaedic Surgeons; 1989.

222. Ogata K & Whiteside LA. 1980 Volvo award winner in basic science. Nutritional pathways of the intervertebral disc. An experimental study using hydrogen washout technique. Spine (Phila Pa 1976) 1981; 6(3):211-6.

223. Setton LA, Zhu W, Weidenbaum M, Ratcliffe A, & Mow VC. Compressive properties of the cartilaginous end-plate of the baboon lumbar spine. Journal of Orthopaedic Research 1993; 11(2):228-39.

224. Demers CN, Antoniou J, & Mwale F. Value and limitations of using the bovine tail as a model for the human lumbar spine. Spine (Phila Pa 1976) 2004; 29(24):2793-9.

225. Oshima H, Ishihara H, Urban JP, & Tsuji H. The use of coccygeal discs to study intervertebral disc metabolism. Journal of orthopaedic research : official publication of the Orthopaedic Research Society 1993; 11(3):332-38.

226. Soltz MA & Ateshian GA. Interstitial fluid pressurization during confined compression cyclical loading of articular cartilage. Ann Biomed Eng 2000; 28(2):150-9.

227. Yao H, Justiz MA, Flagler D, & Gu WY. Effects of swelling pressure and hydraulic permeability on dynamic compressive behavior of lumbar annulus fibrosus. Ann Biomed Eng 2002; 30(10):1234-41.

228. Kuo J, Zhang L, Bacro T, & Yao H. The region-dependent biphasic viscoelastic properties of human temporomandibular joint discs under confined compression. J Biomech 2010; 43(7):1316-21.

229. Gu WY, Yao H, Huang CY, & Cheung HS. New insight into deformation-dependent hydraulic permeability of gels and cartilage, and dynamic behavior of agarose gels in confined compression. J Biomech 2003; 36(4):593-8.

230. Thompson JP, Pearce RH, Schechter MT, Adams ME, Tsang IK, & Bishop PB. Preliminary evaluation of a scheme for grading the gross morphology of the human intervertebral disc. Spine (Phila Pa 1976) 1990; 15(5):411-5.

231. Perie DS, Maclean JJ, Owen JP, & Iatridis JC. Correlating material properties with tissue composition in enzymatically digested bovine annulus fibrosus and nucleus pulposus tissue. Ann Biomed Eng 2006; 34(5):769-77.

232. Best BA, Guilak F, Setton LA, Zhu W, Saed-Nejad F, Ratcliffe A, Weidenbaum M, & Mow VC. Compressive mechanical properties of the human anulus fibrosus and their relationship to biochemical composition. Spine (Phila Pa 1976) 1994; 19(2):212-21.

233. Drost MR, Willems P, Snijders H, Huyghe JM, Janssen JD, & Huson A. Confined compression of canine annulus fibrosus under chemical and mechanical loading. J Biomech Eng 1995; 117(4):390-6.

234. Iatridis JC, Setton LA, Foster RJ, Rawlins BA, Weidenbaum M, & Mow VC. Degeneration affects the anisotropic and nonlinear behaviors of human anulus fibrosus in compression. Journal of biomechanics 1998; 31(6):535-44.

235. Perie D, Korda D, & Iatridis JC. Confined compression experiments on bovine nucleus pulposus and annulus fibrosus: sensitivity of the experiment in the determination of compressive modulus and hydraulic permeability. J Biomech 2005; 38(11):2164-71.

236. Mansour JM & Mow VC. The permeability of articular cartilage under compressive strain and at high pressures. J Bone Joint Surg Am 1976; 58(4):509-16.

237. Maroudas A. Biophysical chemistry of cartilaginous tissues with special reference to solute and fluid transport. Biorheology 1975; 12(3-4):233-48.

238. Gu WY & Yao H. Effects of hydration and fixed charge density on fluid transport in charged hydrated soft tissues. Ann Biomed Eng 2003; 31(10):1162-70.

239. Lee RB & Urban JP. Evidence for a negative Pasteur effect in articular cartilage. BiochemJ 1997; 321 (Pt 1):95-102.

240. Zhou S, Cui Z, & Urban JP. Factors influencing the oxygen concentration gradient from the synovial surface of articular cartilage to the cartilage-bone interface: a modeling study. Arthritis Rheum 2004; 50(12):3915-24.

241. Heywood HK, Knight MM, & Lee DA. Both superficial and deep zone articular chondrocyte subpopulations exhibit the Crabtree effect but have different basal oxygen consumption rates. JCell Physiol 2010; 223(3):630-39.

242. Bibby SR, Jones DA, Ripley RM, & Urban JP. Metabolism of the intervertebral disc: effects of low levels of oxygen, glucose, and pH on rates of energy metabolism of bovine nucleus pulposus cells. Spine (Phila Pa 1976) 2005; 30(5):487-96.

243. Huang CY, Yuan TY, Jackson AR, Hazbun L, Fraker C, & Gu WY. Effects of low glucose concentrations on oxygen consumption rates of intervertebral disc cells. Spine (Phila Pa 1976) 2007; 32(19):2063-69.

244. Guehring T, Wilde G, Sumner M, Grunhagen T, Karney GB, Tirlapur UK, & Urban JP. Notochordal intervertebral disc cells: sensitivity to nutrient deprivation. Arthritis Rheum 2009; 60(4):1026-34.

245. Stockwell RA (1979) Biology of Cartilage Cells. (Cambridge University Press, Cambridge, UK).

246. Otte P. Basic cell metabolism of articular cartilage. Manometric studies. ZRheumatol 1991; 50(5):304-12.

247. Holm S, Maroudas A, Urban JP, Selstam G, & Nachemson A. Nutrition of the intervertebral disc: solute transport and metabolism. ConnectTissue Res 1981; 8(2):101-19.

248. Heywood HK & Lee DA. Monolayer expansion induces an oxidative metabolism and ROS in chondrocytes. BiochemBiophysResCommun 2008; 373(2):224-29.

249. Heywood HK & Lee DA. Low oxygen reduces the modulation to an oxidative phenotype in monolayer-expanded chondrocytes. JCell Physiol 2010; 222(1):248-53.

250. Rees LA. The structure and function of the mandibular joint. BrDentJ 1954; 96:125-33.

251. Leonardi R, Lo ML, Bernasconi G, Caltabiano C, Piacentini C, & Caltabiano M. Expression of vascular endothelial growth factor in human dysfunctional temporomandibular joint discs. ArchOral Biol 2003; 48(3):185-92.

252. Detamore MS & Athanasiou KA. Motivation, characterization, and strategy for tissue engineering the temporomandibular joint disc. Tissue Eng 2003; 9(6):1065-87.

253. Detamore MS, Hegde JN, Wagle RR, Almarza AJ, Montufar-Solis D, Duke PJ, & Athanasiou KA. Cell type and distribution in the porcine temporomandibular joint disc. JOral MaxillofacSurg 2006; 64(2):243-48.

254. Mah J. Histochemistry of the foetal human temporomandibular joint articular disc. EurJOrthod 2004; 26(4):359-65.

255. Yoshida H, Fujita S, Nishida M, & Iizuka T. Localization of lymph capillaries and blood capillaries in human temporomandibular joint discs. J Oral Rehabil 1999; 26(7):600-7.

256. Weiss TF (1996) Cellullar Biophysics. (MIT Press, Cambridge, MA).

257. de Donder T (1936) Thermodynamic Theory of Affinity. (Stanford University Press, CA).

258. Tsuga K, Tohse N, Yoshino M, Sugimoto T, Yamashita T, Ishii S, & Yabu H. Chloride conductance determining membrane potential of rabbit articular chondrocytes. J Membr Biol 2002; 185(1):75-81.

259. Sugimoto T, Yoshino M, Nagao M, Ishii S, & Yabu H. Voltage-gated ionic channels in cultured rabbit articular chondrocytes. Comparative biochemistry and physiology Part C, Pharmacology, toxicology & endocrinology 1996; 115(3):223-32.

260. Wilson JR, Duncan NA, Giles WR, & Clark RB. A voltage-dependent K+ current contributes to membrane potential of acutely isolated canine articular chondrocytes. J Physiol 2004; 557(Pt 1):93-104.

261. Clark RB, Hatano N, Kondo C, Belke DD, Brown BS, Kumar S, Votta BJ, & Giles WR. Voltage-gated K+ currents in mouse articular chondrocytes regulate membrane potential. Channels (Austin) 2010; 4(3):179-91.

262. Funabashi K, Fujii M, Yamamura H, Ohya S, & Imaizumi Y. Contribution of chloride channel conductance to the regulation of resting membrane potential in chondrocytes. J Pharmacol Sci 2010; 113(1):94-9.

263. Mobasheri A, Lewis R, Maxwell JE, Hill C, Womack M, & Barrett-Jolley R. Characterization of a stretch-activated potassium channel in chondrocytes. J Cell Physiol 223(2):511-8.

264. Kelsey JL, Mundt DF, & Golden AL. Epidemiology of low back pain. The Lumbar Spine and Back Pain. ed Malcolm JIV. New York: Churchill Livingstone; 1992.